

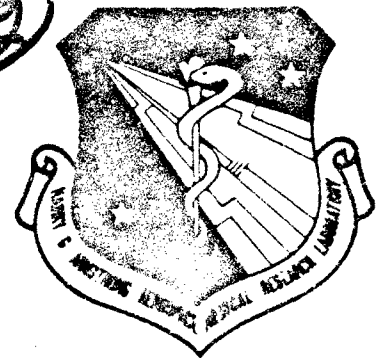
DTIC FILE COPY

AAMRL-TR-90-017  
NMRI-90-15

AD-A223 158



2



# A STUDY OF MIXED CONVECTION IN LARGE BAFFLED RECTANGULAR CHAMBERS WITH AND WITHOUT INTERNAL HEAT SOURCES

K. L. Yerkes

NSI TECHNOLOGY SERVICES CORPORATION  
101 WOODMAN DRIVE, SUITE 12  
DAYTON, OHIO 45431

MARCH 1990

20030206123

FINAL REPORT FOR THE PERIOD JULY 1989 THROUGH FEBRUARY 1990

Approved for public release; distribution is unlimited.

HARRY G. ARMSTRONG AEROSPACE MEDICAL RESEARCH LABORATORY  
HUMAN SYSTEMS DIVISION  
AIR FORCE SYSTEMS COMMAND  
WRIGHT-PATTERSON AIR FORCE BASE, OHIO 45433-6573

90 06 21 032

## NOTICES

When U S Government drawings, specifications, or other data are used for any purpose other than a definitely related Government procurement operation, the Government thereby incurs no responsibility nor any obligation whatsoever, and the fact that the Government may have formulated, furnished, or in any way supplied the said drawings, specifications, or other data, is not to be regarded by implication or otherwise, as in any manner licensing the holder or any other person or corporation, or conveying any rights or permission to manufacture, use, or sell any patented invention that may in any way be related thereto.

Please do not request copies of this report from the Harry G. Armstrong Aerospace Medical Research Laboratory. Additional copies may be purchased from:

National Technical Information Service  
5285 Port Royal Road  
Springfield, Virginia 22161

Federal Government agencies and their contractors registered with Defense Technical Information Center should direct requests for copies of this report to:

Defense Technical Information Center  
Cameron Station  
Alexandria, Virginia 22314

## TECHNICAL REVIEW AND APPROVAL

AAMRL-TR-90-017

The experiments reported herein were conducted according to the "Guide for the Care and Use of Laboratory Animals," Institute of Laboratory Animal Resources, National Research Council.

This report has been reviewed by the Office of Public Affairs (PA) and is releasable to the National Technical Information Service (NTIS). At NTIS, it will be available to the general public, including foreign nations.

This technical report has been reviewed and is approved for publication.

FOR THE COMMANDER



MICHAEL B. BALLINGER, Lt Col, USAF, BSC  
Chief, Toxic Hazards Division  
Harry G. Armstrong Aerospace Medical Research Laboratory

SECURITY CLASSIFICATION OF THIS PAGE

UNCLASSIFIED

## REPORT DOCUMENTATION PAGE

Form Approved  
OMB No. 0704-0188

|   |  |  |  |  |
|---|--|--|--|--|
| 1a. REPORT SECURITY CLASSIFICATION<br>UNCLASSIFIED  |  |  | 1b. RESTRICTIVE MARKINGS   |  |
| 2a. SECURITY CLASSIFICATION AUTHORITY   |  |  | 3. DISTRIBUTION AVAILABILITY OF REPORT   |  |
| 2b. DECLASSIFICATION/DOWNGRADING SCHEDULE   |  |  | Approved for public release, distribution is unlimited.  |  |
| 4. PERFORMING ORGANIZATION REPORT NUMBER(S)   |  |  | 5. MONITORING ORGANIZATION REPORT NUMBER(S)<br>AAMRL-TR-90-017<br>NMRI-90-15   |  |
| 6a. NAME OF PERFORMING ORGANIZATION<br>NSI Technology Services Corporation  | 6b. OFFICE SYMBOL<br>(if applicable)   | 7a. NAME OF MONITORING ORGANIZATION<br>AAMRL, Toxic Hazards Division                     |  |  |
| 6c. ADDRESS (City, State, and ZIP Code)<br>101 Woodman Dr., Suite 12<br>Dayton, Ohio 45431  |  | 7b. ADDRESS (City, State, and ZIP Code)<br>HSD, AFSC<br>Wright-Patterson AFB, Ohio 45433 |  |  |
| 8a. NAME OF FUNDING SPONSORING ORGANIZATION   | 8b. OFFICE SYMBOL<br>(if applicable)   | 9. PROCUREMENT INSTRUMENT IDENTIFICATION NUMBER<br>F33615-85-C-0532                      |  |  |
| 8c. ADDRESS (City, State, and ZIP Code)   |  | 10. SOURCE OF FUNDING NUMBERS  |  |  |
|   |  | PROGRAM ELEMENT NO<br>62202F   | PROJECT NO<br>6302   | TASK NO<br>00<br>WORK UNIT<br>ACCESSION NO<br>01 |
| 11. TITLE (Include Security Classification)<br>A Study of Mixed Convection in Large Baffled Rectangular Chambers With or Without Internal Heat Sources  |  |  |  |  |
| 12. PERSONAL AUTHOR(S)<br>K. L. Yerkes  |  |  |  |  |
| 13a. TYPE OF REPORT<br>Final  | 13b. TIME COVERED<br>FROM 1985 TO 1990 | 14. DATE OF REPORT (Year, Month, Day)<br>March 1990                                      | 15. PAGE COUNT<br>188  |  |
| 16. SUPPLEMENTARY NOTATION  |  |  |  |  |
| 17. COSAT CODES   |  |  | 18. SUBJECT TERMS (Continued on reverse if necessary and identify by block number)   |  |
| FIELD   | GROUP                                  | SUB GROUP  | Mixed Convection, Thermal Effects, Inhalation Toxicology, Flow, Exposure Chambers, Internal Heat Sources, Theoretical, Buoyant, Experimental |  |
|   |  |  |  |  |
| 19. ABSTRACT (Continue on reverse if necessary and identify by block number.)<br>A numerical and experimental investigation to determine the thermal effects on the development of the flow structure in large baffled rectangular chambers with and without internal heat sources has been completed. Two- and three-dimensional numerical models were formulated using the time-dependent laminar Navier-Stokes equations assuming a Boussinesq fluid with a Prandtl number of 0.7. Experiments were conducted using a scaled-down model simulated the full-size chamber enabling experimental data to be obtained and subsequently compared with numerical results. Flow visualization experiments were conducted using the larger, full-size chamber. Internal horizontal baffles and heat sources were located symmetrically about the vertical centerline axis. Mixed convection without internal heat sources for both "aided" and "opposed" buoyant forces showed that the development of the flow structure was sensitive to small variations in the temperature difference between the inlet and the vertical walls. Mixed convection with internal heat sources showed the flow structure to develop through a series of bifurcations from steady state, to periodic, aperiodic and finally chaotic with increasing heat source temperature. Use of the scaled-down laboratory experimental model as an indicator for the flow development in the larger full-size chamber showed significant three-dimensional effects. Flow visualization in the larger full-size chamber using dihydrocarbon aerosol droplets showed good agreement with the two-dimensional numerical results. |  |  |  |  |
| 20. DISTRIBUTION AVAILABILITY OF ABSTRACT<br><input checked="" type="checkbox"/> UNCLASSIFIED/UNLIMITED <input type="checkbox"/> SAME AS RPT <input type="checkbox"/> DTIC USERS  |  |  | 21. ABSTRACT SECURITY CLASSIFICATION<br>UNCLASSIFIED   |  |
| 22. NAME OF RESPONSIBLE INDIVIDUAL<br>Michael B. Ballinger, 11 Col USAF BSC   |  |  | 22b. TELEPHONE (include Area Code)<br>(513) 255-3916   | 22c. OFFICE SYMBOL<br>AAMRL/TH                   |

DD FORM 1473, JUN 86

Previous editions are obsolete

SECURITY CLASSIFICATION OF THIS PAGE

UNCLASSIFIED

## PREFACE

This is one of a series of reports describing results of experimental laboratory programs conducted at the Toxic Hazards Research Unit, NSI Technology Services. This document serves as a final report on thermal effects on inhalation chamber toxicant distribution. The research described in this report began on 7 July 1989 and was completed on 23 February 1990 under U.S. Air Force Contract No. F33615-85-C-0532 and meets the research requirements of Technical Directive study USN 0-80 8 entitled "Thermal Effects on Inhalation Chamber Toxicant Distribution".

Lt Col Michael B. Ballinger served as Contract Technical Monitor for the U.S. Air Force, Harry G. Armstrong Aerospace Medical Research Laboratory. This study was sponsored by the U.S. Navy under the direction of CDR David A. Macys, MSC, USN. This work was supported by the Naval Medical Research and Development Command Task M0096 004 0006.

The opinions contained herein are those of the authors and are not to be construed as official or reflecting the views of the Department of the Navy or the Naval Services at large. Quality assurance was provided by an outside panel of expert reviewers.

|                    |                                     |
|--------------------|-------------------------------------|
| Accession For      |                                     |
| NTIS GRA&I         | <input checked="" type="checkbox"/> |
| DTIC TAB           | <input type="checkbox"/>            |
| Unannounced        | <input type="checkbox"/>            |
| Justification      |                                     |
| By _____           |                                     |
| Distribution/      |                                     |
| Availability Codes |                                     |
| Dist _____         |                                     |
| Special _____      |                                     |
| A-1                |                                     |



A STUDY OF MIXED CONVECTION IN LARGE BAFFLED RECTANGULAR  
CHAMBERS WITH AND WITHOUT INTERNAL HEAT SOURCES

A thesis submitted in partial fulfillment  
of the requirements for the degree of  
Master of Science

By

KIRK LEE YERKES  
B.S., West Virginia University, 1986

1989  
Wright State University

WRIGHT STATE UNIVERSITY  
SCHOOL OF GRADUATE STUDIES

December, 1989

I HEREBY RECOMMEND THAT THE THESIS PREPARED  
UNDER MY SUPERVISION BY Kirk Lee Yerkes ENTITLED  
A Study of Mixed Convection in Large Baffled Rectangular

Chambers with and without Internal Heat Sources

IS ACCEPTED IN PARTIAL FULFILLMENT OF THE REQUIREMENTS FOR  
THE DEGREE OF Master of Science.

Amir Fagher, Ph.D.  
Thesis Director

J. F. Thomas  
Chairman of Department

Committee on  
Final Examination

Amir Fagher, Ph.D.

Billy W. Turner

David E. B. Reynolds

W. J. ...

David C. ...

Dean of the School of Graduate  
Studies

Robert L. Carpenter

## ABSTRACT

Yerkes, Kirk Lee, M.S., Department of Mechanical and Materials Engineering, Wright State University, 1989. A Study of Mixed Convection in Large Baffled Rectangular Chambers with and without Internal Heat Sources.

A numerical and experimental investigation to determine the thermal effects on the development of the flow structure in large baffled rectangular chambers with and without internal heat sources has been completed. Two- and three-dimensional numerical models were formulated using the time-dependent laminar Navier-Stokes equations assuming a Boussinesq fluid with a Prandtl number of 0.7. Experiments were conducted using a scaled-down laboratory model and the larger, full size chamber. The scaled-down model simulated the full-size chamber enabling experimental data to be obtained and subsequently compared with numerical results. Flow visualization experiments were conducted using the larger, full size chamber. Internal horizontal baffles and heat sources were located symmetrically about the vertical centerline axis. Mixed convection without internal heat sources for both "aided" and "opposed" buoyant forces showed that the development of the flow structure was sensitive to small variations in the temperature difference between the inlet and the vertical walls. Mixed convection

with internal heat sources showed the flow structure to develop through a series of bifurcations from steady state, to periodic, aperiodic and finally chaotic with increasing heat source temperature. Use of the scaled down laboratory experimental model as an indicator for the flow development in the larger full-size chamber showed significant three-dimensional effects. Flow visualization in the larger full-size chamber using Silahydrocarbon aerosol droplets showed good agreement with the two-dimensional numerical results.



## TABLE OF CONTENTS

|   |      |
|---|------|
| ABSTRACT . . . . .  | iii  |
| ACKNOWLEDGEMENT . . . . .   | xvii |
| LIST OF SYMBOLS . . . . .   | xii  |
| LIST OF FIGURES . . . . .   | vii  |
| LIST OF TABLES . . . . .  | xi   |
| STUDY INTRODUCTION . . . . .  | 1    |
| 1. EXPERIMENTAL AND NUMERICAL SIMULATION OF MIXED<br>CONVECTION IN LARGE BAFFLED RECTANGULAR CHAMBERS . . . . . | 2    |
| 1.1. Summary . . . . .  | 2    |
| 1.2. Introduction . . . . .   | 3    |
| 1.3. Analysis . . . . .   | 7    |
| 1.4. Numerical Scheme . . . . .   | 12   |
| 1.5. Experimental Approach . . . . .  | 15   |
| 1.6. Results and Discussion . . . . .   | 17   |
| 1.7. Conclusions . . . . .  | 23   |
| 2. MIXED CONVECTION ANALYSIS IN LARGE BAFFLED RECT-<br>ANGULAR CHAMBERS WITH INTERNAL HEAT SOURCES . . . . .    | 40   |
| 2.1. Summary . . . . .  | 40   |
| 2.2. Introduction . . . . .   | 41   |
| 2.3. Analysis . . . . .   | 45   |
| 2.4. Numerical Scheme . . . . .   | 48   |
| 2.5. Experimental Approach . . . . .  | 52   |

|  |     |
|--|-----|
| 2.6. Results and Discussion . . . . .  | 54  |
| 2.7. Conclusions . . . . .   | 60  |
| 3. FLOW VISUALIZATION OF MIXED CONVECTION IN LARGE<br>DAFFLED RECTANGULAR CHAMBERS WITH AND WITHOUT INTER-<br>NAL HEAT SOURCES . . . . . | 74  |
| 3.1. Summary . . . . .   | 74  |
| 3.2. Introduction . . . . .  | 75  |
| 3.3. Analysis . . . . .  | 78  |
| 3.4. Numerical Scheme . . . . .  | 84  |
| 3.5. Experimental Approach . . . . .   | 87  |
| 3.6. Results and Discussion . . . . .  | 88  |
| 3.7. Conclusion . . . . .  | 91  |
| OVERALL SUMMARY . . . . .  | 100 |
| . Conclusions . . . . .  | 100 |
| . Recommendations . . . . .  | 102 |
| Appendix A BUOYANT FLOW AND EXPOSURE CHAMBER OVERVIEW<br>103   |     |
| Appendix B EXPERIMENTAL INSTRUMENTATION . . . . .  | 115 |
| Appendix C NUMERICAL FORMULATION (PHOENICS) . . . . .  | 137 |
| Appendix D DISCUSSIONS ON THE USE OF PHOENICS . . . . .  | 156 |
| REFLENCES . . . . .  | 157 |

## LIST OF FIGURES

|  |    |
|--|----|
| 1.1 Chamber geometry specifications (a) two-dimensional geometry<br>(b) three-dimensional laboratory model geometry  | 7  |
| 1.2 Experimental apparatus (a) laboratory experimental model (b)<br>temperature measurement setup  | 15 |
| 1.3 Two-dimensional results (a) velocity direction and magnitude<br>profile case #1 (b) velocity magnitude profile case #2   | 19 |
| 1.4 Two-dimensional results for case #2 (a) chamber velocity direc-<br>tion profile (b) temperature contour  | 19 |
| 1.5 Two-dimensional results for case #3 (a) chamber velocity direc-<br>tion and magnitude profile (b) temperature contour  | 20 |
| 1.6 Two-dimensional results for case #4 (a) chamber velocity direc-<br>tion and magnitude profile (b) temperature contour  | 20 |
| 1.7 Three-dimensional results for case #5 at center plane (a) cham-<br>ber velocity direction and magnitude profile (b) temperature contour                        | 20 |
| 1.8 Three dimensional results for case #6 at center plane (a) cham-<br>ber velocity direction and magnitude profile (b) temperature contour                        | 21 |
| 1.9 Three dimensional results, temperature contour (a) case #5, 0.2°C<br>intervals, 25.3°C to 27.3°C (b) case #6, 0.1°C intervals, 26.3°C to 27.3°C                | 21 |
| 1.10 Velocity vector plot across depth of three-dimensional numerical<br>formulation at lateral distance .25L as viewed from the origin (a) case #5 (b)<br>case #6 | 21 |

|  |    |
|--|----|
| 1.11 Non-dimensional temperature vs. vertical height for two- and three-dimensions and experimental data along Y'-axis at central plane  | 22 |
| 1.12 Non-dimensional temperature vs. vertical height for two and three dimensions and experimental data along Y'-axis at central plane   | 22 |
| 2.1 Chamber geometry specifications (a) two-dimensional geometry (b) three-dimensional laboratory model geometry   | 45 |
| 2.2 Experimental apparatus (a) laboratory experimental model (b) temperature measurement setup   | 52 |
| 2.3 Two-dimensional numerical results at time $t=t_0$ (a) chamber velocity direction and magnitude profile (b) temperature contour   | 55 |
| 2.4 Two-dimensional numerical results at time $t=t_0+30s$ (a) chamber velocity direction and magnitude profile (b) temperature contour   | 55 |
| 2.5 Two-dimensional numerical time-dependent plots of velocity and temperature (a) (.50L, .31H) (b) (.70L, .31H) (c) (.90L, .11H) (d) (.50L, .82H) (e) (.70L, .62H) (f) (.90L, .72H) | 55 |
| 2.6 Two-dimensional numerical phase-space plots of velocity and temperature (a) (.50L, .31H) (b) (.70L, .31H) (c) (.90L, .11H) (d) (.50L, .82H) (e) (.70L, .62H) (f) (.90L, .72H)    | 55 |
| 2.7 Time dependent experimental results for velocity at chamber location (.70L, .31H) with increasing heat source temperature  | 55 |
| 2.8 Comparison of the (a) time-dependent experimental results for velocity and temperature (b) time-dependent numerical results for velocity at                                      |    |

chamber locations: (a) (.50L, .31H) (b) (.70L, .31H) (c) (.90L, .11H) (d) (.50L, .82H) (e) (.70L, .62H) (f) (.90L, .72H) 55

2.9 Experimental results for locating the high velocity boundary layer region at  $0.67H$  59

3.1 Whole-body inhalation exposure chamber 77

3.2 Chamber geometry specification for two-dimensional numerical formulation (a) case #1 (b) case #2 78

3.3 Forces on aerosol droplet 82

3.4 Silahydrocarbon droplet aerosol generation system 87

3.5 Case #1 two-dimensional numerical results showing velocity direction and magnitude and chamber locations for comparison of flow visualization experimental results 89

3.6 Case #2 two-dimensional numerical results showing velocity direction and magnitude and chamber locations for comparison of flow visualization experimental results 89

A.1 Free, forced, and mixed convection regimes for flow in vertical circular tubes for uniform heat flux (UHF) and uniform wall temperature (UWT) boundary conditions 103

A.2 Possible chamber configurations in use for inhalation research (a) horizontal flow chamber (b) multi-tiered chamber (c) pyramidal end cone "Hinnert-type" chamber (d) cylindrical chamber 110

B.1 Free body diagram of rotameter float 116

|   |     |
|---|-----|
| B.2 Rotameter application schematic (a) operational pressure drop,<br>$\delta P = 0$ (b) operational pressure drop, $\delta P \neq 0$ | 117 |
| B.3 Rotameter inlet air calibration curve corrected for $\delta P = 0$  | 123 |
| B.4 Thermocouple calibration curve over the anticipated range of<br>operation with a 99 percent confidence band for the linear fit    | 125 |
| B.5 Thermocouple first order instrument Bode plot   | 125 |
| B.6 Hot wire anemometer calibration cell  | 127 |
| B.7 Hot wire anemometer calibration curves for aligned (flow up)<br>and opposed (flow down) calibration velocities                    | 127 |

---

## LIST OF TABLES

|   |     |
|---|-----|
| 1.1 Parametric Specifications for Numerical and Experimental Investigation          | 26  |
| 1.2 Boundary Layer Thickness and Maximum Velocity                                   | 27  |
| 3.1 Experimental Conditions for 2-Dimensional Numerical Comparison                  | 92  |
| 3.2 Experimental Flow Visualization and 2-Dimensional Numerical Comparison          | 93  |
| B.1 Thermocouple Frequency Response Amplitude Ratio and Phase Shift ( $\tau=1.7s$ ) | 129 |

## LIST OF SYMBOLS

|             |  |
|-------------|--|
| $a$         | constant describing the tube taper of a rotameter            |
| $A$         | cross-sectional area, $m^2$                                  |
| $AR$        | amplitude ratio  |
| $AR_{db}$   | amplitude ratio in decibels                                  |
| $A_1$       | aspect ratio, $L/H$  |
| $A_2$       | aspect ratio, $L/D$  |
| $A_3$       | aspect ratio, $D_h/H$  |
| $\vec{B}$   | body force vector  |
| $\vec{B}_z$ | body force vector z-direction                                |
| $C_c$       | Cunningham slip correction factor                            |
| $C_D$       | drag coefficient   |
| $C_p$       | specific heat, $J/kg \cdot ^\circ C$                         |
| $d$         | rotameter ball diameter or droplet mass median diameter, $m$ |
| $D$         | depth of chamber, $m$  |
| $D_h$       | hydraulic diameter, $2LD/(L + D)$                            |
| $D_o$       | diameter of rotameter tube base, $m$                         |
| $g$         | acceleration due to gravity, $m/s^2$                         |
| $Gr$        | Grashof number, $g\beta D_h^3 \delta T/\nu^2$                |
| $h$         | hydrostatic height, $m$                                      |
| $H$         | height of chamber, $m$ , thermophoretic coefficient          |



|             |   |
|-------------|---|
| $I$         | anemometer sensor current, amp  |
| $k$         | thermal conductivity, W/m·°C  |
| $K^*$       | static sensitivity, volts/°C  |
| $L$         | width of chamber, m   |
| $m$         | mass, kg  |
| $p^+$       | dimensional pressure, motion (static) and hydrostatic pressures, N/m <sup>2</sup> |
| $P$         | non-dimensional pressure, $(p^+ - p_o^+)/\rho W_{IN}^2$                           |
| $P$         | dimensional pressure for rotameter use, appendix, N/m <sup>2</sup>                |
| $Pe$        | Peclet number, $Re \cdot Pr$  |
| $Pr$        | Prandtl number, $\mu C_p/k$   |
| $q$         | signal amplitude  |
| $\bar{q}_c$ | conduction flux, $k \nabla T$   |
| $Q$         | rotameter volumetric flow rate, m <sup>3</sup> /s                                 |
| $Q_{IN}$    | inlet volumetric flow rate, m <sup>3</sup> /s                                     |
| $R$         | gas constant, J/kg·°K, resistance, ohm  |
| $Ra$        | Rayleigh number, $Gr \cdot Pr$  |
| $Re$        | inlet Reynolds number, $D_h W_{IN}/\nu$   |
| $S$         | heat source term  |
| $t$         | dimensional time, s   |
| $T$         | dimensional temperature, °C   |

|                |  |
|----------------|--|
| $T'$           | non-dimensional temperature, $(T_{IN} - T)/(T_{IN} - T_w)$ |
| $T_{IN}$       | inlet temperature, °C                                      |
| $T_{lwall}$    | left vertical end wall temperature, °C                     |
| $T_{rwall}$    | right vertical end wall temperature, °C                    |
| $T_{sw}$       | side wall temperature, °C (see Fig. 1 of chapter 1)        |
| $T_w$          | end wall temperature, °C (see Fig. 1 of chapter 1)         |
| $u$            | dimensional $x$ -direction velocity, m/s                   |
| $U$            | non-dimensional $x$ -direction velocity, $u/W_{IN}$        |
| $v$            | dimensional $y$ -direction velocity, m/s                   |
| $V$            | non-dimensional $y$ -direction velocity, chapter 1, m/s    |
| $V$            | fluid velocity or droplet terminal settling velocity, m/s  |
| $\vec{V}$      | velocity vector, m/s                                       |
| $V_{ch}$       | chamber volume, m <sup>3</sup>                             |
| $V_{max}$      | magnitude of maximum velocity, m/s                         |
| $\vec{V}_{th}$ | thermophoretic velocity vector, m/s                        |
| $\forall$      | volume, m <sup>3</sup>                                     |
| $w$            | dimensional $z$ -direction velocity, m/s                   |
| $W$            | non-dimensional $z$ -direction velocity, $w/W_{IN}$        |
| $W_{IN}$       | inlet vertical velocity, m/s                               |
| $z$            | dimensional horizontal coordinate, m                       |
| $X$            | non-dimensional horizontal coordinate, $z/D$               |

|      |   |
|------|---|
| $y$  | dimensional horizontal coordinate, rotameter ball position, m |
| $Y$  | non-dimensional horizontal coordinate, $y/L$                  |
| $Y'$ | experimental horizontal coordinate axis                       |
| $Z$  | non-dimensional vertical coordinate, $z/L$                    |

#### Greek letter symbols

|            |  |
|------------|--|
| $\alpha$   | thermal diffusivity, $\text{m}^2/\text{s}$   |
| $\beta$    | coefficient of thermal expansion, $\beta = -\frac{1}{\rho} \left( \frac{\partial \rho}{\partial T} \right)$ , $1/^\circ\text{K}$ |
| $\delta$   | boundary layer thickness, m  |
| $\delta P$ | $(P_2 - P_1)$ , $\text{N}/\text{m}^2$  |
| $\delta T$ | $(T_{IN} - T_w)$ , $^\circ\text{C}$  |
| $\epsilon$ | fractional change in dependent variable  |
| $\theta$   | non-dimensional time, $tQ_{IN}/V_{ch}$   |
| $\theta_o$ | $(T_{hot} - T_{cold})/T_{cold}$  |
| $\lambda$  | mean free path, m  |
| $\mu$      | dynamic viscosity or reference at inlet, $\text{kg}/\text{m}\cdot\text{s}$   |
| $\nu$      | kinematic viscosity or reference at inlet, $\mu/\rho$ , $\text{m}^2/\text{s}$  |
| $\rho$     | fluid density or reference at inlet, $\text{kg}/\text{m}^3$  |
| $\tau$     | time constant, s   |
| $\tau$     | stress tensor, $\mu \nabla \vec{V} + \mu (\nabla \vec{V})^T$ , $( )^T \equiv \text{transpose}$                                   |
| $\phi$     | dependent variable   |
| $\phi_s$   | dependent variable at specific sweep or time step  |

$\nabla T$  temperature gradient, °K/m

### Subscripts

o,1,2 reference location for rotameter pressure correction

o reference value for Boussinesq approximation

atm atmosphere reference

b rotameter ball

d droplet

f fluid

wire anemometer wire or film

## ACKNOWLEDGEMENT

I wish to acknowledge Drs. A. Faghri, W. Hankey, and R. Carpenter for their valuable contributions in the review and comments during the course of this study. Their insight and experience have proved to be invaluable to this research. I also wish to thank S. Thomas for his unbiased assistance and patience.

## STUDY INTRODUCTION

Large, low velocity chambers ( $\approx 1$  m diameter) have traditionally been used for studies investigating the toxic effects of various airborne compounds. Use of these chambers in toxicological studies have precluded detailed investigations utilizing computational fluid dynamics in conjunction with experimental data in determining the physics of chamber operation and performance in the development of the chamber flow structure. The series of studies contained herein address these issues by utilizing computational fluid dynamics and experimental data from both a scaled-down laboratory model and a full-size chamber typically used for toxicological studies. Internal heat sources, simulating biological heat sources have also been included and the effects on the developing flow structure with and without these internal heat sources investigated.

Chapter 1 addresses the development of the chamber flow structure without internal heat sources for a geometry typically used for toxicological studies. Chapter 2 includes the addition of internal heat sources and addresses the time-dependent effects on the development of the chamber flow structure. Both chapters 1 and 2 utilize computational fluid dynamics and experimental results from the scaled-down laboratory model. Finally, chapter 3 utilizes both computational fluid dynamics and flow visualization experiments conducted in the full-size chamber with and without internal heat sources.

## Chapter 1

# EXPERIMENTAL AND NUMERICAL SIMULATION OF MIXED CONVECTION IN LARGE BAFFLED RECTANGULAR CHAMBERS

### 1.1 Summary

An investigation to determine the effects of mixed convection on the flow structure of large baffled chambers for both "aided" and "opposed" buoyant forces has been completed. Experimental results were reported for momentum boundary layer thickness and temperature distribution within the chamber. Numerical results and experimental data were obtained for comparison. Two- and three-dimensional transient numerical models were formulated using a fully implicit finite-difference scheme of the laminar Navier-Stokes equations. The inlet and wall temperatures were held constant while maintaining a uniform inlet

velocity. Two tiers of four (two per tier) horizontal baffles were located axisymmetrically about the vertical axis with the inlet at the top and exhaust at the base of the chamber. The difference between the inlet and wall temperatures ranged between  $-1.0^{\circ}\text{C}$  to  $3.3^{\circ}\text{C}$  with a Prandtl number,  $Pr = 0.7$ , inlet Reynolds number,  $Re = 32$  and  $235$  and inlet Rayleigh number  $Ra = 0 - 6.8 \times 10^7$ . It was concluded that the flow patterns within these chambers are predominantly buoyant in nature with asymmetric behavior. The development of the flow structure was found to be sensitive to small variations in the temperature difference between the inlet and wall.

## 1.2 Introduction

Large baffled rectangular chambers with low inlet velocities have traditionally been used to study a variety of chemical atmospheres, generated for health effects studies, chemical reaction and chemical species formation studies, and aerosol characterization studies, Fig 1.1a. Generally, they have a cross-sectional diameter greater than 0.5 meter with an inlet velocity set to maintain 10-15 chamber volume changes per hour. The inlet and exhaust may be mounted vertically or horizontally with an array of internal baffles included for atmosphere dispersion purposes.

There have been many investigations concerning the Rayleigh-Bénard flow in confined and partially open enclosures with and without baffles or dividers



(Ostrach and Austin, 1988; Bajorek and Lloyd, 1982; Nansteel and Greif, 1981; Markatos and Malin, 1982). Such investigations have made use of both experimental and numerical results for information with regard to the temperature profile and flow structure in various closed cavity geometries with differing magnitudes of Grashof, Prandtl, and Rayleigh numbers. There have also been many investigations concerning mixed convective flow in pipe (Tanaka et al., 1987), inclined tubes (Choudhury and Patankar, 1983), vertical channels (Yao, 1983), spherical annuli (Ramadhyani et al., 1984), and vertical and horizontal plates (Ramachandran et al., 1988; Osborne and Incropera, 1985; Chiu and Rosenberger, 1987; Chiu et al. 1987), but there is little information with regard to mixed convective flow in large baffled chambers.

Mixed convection in heated vertical channels have shown some indication of the possible effects of both "aided" and "opposed" buoyant forces in larger geometries. Yao (1983) demonstrated that the "aided" buoyant forces for upward vertical channel flow tended to accelerate the boundary layer such that incoming flow was drawn toward the channel wall. Tanaka et al. (1987) also showed an increase in the wall boundary layer velocity with a decrease in Reynolds number for the case of "aided" buoyant forces in a uniformly heated pipe. These investigations indicate a shift in the major velocity component toward the pipe or channel walls as buoyant forces become significant. While these investigations indicate some possible effects of buoyant forces, the chambers of interest in addition to including baffles, also have inlet Reynolds numbers that are one to two

orders of magnitude lower, resulting in a flow structure that is predominantly buoyant in nature.

Initial investigations of these chambers incorporated flow visualization techniques using smoke and dyes to optimize the chamber geometry so that well-dispersed atmospheres could be obtained (Carpenter and Beethe, 1981; Moss, 1981). Quantitative approaches to determine the mean residence time of a chamber, the rate of dispersion within a chamber of a tracer gas, and the distribution within a chamber using vapors, droplets, and solid particles have also been done (Hemerway et al., 1982; Beethe et al., 1979; Moss, 1982; Yeh et al., 1986). These investigations, however, have not addressed the effects of mixed convection on the transport phenomenon of heat and mass transfer within these chambers. Information into the diffusion and convection of mass, enthalpy, and momentum within these chambers is of interest to better understand their operation and provide a basis for improvement, modification and future development.

A typical chamber, that may be used for the purposes described, consists of a conical inlet intended to uniformly distribute the atmosphere of interest across the inlet plane. The exhaust consists of a manifold to achieve uniform flow characteristics across the exhaust plane. Inlet and exhaust flow rates are controlled independently to maintain a slight negative chamber pressure with respect to the ambient pressure (2.5 - 5.1 cm  $H_2O$ ).

This investigation considers a simplified version of the aforementioned chamber. Of interest is the development of the flow structure due to a temperature

gradient between the inlet and wall temperature. Table 1.1 shows the scope of this investigation with both two- and three-dimensional numerical formulations (cases #1 - #6) and experimental results from a scaled-down laboratory experimental model (case #7) intended to be used as an indicator for use in the analysis of the larger, full-size chamber. For this investigation, the three-dimensional effects of the experimental model were considered and the corresponding three-dimensional numerical solutions were used to account for discrepancies between the experimental and two-dimensional numerical results. The two-dimensional numerical formulation is intended to correspond to the larger, full-size chamber with a depth of one meter and was compared to the experimental results. The vertical wall temperature,  $T_w$ , was assumed to be constant due to the thin wall construction. A typical range of Reynolds, Grashof, Rayleigh and Prandtl numbers at the inlet plane, assuming a uniform velocity distribution, are also shown in Table 1.1 where  $\delta T$  is taken to be the difference between the inlet temperature,  $T_{IN}$ , and the vertical wall temperature,  $T_w$ , with the characteristic length chosen to be the hydraulic diameter of the chamber body.

Initial verification of the magnitude of the buoyant forces compared to inertia forces was determined by finding the ratio of the buoyant forces to inertia forces. This was done by evaluating  $Gr/Re^2$  at the inlet plane. The buoyant forces were found to dominate the inertia forces by as much as three orders of magnitude with a temperature difference of  $\delta T = 1.0^\circ C$ . The dominate buoyant forces, therefore, must be considered as the primary force in development of the flow structure within these chambers.

### 1.3 Analysis

Both two- and three-dimensional numerical solutions of the incompressible time-dependent laminar Navier-Stokes equations were considered. The time-dependent approach was chosen to evaluate the presence of a steady periodic oscillation. The two- and three-dimensional problems shown in Fig. 1.1 were considered with the three-dimensional formulation simulating the experimental model. The additional third- dimensional wall is termed "side wall" while the constant temperature two- and three-dimensional vertical wall is termed "end wall".

For this investigation, only the dimensional form of the governing equations were solved, thereby circumventing the immediate need for scaling considerations of the non-dimensional parameters as is typically required for buoyant flow conditions (Ostrach and Austin, 1988). The non-dimensional form of the governing equations were derived using the scale length and characteristic velocity generally chosen for mixed convection pipe flow and the resultant non-dimensional parameters were compared using subsequent dimensional solutions.

The Boussinesq approximation was used in the vertical direction to account for buoyancy effects. Using this approximation the vertical body force becomes:

$$\vec{B}_z = \rho g [1 - \beta (T - T_{IN})]$$

where

$$\beta = \frac{1}{T_{IN}}$$

for an ideal gas.

For this investigation, the reference values for all of the gas properties were taken to be those at the inlet plane.

The chamber inlet cone was assumed to provide a uniform velocity distribution across the inlet plane with the exhaust manifold providing a velocity distribution resulting from a constant exhaust pressure across the outlet plane. Viscous dissipation and pressure work were assumed to be negligible due to the low buoyancy-induced velocities. With these assumptions, the three-dimensional governing equations become:

Conservation of mass:

$$\frac{\partial u}{\partial x} + \frac{\partial v}{\partial y} + \frac{\partial w}{\partial z} = 0 \quad (1.1)$$

Conservation of momentum:

$$\rho \left( \frac{\partial u}{\partial t} + u \frac{\partial u}{\partial x} + v \frac{\partial u}{\partial y} + w \frac{\partial u}{\partial z} \right) = -\frac{\partial p}{\partial x} + \mu \left( \frac{\partial^2 u}{\partial x^2} + \frac{\partial^2 u}{\partial y^2} + \frac{\partial^2 u}{\partial z^2} \right) \quad (1.2)$$

$$\rho \left( \frac{\partial v}{\partial t} + u \frac{\partial v}{\partial x} + v \frac{\partial v}{\partial y} + w \frac{\partial v}{\partial z} \right) = -\frac{\partial p}{\partial y} + \mu \left( \frac{\partial^2 v}{\partial x^2} + \frac{\partial^2 v}{\partial y^2} + \frac{\partial^2 v}{\partial z^2} \right) \quad (1.3)$$

$$\rho \left( \frac{\partial w}{\partial t} + u \frac{\partial w}{\partial x} + v \frac{\partial w}{\partial y} + w \frac{\partial w}{\partial z} \right) = - \frac{\partial p^+}{\partial z} + \mu \left( \frac{\partial^2 w}{\partial x^2} + \frac{\partial^2 w}{\partial y^2} + \frac{\partial^2 w}{\partial z^2} \right) + \rho g \beta (T - T_{IN}) \quad (1.4)$$

Conservation of energy:

$$\rho \left( \frac{\partial T}{\partial t} + u \frac{\partial T}{\partial x} + v \frac{\partial T}{\partial y} + w \frac{\partial T}{\partial z} \right) = \frac{k}{C_p} \left( \frac{\partial^2 T}{\partial x^2} + \frac{\partial^2 T}{\partial y^2} + \frac{\partial^2 T}{\partial z^2} \right) \quad (1.5)$$

Defining the non-dimensional parameters as follows;

$$\theta = tQ_{IN}/V_{ch} = tW_{IN}/H, \quad X = x/D, \quad Y = y/L, \quad Z = z/H,$$

$$U = u/W_{IN}, \quad V = v/W_{IN}, \quad W = w/W_{IN}, \quad T' = (T_{IN} - T)/(T_{IN} - T_{\infty}),$$

$$P = (p^+ - p_o^+) / \rho W_{IN}^2$$

The non-dimensional form of the governing equations can be derived in terms of the aspect ratios,  $A_1$ ,  $A_2$ , and  $A_3$ .

Conservation of mass:

$$A_2 \frac{\partial U}{\partial X} + \frac{\partial V}{\partial Y} + A_1 \frac{\partial W}{\partial Z} = 0 \quad (1.6)$$

Conservation of momentum:

$$\begin{aligned} & \frac{\partial U}{\partial \theta} + \left( \frac{A_2}{A_1} U \frac{\partial U}{\partial X} + \frac{1}{A_1} V \frac{\partial U}{\partial Y} + W \frac{\partial U}{\partial Z} \right) \\ &= -\frac{A_2}{A_1} \frac{\partial P}{\partial X} + \frac{A_3}{\text{Re}} \left( \left( \frac{A_2}{A_1} \right)^2 \frac{\partial^2 U}{\partial X^2} + \frac{1}{A_1^2} \frac{\partial^2 U}{\partial Y^2} + \frac{\partial^2 U}{\partial Z^2} \right) \end{aligned} \quad (1.7)$$

$$\begin{aligned} & \frac{\partial V}{\partial \theta} + \left( \frac{A_2}{A_1} U \frac{\partial V}{\partial X} + \frac{1}{A_1} V \frac{\partial V}{\partial Y} + W \frac{\partial V}{\partial Z} \right) \\ &= -\frac{1}{A_1} \frac{\partial P}{\partial Y} + \frac{A_3}{\text{Re}} \left( \left( \frac{A_2}{A_1} \right)^2 \frac{\partial^2 V}{\partial X^2} + \frac{1}{A_1^2} \frac{\partial^2 V}{\partial Y^2} + \frac{\partial^2 V}{\partial Z^2} \right) \end{aligned} \quad (1.8)$$

$$\begin{aligned} & \frac{\partial W}{\partial \theta} + \left( \frac{A_2}{A_1} U \frac{\partial W}{\partial X} + \frac{1}{A_1} V \frac{\partial W}{\partial Y} + W \frac{\partial W}{\partial Z} \right) = \\ & -\frac{\partial P}{\partial Z} + \frac{A_3}{\text{Re}} \left( \left( \frac{A_2}{A_1} \right)^2 \frac{\partial^2 W}{\partial X^2} + \frac{1}{A_1^2} \frac{\partial^2 W}{\partial Y^2} + \frac{\partial^2 W}{\partial Z^2} \right) + \frac{\text{Gr}T'}{A_3 \text{Re}^3} \end{aligned} \quad (1.9)$$

Conservation of energy:

$$\begin{aligned} & \frac{\partial T'}{\partial \theta} + \left( \frac{A_2}{A_1} U \frac{\partial T'}{\partial X} + \frac{1}{A_1} V \frac{\partial T'}{\partial Y} + W \frac{\partial T'}{\partial Z} \right) \\ &= \frac{A_3}{\text{Pr} \cdot \text{Re}} \left( \left( \frac{A_2}{A_1} \right)^2 \frac{\partial^2 T'}{\partial X^2} + \frac{1}{A_1^2} \frac{\partial^2 T'}{\partial Y^2} + \frac{\partial^2 T'}{\partial Z^2} \right) \end{aligned} \quad (1.10)$$

The boundary conditions were specified with the assumption that there is a uniform inlet velocity profile and the vertical end wall temperature is constant. The side walls were either at a fixed temperature,  $(T')_{\text{sw}} = 1/6$ , or adiabatic,  $(\partial T' / \partial x)_{\text{sw}} = 0$ , for the three-dimensional formulation. Only the magnitude of the inlet velocity is specified. The magnitude of the outlet velocity is such as

to satisfy the conservation of mass with a constant reference pressure across the outlet plane. With these considerations the boundary conditions become:

$$X = 0, 0 \leq Y \leq 1, 0 \leq Z \leq 1, (\partial T' / \partial x) = 0 \text{ or } T' = 1/6, U = 0,$$

$$V = 0, W = 0$$

$$X = 1, 0 \leq Y \leq 1, 0 \leq Z \leq 1, (\partial T' / \partial x) = 0 \text{ or } T' = 1/6, U = 0,$$

$$V = 0, W = 0$$

$$Y = 0, 0 \leq X \leq 1, 0 \leq Z \leq 1, T' = 1, U = 0, V = 0, W = 0$$

$$Y = 1, 0 \leq X \leq 1, 0 \leq Z \leq 1, T' = 1, U = 0, V = 0, W = 0$$

$$Z = 0, 0 \leq X \leq 1, 0 \leq Y \leq 1, T' = 0, U = 0, V = 0, W = 1$$

$$Z = 1, 0 \leq X \leq 1, 0 \leq Y \leq 1, U = 0, V = 0, P = 0$$

The outlet boundary condition for temperature was considered to be locally parabolic such that the Peclet number is sufficiently large so as to exhibit local one-way behavior in the axial direction. The baffles were treated as being infinitesimally thick with a no-slip boundary condition. The baffle temperature was specified to be that of the local fluid temperature.



## 1.4 Numerical Scheme

The numerical scheme used is a finite-difference iterative method of solution using a control-volume approach as developed by Spalding et al. (1980). Two- and three-dimensional numerical models were formulated using the fully implicit finite-difference scheme of the time dependent, laminar Navier-Stokes equations. The "SIMPLEST" (Spalding et al., 1980) method of solution for the momentum equations was used with the hybrid differencing formulation. When a cell Peclet number is within the range -2 to 2, a central-difference scheme is used and when the cell Peclet number is outside this range the upwind differencing scheme is used.

The outlet boundary condition for temperature was considered to be locally parabolic such that the Peclet number is sufficiently large so as to exhibit local one-way behavior in the axial direction (Patankar, 1980). This approach to specifying the outlet boundary condition for a dependent variable is generally accepted as the most available approach for internal flow problems in which the fluid leaves the calculation domain and the dependent variable of interest is unknown.

The baffles were treated as being infinitesimally thick with a no-slip boundary condition by setting the cell wall velocity to zero over the region of the

baffle location. The baffle temperature was specified to be that of the local fluid temperature.

The solution sequence involved solving for the velocity and temperature fields from an assumed pressure field at a specific time step. The pressure field was then subsequently updated using these velocity and temperature fields in the pressure-correction equation such that the conservation of mass was satisfied. This iterative sweep process was then repeated using a slab-by-slab method at each time step until convergence criteria were satisfied. Convergence characteristics at each time step were maintained by reducing the time step where appropriate with the minimum computational time required to reach a steady state solution being at least three characteristic times,  $H/W_{IN}$ , or approximately ten minutes. In addition, conditions for convergence to a solution, either at a specific time step or to a steady state solution, was based upon a dependent variable,  $\phi$ , varying less than a predetermined change of the magnitude fraction,  $\epsilon_\phi$ , between successive sweeps or time steps where:

$$|\phi_s - \phi_{s+1}| / \phi \leq \epsilon_\phi$$

The values of  $\epsilon_\phi$  were varied and it was required that the magnitude of the dependent variable be greater than the roundoff error or truncation error such as would happen when velocities approach zero. Typically, for a steady state solution,  $\epsilon_\phi$  ranged from  $1.0 \times 10^{-3}$  to  $1.0 \times 10^{-2}$  over a time span of 25 seconds, while over five successive sweeps  $\epsilon_\phi$  was less than  $1.0 \times 10^{-3}$ . Intermediate results were monitored to insure convergence and numerical stability at a specific time step during the course of the solution. These intermediate results were also

used to determine convergence toward either a steady state or a steady periodic solution.

Appropriate grid size and spacing was chosen to give acceptable numerical accuracy while still maintaining reasonable and acceptable computational times. Generally, the approach to organizing the grid layout for typical closed cavity buoyant problems has been to concentrate on an increased number of grids at the walls to accurately describe the thermal and momentum boundary layers. For the two-dimensional formulation, a uniform  $100 \times 100$  grid was chosen to give good coverage without knowing in advance as to where the greatest dependent variable gradients would be located within the chamber cavity. This grid layout was subsequently refined in regions of interest to verify numerical accuracy. Refining the grid by doubling the grid number at the vertical wall, a high gradient region, showed that the predicted maximum wall boundary layer velocity using the  $100 \times 100$  grid underestimated, to within 3 percent, the value obtained using the refined grid. The predicted momentum boundary layer thickness was less than 5 percent for boundary layers greater than 2.5 cm in thickness while the temperature was less than 1 percent of the value predicted using the refined grid.

While the  $100 \times 100$  grid in the two-dimensional formulation was found to be satisfactory, expansion to a three-dimensional formulation was found to be computationally intensive and time consuming. The third-dimension grid number was set to five to maintain reasonable computational times while still being able to qualitatively describe the general flow structure for the  $xx$  plane and thereby

address some of the inconsistencies between the numerical and experimental results.

Nusselt number was not evaluated since this only gives information regarding gross behavior and is insensitive to specific information regarding the flow structure and temperature distribution at various chamber locations such as the core region (Ostrach and Austin, 1988). This did not preclude evaluation of the Nusselt number to verify numerical convergence and optimum grid size but still only gave information for the numerical conditions at the chamber wall. In addition, there is an error associated with the Boussinesq approximation (Zhong et al., 1985) in which there is as much as a 20 percent overestimation of the maximum vertical velocity.

### 1.5 Experimental Approach

An experimental chamber model was fabricated using 1.91cm thick plexiglas with an interior body dimension of 0.813 m  $\times$  6.67 cm and 0.686 m high, Figs. 1.1b and 1.2. Baffles of 1.5 mm thick plexiglas were inserted across the chamber depth and fixed into the vertical side walls. The vertical end walls were fabricated using a thin aluminum plate combined with a water jacket to maintain a constant wall temperature. A Lauda recycling water bath was used to maintain a constant water temperature in the water jacket ( $\pm 0.2^\circ\text{C}$ ). Inlet and exhaust air was passed through a series of laminated porous stainless steel plates with a

nominal pore size of 44 microns to maintain a uniform velocity profile. The inlet volumetric flow rate was adjusted and monitored using a Matheson rotameter and corrected to account for the operational pressure drop. The chamber pressure was maintained to that of ambient by adjusting the exhaust flow rate.

Field temperature measurements were made using iron-constantan exposed junction thermocouples individually calibrated to within  $\pm 0.1^\circ\text{C}$ . Each thermocouple was immersed in a stirred water bath and calibrated using a standard NBS traceable thermometer (Ever Ready Thermometer Co., New York, N.Y.) ( $\pm 0.05^\circ\text{C}$ ) over the anticipated range of operation of  $24^\circ\text{C}$  to  $32^\circ\text{C}$ . An insulated isothermal thermocouple switch to minimize stray emf and thermocouple amplifier were used in conjunction with a digital voltmeter for a sensitivity greater than the required  $\pm 5.1 \mu\text{V}$  for  $\pm 0.1^\circ\text{C}$  measurements. Thermocouple voltages over a range of calibration temperatures were obtained and referenced to an ice point consisting of a large reservoir ice bath with an additional reference thermocouple to verify shifts in the reference ice point temperature. The resulting calibration was used to determine the field temperature during the course of experimentation. Periodically, the standard NBS traceable thermometer was also used to verify field temperatures of the experiment. Thermocouples were chosen and sized to minimize flow disturbances and maximize response time with a sheath diameter of 0.159 cm and a bead diameter ranging from 0.025 cm to 0.076 cm for a time constant of 1.35 to 1.73 seconds.

Velocity data was obtained using a TSI IFA-100 hot wire anemometer using a platinum film sensor model #1211-10. To effectively use the hot wire anemome-

ter, the magnitude of the buoyant-induced velocity, due to the heating of the sensor, in relation to the velocity to be measured was of interest. Uncertainty errors can be determined depending upon the orientation of the fluid velocity to that of the induced buoyant velocity as described by TSI (TSI TB 14). This is evident when the stream velocity is opposed to the sensor-induced buoyant velocity and of the same order of magnitude. During this experiment, there was a range of stream velocities in which the indicated sensor velocity would decrease as the stream velocity is increased. This is due to the counter acting velocities summing and indicating a lower resultant velocity. A spot calibration of the probe sensor using a series of parallel screens at isothermal conditions showed this velocity to be on the order of  $2.15 \times 10^{-2} \pm 0.25 \times 10^{-2}$  m/s. Therefore hot wire anemometry was limited to the evaluation of the momentum boundary layer thickness along the vertical end wall with the edge of the boundary layer being defined as this baseline velocity.

## 1.6 Results and Discussion

Experimental data from the experimental model consisted of temperature measurements at various chamber locations at the central plane and hot wire anemometry data to determine the momentum boundary layer thickness. These experimental data were then compared with results obtained from the three-dimensional numerical solutions, also at the central plane, to simulate this same

experimental model. Two-dimensional numerical solutions to simulate the full-size chamber were also compared to the same model experimental data and the corresponding three-dimensional numerical solutions.

To obtain similitude of the full-size chamber using the experimental model, the non-dimensional parameters,  $A_3/Re$ ,  $Gr/A_3Re^2$  and  $A_3/Pr \cdot Re$  were matched with the exception of the coefficient,  $A_2/A_1$ . The aspect ratio  $A_2$  was not considered for similitude of the full-size chamber and was either 0.813 or 12.2 for the full size chamber and experimental chamber respectively. As a result, the inlet velocity,  $W_{IN}$ , and temperature difference,  $\delta T$ , between the inlet and vertical end walls remained the same as that of the full-size chamber since only the chamber depth varied.

Figures 1.3-1.6 show the chamber velocity direction, velocity magnitude and temperature contours for the two-dimensional cases #1-#4. Figures 1.7-1.10 show the temperature contours and velocity vector and magnitude plots for the three-dimensional cases #5 and #6. Final comparisons of non-dimensional temperature are shown in Figs. 1.11 and 1.12 for the two-dimensional full size chamber case #4, the three-dimensional cases #5 and #6, and experimental results case #7. Momentum boundary layer thickness and maximum velocity for the cases investigated are shown in Table 1.2.

Three characteristic flow structures were observed for negative, positive and zero differences between the inlet and vertical wall temperatures. The three-

dimensional cases exhibited additional flow structure characteristics inherent to the third-dimensional boundary condition.

Negative differences between the inlet and vertical end wall temperatures induced "opposed" buoyant forces at the vertical end walls as shown in Figs. 1.3b and 1.4 for the two-dimensional case #2. The flow structure for this case consists of a central downward flowing core of cooler fluid with a reflux of mass at the vertical end walls from the exhaust to the inlet due to the upward vertical velocity component induced by the "opposed" buoyant forces. This reflux of mass subsequently combines with the cooler inlet mass at the inlet plane. The resulting flow structure was not only steady periodic in nature with a period on the order of 300 seconds, but was also displaced from the expected symmetrical flow pattern. Placement of the lower baffles in relation to the exhaust plane was found to be the contributing factor in the development of the oscillatory flow and the asymmetric flow structure. When these lower baffles were removed, the flow structure became symmetric with little oscillation.

Positive and increasing differences between the inlet and end wall temperatures resulted in a increased downward vertical velocity component at the vertical end walls with mass refluxing from the exhaust plane and flowing horizontally along the upper surface of the lower baffles. This is shown in Figs. 1.5-1.7 for the two-dimensional cases #3 and #4 and the three-dimensional adiabatic side wall case #5. As the temperature differences increased, both a thinning of the vertical wall boundary layer coupled with an increased vertical velocity component was observed as shown in Table 1.2. With this increase in the temperature



differential, the central vertical mass flow between the baffles was diminished as a result of an increased mass flux to the vertical end walls above the upper baffles.

There are two distinct regions of interest. The first regions of interest are the areas above the upper baffles, locations where flow is diverted around the baffles, and along the vertical end walls. In these areas, convection begins to dominate diffusion and becomes the primary mode of energy transport. This is demonstrated in the temperature contour plots of Figs. 1.5, 1.6, and 1.7 by the constant temperature region and the distorted contours between the baffles themselves and the chamber walls. The second, lower, region of interest is the area below the upper baffles and above the lower baffles where diffusion is the primary mode of energy transport as a result of the low velocity components. This is demonstrated by the stratified temperature gradient in the contour plots of Figs. 1.5, 1.6, and 1.7. This second region varies in size and will gradually diminish as the inlet and vertical end wall temperature differences are positive and decreasing to zero. With decreasing positive temperature differences, the central vertical mass flow between the baffles will increase. This mass will enter into the lower region and flow horizontally along the lower surface of the upper baffles toward the vertical end walls. As the temperature difference is further decreased, approaching zero, the flow will depict that of Fig. 1.3a in which the buoyant forces are no longer dominant.

Formulation of the three-dimensional case was considered such that the additional side walls for the third-dimension were either adiabatic case #5 or constant temperature case #6. With this formulation, a solution with a conduction side

wall boundary condition, as was anticipated using the experimental model, would be bordered by the two solutions with the side wall boundary condition being either adiabatic or constant temperature. For constant temperature side walls, the temperature was maintained less than the inlet temperature and greater than the vertical end wall temperature. Average experimental wall temperatures were obtained during the experimental testing and subsequently used as the boundary condition for the side wall temperature in the three-dimensional numerical formulation of case #6. For this case, the side wall temperature was maintained, satisfying the following relation for comparison to the non-dimensional temperature,  $T'$ :

$$(T_{IN} - T_{sw}) = T'(T_{IN} - T_w)$$

where  $T' = 1/6$

Comparison of the two-dimensional case #4 and the three-dimensional adiabatic side wall case #5 show a slight variation in the temperature contour plots (Figs. 1.6b and 1.7b.) attributed to the increased aspect ratio,  $A_2$  and the additional no-slip side wall boundary condition. Comparison of the solution of the three-dimensional constant side wall temperature case #6 to that of the three-dimensional adiabatic side wall case #5 and the two-dimensional case #4 showed a significant deviation in both the flow structure and temperature profile as shown in Figs. 1.6-1.8. This variation between the two three-dimensional solutions are attributed to differences in the side wall boundary conditions.

Additional effects of the third-dimension can be further demonstrated from Figs. 1.9 and 1.10. The three-dimensional adiabatic case #5 differs from the

two-dimensional formulation, case #4, in that the no-slip boundary condition is included along the side walls. The constant temperature side wall case #6 resulted in an increased boundary layer flow that is characteristic of the "aided" mixed convection flow in a pipe or channel. Case #6 also exhibited flow reversal in areas above the lower baffles and at the inlet. Both cases #5 and #6 showed rotational circulation below the lower baffles.

Non-dimensional temperature profiles for two-dimensional case #4 and three-dimensional cases #5 and #6 were compared with the experimental results case #7 and are shown in Figs. 1.11 and 1.12. In these figures, non-dimensional center plane temperatures along the chamber vertical axis are compared at lateral locations along the  $Y'$ -axis, where  $Y'=0$  is the centerline of the chamber and  $Y'=1$  the location of the vertical end wall. The two-dimensional case #4 consistently overestimated the non-dimensional temperature when compared to the three-dimensional adiabatic case #5. These differences in non-dimensional temperature were most evident for  $Z/H > 0.4$  and were also attributed to the increased aspect ratio,  $A_2$ , and the additional no-slip side wall boundary condition. There were significant differences between these two cases (#4 and #5), case #6 and the experimental results case #7. The experimental results, as expected, agree more with a conduction side wall boundary condition as opposed to the chosen adiabatic or constant temperature boundary conditions. A conjugate numerical formulation to account for the side wall boundary condition of third-dimension for comparison to the experimental results would be more appropriate

than the chosen boundary condition, but would require a significant increase in computational time.

Verification of the vertical end wall boundary layer thickness was performed using hot wire anemometry measurements. The numerical error in boundary layer thickness was taken to be one half of the grid size,  $\pm 0.41$  cm, and the experimental error  $\pm 0.32$  cm. Anemometer measurements were made by noting a change in the response from the zero baseline and the corresponding location from the vertical end wall determined to be the boundary layer thickness. This boundary layer thickness as defined was also determined from the numerical solutions of cases #3 - #6 and the results compared in Table 1.2 for the vertical non-dimensional locations at  $Z/H=0.44$  and  $Z/H=0.67$ . There was good agreement within error of both the experimentally determined boundary layer thickness and the numerically predicted boundary layer thickness.

## 1.7 Conclusions

Development of the chamber flow structure was found to be sensitive to small variations in the temperature difference between the inlet and wall. For positive temperature differences greater than  $1^{\circ}\text{C}$ , the entry above the upper baffles was sufficient such as to provide enough length for the flow to develop and combine in the boundary layer flow. Upper baffle placement in this instance appeared to have minimal effect upon the development of the resulting flow

structure. However, with gradually decreasing temperature differences, the baffle placement had significant impact upon the flow structure, eventually resulting in an asymmetric steady periodic behavior. There were also distinct regions of fluid and energy transport due either to diffusion or convection depending upon the location within the confines of the chamber. With increasing or decreasing temperature differentials, these areas were either enlarged or diminished as the flow structure developed with temperature being the driving parameter.

Use of the laboratory experimental model as an indicator in the evaluation of the flow structure in the larger, full-size chamber appeared to be limited due to the significant effects of the three-dimensional geometry. Effects of the additional side wall boundary condition appeared to have a significant effect upon the development of the flow structure within the model, significantly differing from the two-dimensional numerical solution.

In general, the observed variations in development of the flow structure from steady state to oscillatory behavior are consistent with laminar buoyant flow bifurcations for which Prandtl number, geometry, and Rayleigh number are the parameters influencing the flow structure at a specific bifurcation (Yang, 1988). Such appears to be the case with the development of the flow structure in the chambers investigated here. Variation in Rayleigh number due to the difference between the inlet and wall temperature in conjunction with either the baffle placement or chamber aspect ratios provided the means for these flow structure

transitions to occur. This resulted in the observed differences between the two-dimensional formulation to simulate the full-size chamber, the three-dimensional formulations and laboratory experimental model.

Table 1.1  
PARAMETRIC SPECIFICATIONS FOR NUMERICAL  
AND EXPERIMENTAL INVESTIGATION

| case # | Approach        | $T_{sw}$   | $T_w$ | $T_{IN}$ | $\delta T$ |
|--------|-----------------|------------|-------|----------|------------|
| 1      | 2D NUMERICAL    | N/A        | 24°C  | 24°C     | 0°C        |
| 2      | 2D NUMERICAL    | N/A        | 24°C  | 23°C     | -1°C       |
| 3      | 2D NUMERICAL    | N/A        | 24°C  | 25°C     | 1°C        |
| 4      | 2D NUMERICAL    | N/A        | 24°C  | 27.3°C   | 3.3°C      |
| 5      | 3D NUMERICAL    | adiabatic  | 24°C  | 27.3°C   | 3.3°C      |
| 6      | 3D NUMERICAL    | constant** | 24°C  | 27.3°C   | 3.3°C      |
| 7      | 3D EXPERIMENTAL | conducting | 24°C  | 27.3°C   | 3.3°C      |

| case # | Ra                         | Gr                         | Re   | $A_1$ | $A_2$ | $A_3$ |
|--------|----------------------------|----------------------------|------|-------|-------|-------|
| 1      | 0                          | 0                          | 235  | 1.19  | 0.813 | 1.31  |
| 2      | (-)*6.82 × 10 <sup>7</sup> | (-)*9.74 × 10 <sup>7</sup> | 235  | 1.19  | 0.813 | 1.31  |
| 3      | 6.82 × 10 <sup>7</sup>     | 9.74 × 10 <sup>7</sup>     | 235  | 1.19  | 0.813 | 1.31  |
| 4      | 2.25 × 10 <sup>8</sup>     | 3.21 × 10 <sup>8</sup>     | 235  | 1.19  | 0.813 | 1.31  |
| 5      | 5.84 × 10 <sup>5</sup>     | 8.35 × 10 <sup>5</sup>     | 32.3 | 1.19  | 12.2  | 0.180 |
| 6      | 5.84 × 10 <sup>5</sup>     | 8.35 × 10 <sup>5</sup>     | 32.3 | 1.19  | 12.2  | 0.180 |
| 7      | 5.84 × 10 <sup>5</sup>     | 8.35 × 10 <sup>5</sup>     | 32.3 | 1.19  | 12.2  | 0.180 |

\* negative sign signifies "opposed" and positive sign signifies "aided" buoyant force at vertical "end walls"

$$** T_{sw} = (T_{IN} - \delta T / 6) \text{ or } T' - 1/6$$

$$Pr = 0.7$$

$$W_{IN} = 4.1 \times 10^{-3} \text{ m/s}$$

Table 1.2  
BOUNDARY LAYER THICKNESS AND MAXIMUM VELOCITY

| case # | $V_{max}$             | $\delta^*$ , cm |            |            | characteristic  |
|--------|-----------------------|-----------------|------------|------------|-----------------|
|        |                       | $Z/H=0.44$      | $Z/H=0.67$ | error, cm  |                 |
| 1      | $2.81 \times 10^{-2}$ | N/A             | N/A        | N/A        | steady state    |
| 2      | $7.03 \times 10^{-2}$ | N/A             | N/A        | N/A        | steady periodic |
| 3      | $6.89 \times 10^{-2}$ | 2.38            | 2.84       | $\pm 0.41$ | steady state    |
| 4      | $1.03 \times 10^{-1}$ | 1.98            | 2.32       | $\pm 0.41$ | steady state    |
| 5      | $1.02 \times 10^{-1}$ | 1.93            | 2.31       | $\pm 0.41$ | steady state    |
| 6      | $1.16 \times 10^{-1}$ | 2.09            | 2.58       | $\pm 0.41$ | steady state    |
| 7      | not measured          | 1.91            | 2.54       | $\pm 0.32$ | steady state    |

\* $\delta$  determined to be the location for a velocity equivalent to the minimum response of the anemometer sensor ( $\approx 2.15 \times 10^{-2}$  m/s)





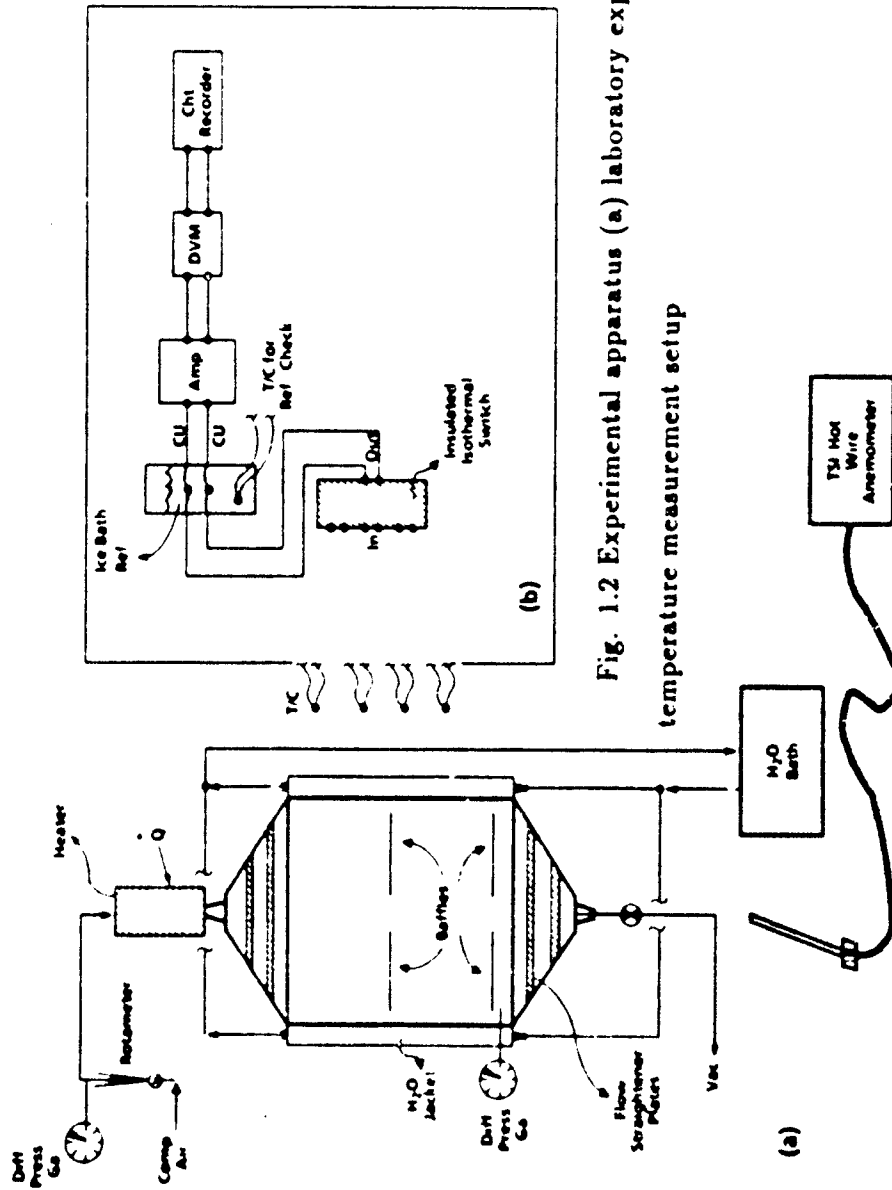


Fig. 1.2 Experimental apparatus (a) laboratory experimental model (b) temperature measurement setup

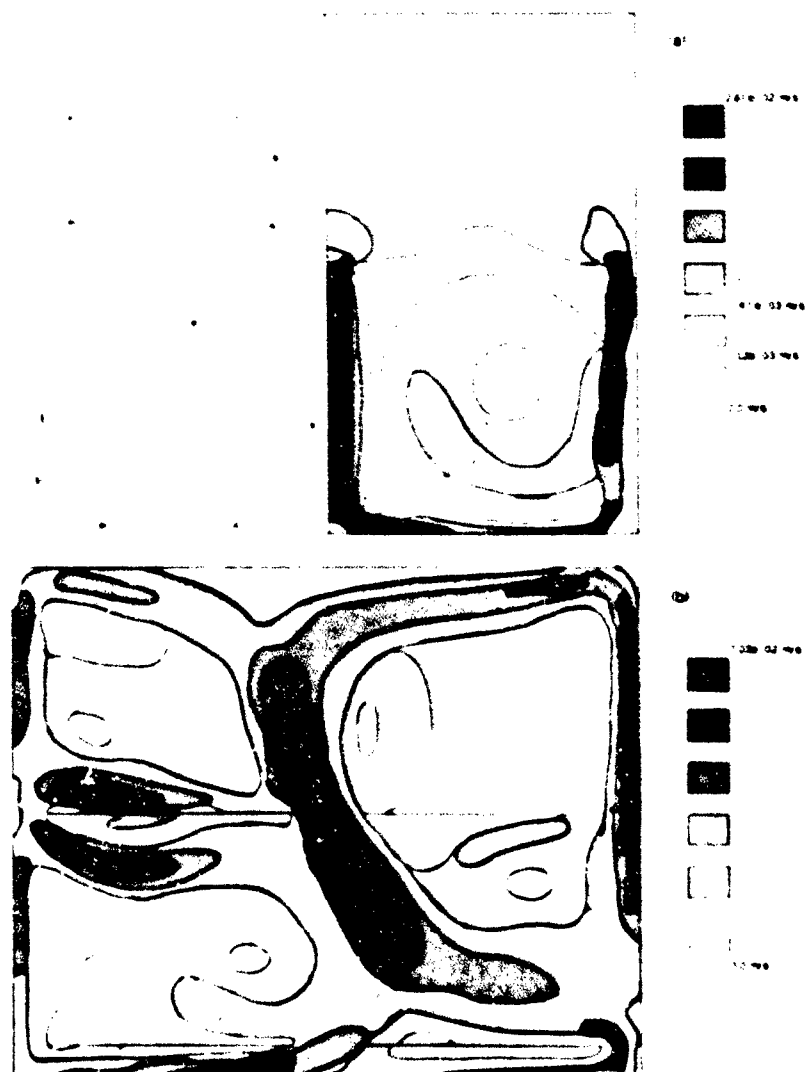


Fig. 1.3 Two-dimensional results (a) velocity direction and magnitude profile case #1 (b) velocity magnitude profile case #2

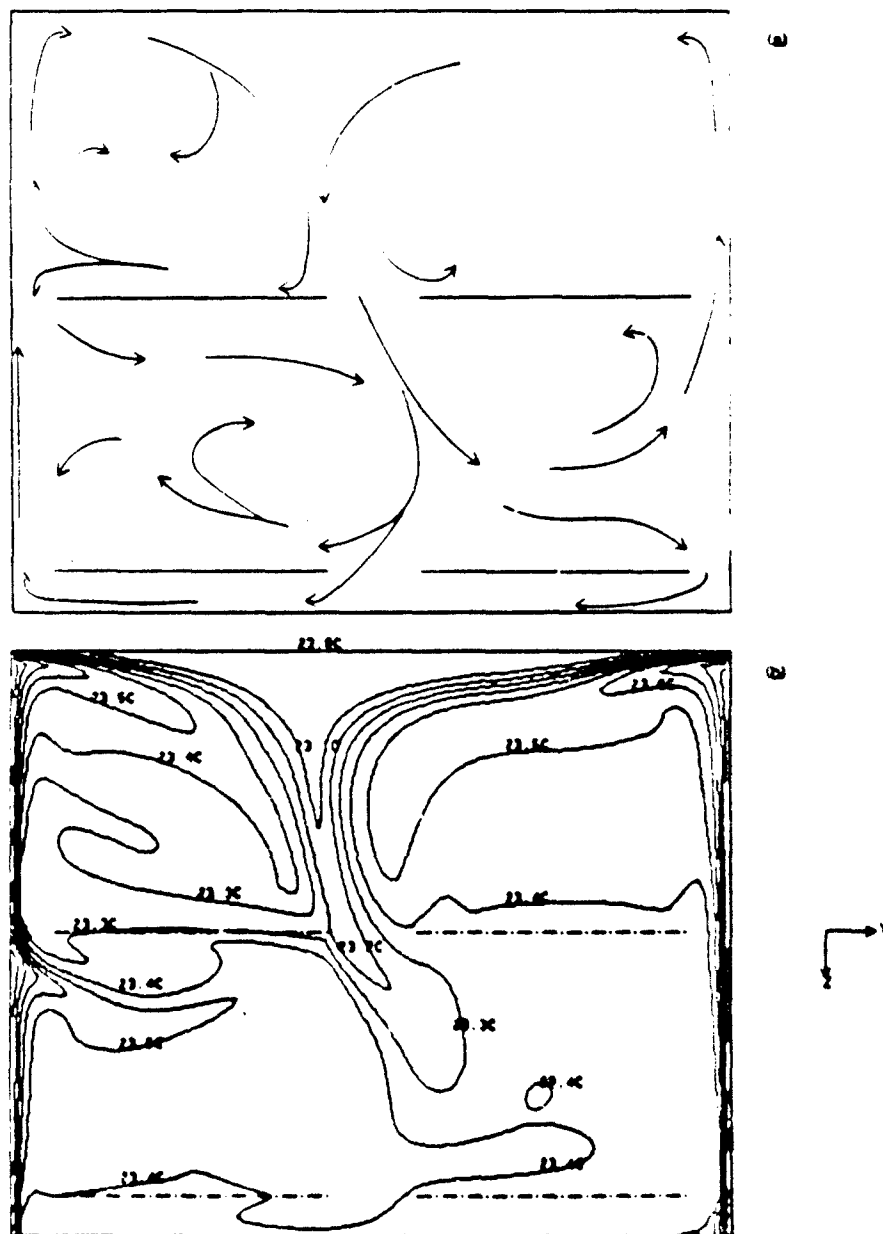


Fig. 1.4 Two-dimensional results for case #2 (a) chamber velocity direction profile (b) temperature contour

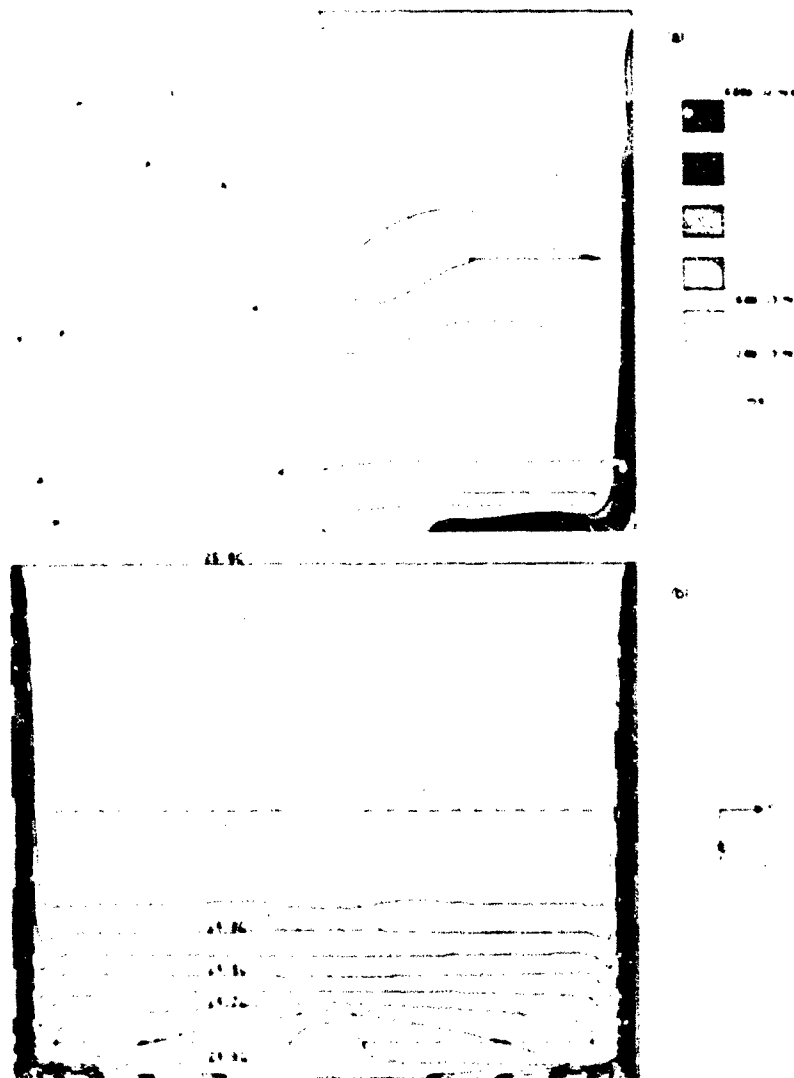


Fig. 1.5 Two-dimensional results for case #3 (a) chamber velocity direction and magnitude profile (b) temperature contour

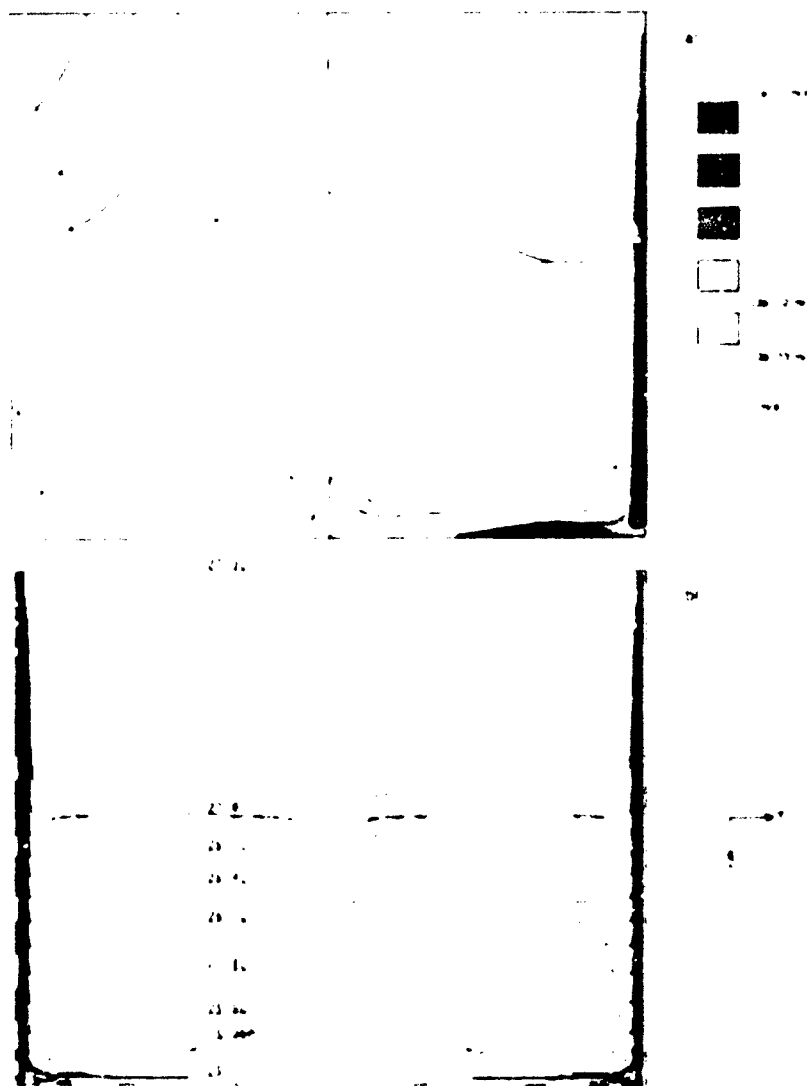


Fig. 1.6 Two-dimensional results for case #4 (a) chamber velocity direction and magnitude profile (b) temperature contour

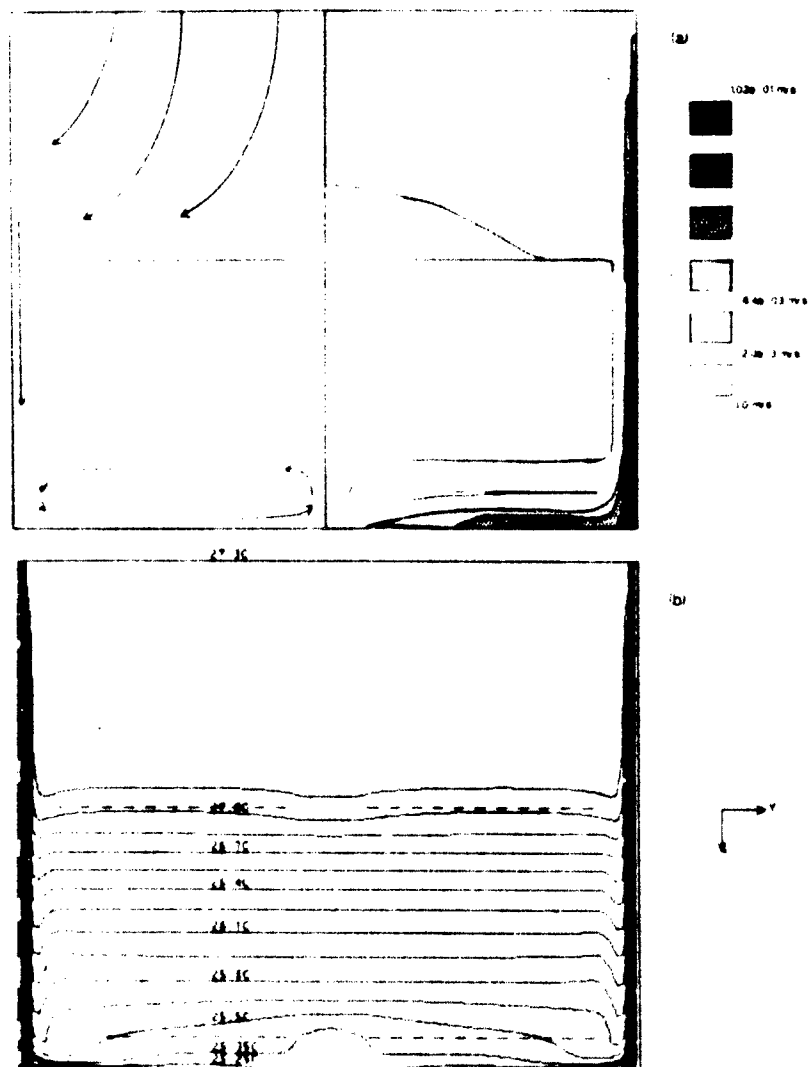


Fig. 1.7 Three-dimensional results for case #5 at center plane (a) chamber velocity direction and magnitude profile (b) temperature contour

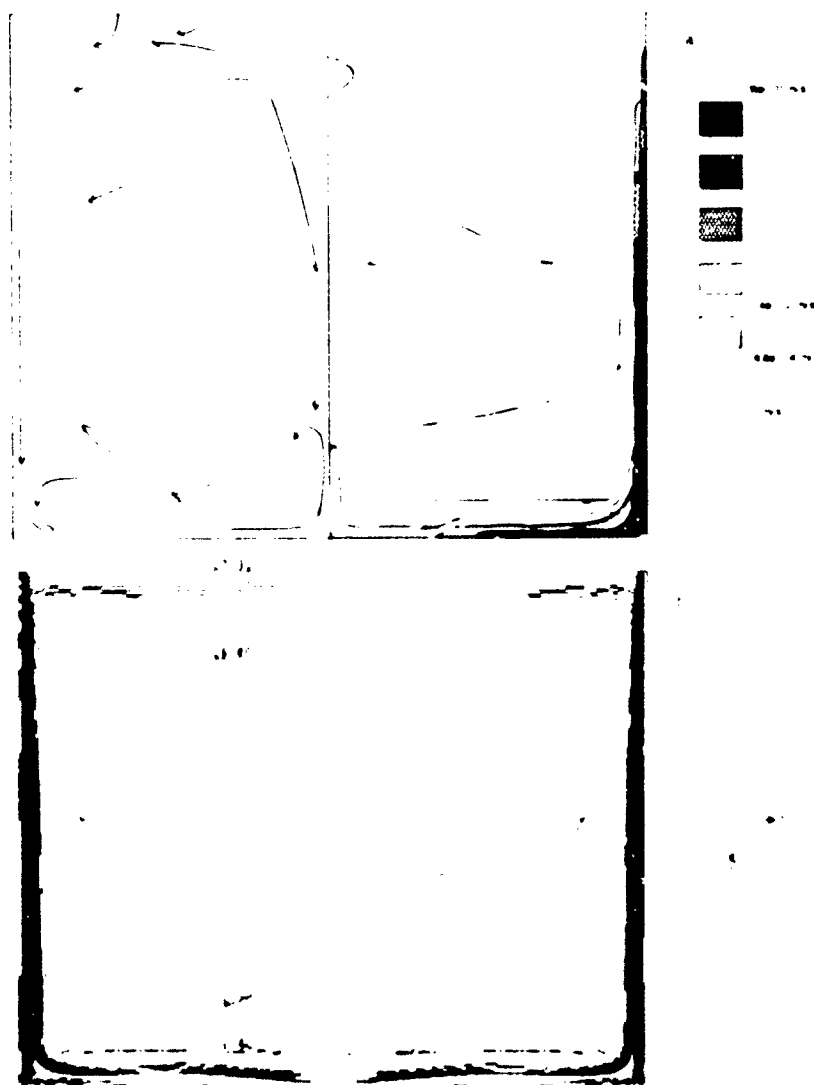


Fig. 1.8 Three-dimensional results for case #6 at center plane (a) chamber velocity direction and magnitude profile (b) temperature contour



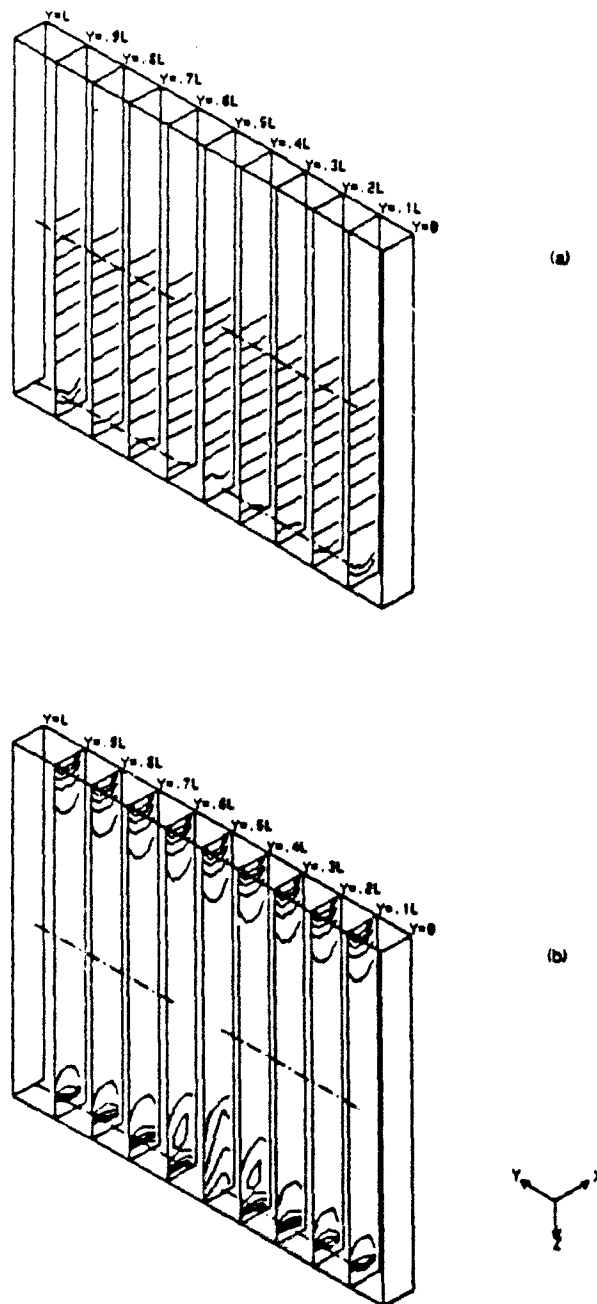


Fig. 1.9 Three-dimensional results, temperature contour (a) case #5, 0.2°C intervals, 25.3°C to 27.3°C (b) case #6, 0.1°C intervals, 26.3°C to 27.3°C

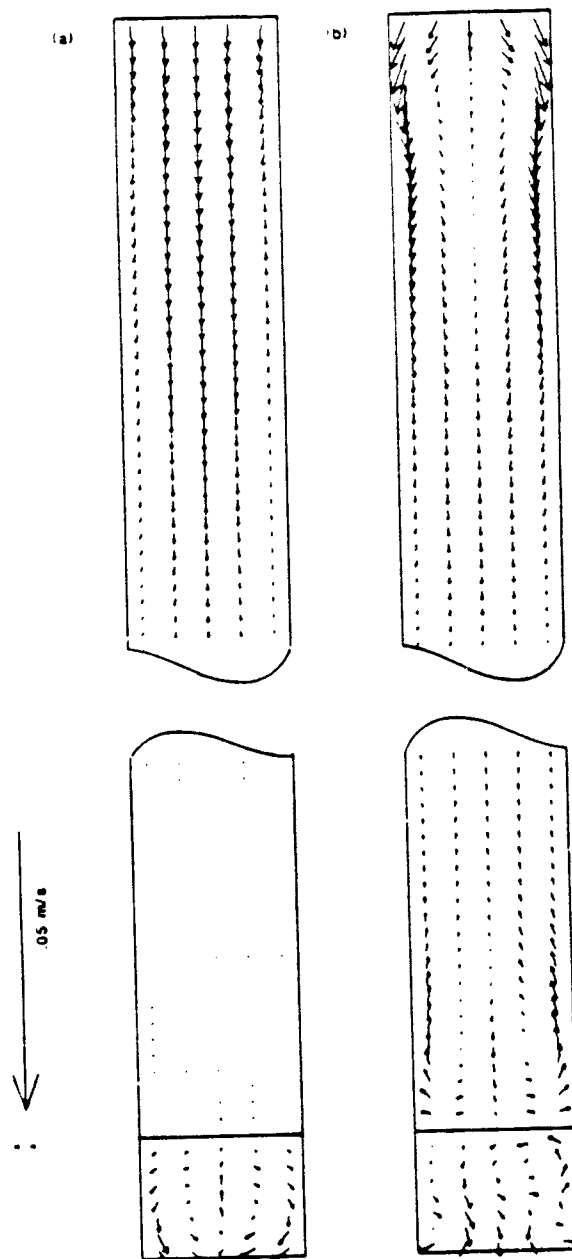


Fig. 1.10 Velocity vector plot across depth of three-dimensional numerical formulation at lateral distance  $.25L$  as viewed from the origin (a) case #5 (b) case #6

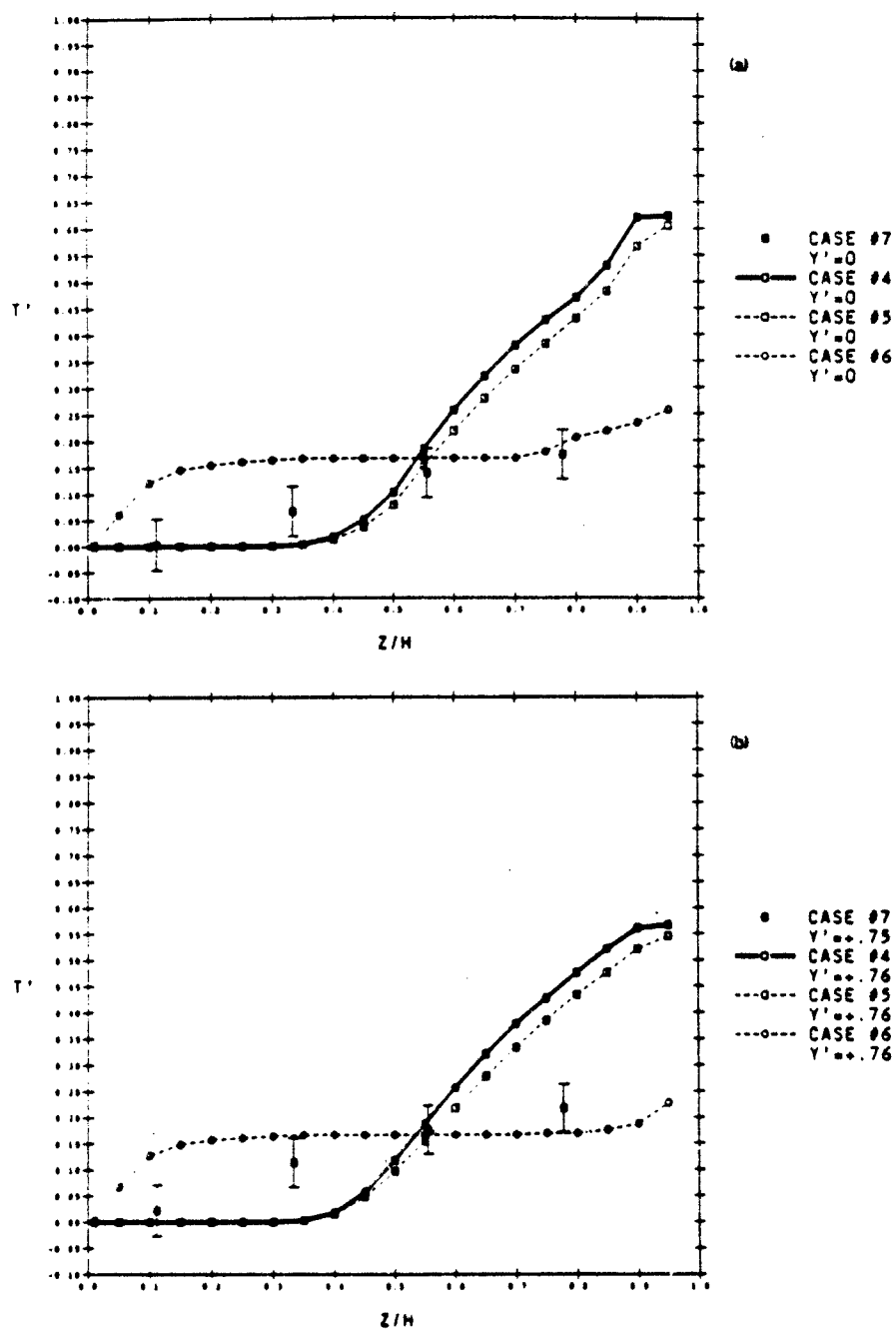


Fig. 1.11 Non-dimensional temperature vs. vertical height for two- and three-dimensions and experimental data along  $Y'$ -axis at central plane

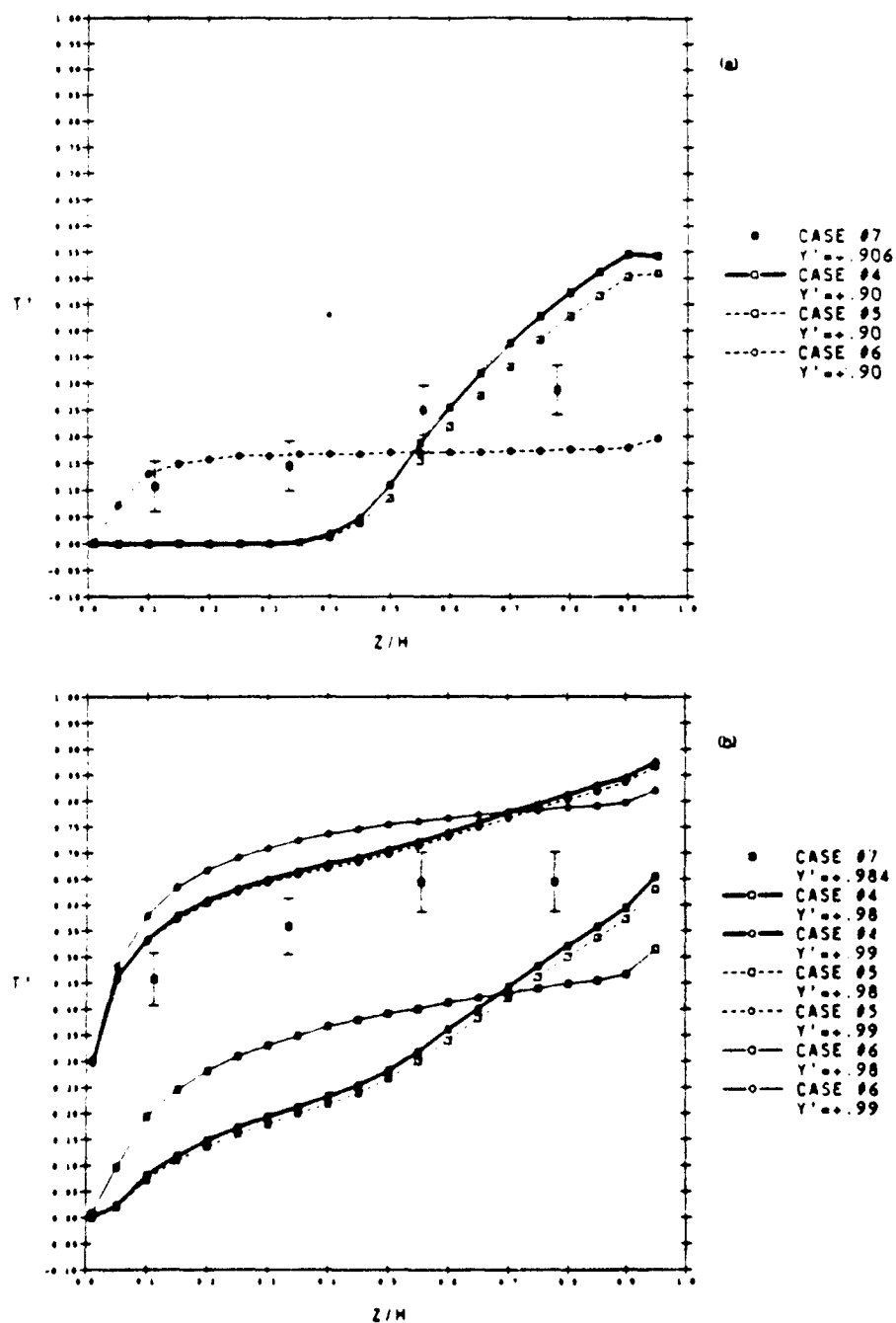


Fig. 1.12 Non-dimensional temperature vs. vertical height for two and three dimensions and experimental data along  $Y'$ -axis at central plane

## Chapter 2

### MIXED CONVECTION ANALYSIS IN LARGE BAFFLED RECTANGULAR CHAMBERS WITH INTERNAL HEAT SOURCES

#### 2.1 Summary

An investigation to determine the effects of mixed convection on the flow structure of large baffled chambers with internal heat sources has been completed. Baffles and internal heat sources were placed symmetrically about the vertical axis while maintaining a constant and uniform inlet velocity, inlet temperature, and wall temperature of  $4.1 \times 10^{-3}$  m/s, 27°C and 24°C respectively. Time dependent experimental and two-dimensional numerical results were compared at various chamber locations to demonstrate the transition of the flow

structure through a sequence of bifurcations with increasing internal heat source temperature up to 32°C.

Phase-space and frequency plots of temperature and velocity for the numerical solutions showed that there were characteristic harmonics, amplitude, and phase-space shapes at the various chamber locations. The three-dimensional experimental laboratory model demonstrated a transition of the flow structure from one that is steady state to periodic, aperiodic and finally chaotic with increasing internal heat source temperature. Three-dimensional experimental results also exhibited unique harmonics and amplitude of temperature and velocity at various chamber locations. Although differing from the two-dimensional numerical results at the same chamber locations, the harmonics observed from the three-dimensional experimental model showed similar frequency behavior and trends to that of the two-dimensional numerical results.

## 2.2 Introduction

Large baffled rectangular chambers with low inlet velocities have traditionally been used to study a variety of chemical atmospheres generated for health effects and biological studies, chemical reaction and chemical species formation studies, and aerosol characterization studies. Generally, they have a cross-sectional diameter greater than .5 meter with an inlet velocity set to maintain 10-15 chamber volume changes per hour. The inlet and exhaust may be mounted vertically

or horizontally with an array of internal baffles included for atmosphere dispersion purposes. Additional capabilities include cage units for housing laboratory animals for a variety of biological research applications.

There have been many investigations concerning the Rayleigh-Bénard flow in confined and partially open enclosures with and without baffles or dividers and internal or wall heat sources (Bajorek and Lloyd, 1982; Markatos and Malin, 1982; Powe and Warrington, 1983; Nansteel and Greif, 1981; Sparrow, et al., 1984; Warrington and Powe, 1985; November and Nansteel, 1987; Lee and Goldstein, 1988; Ostrach and Austin, 1988). Such investigations have made use of both experimental and numerical results for information with regard to the temperature profile and flow structure in various closed cavity geometries with differing magnitudes of Grashof, Prandtl, and Rayleigh numbers.

Yang (1988) discussed the buoyant enclosure problem as a dissipative dynamic system whose flow structure development is one of a series of bifurcations brought about by the driving parameters of Rayleigh number, Prandtl number, and enclosure geometry. Development of a flow structure from one that is steady state, periodic in time, aperiodic, and finally chaotic are examples of specific bifurcations that may be expected with variation in Rayleigh number, Prandtl number, and altered geometry. Yang (1988) further discussed the use of an attractor, a concept used in nonlinear dynamics, to describe the temporal asymptotic behavior of a trajectory in the phase space corresponding to a specific bifurcation.

Initial investigations of these chambers incorporated flow visualization techniques using smoke and dyes to optimize the chamber geometry so that well-dispersed atmospheres could be obtained (Carpenter and Beethe, 1981; Moss, 1981). Quantitative approaches to determine the mean residence time of a chamber, the rate of dispersion within a chamber of a tracer gas, and the distribution within a chamber using vapors, droplets, and solid particles have also been done (Hemenway et al., 1982; Beethe et al., 1979; Moss, 1982; Yeh et al., 1986). Most recently, Yerkes et al. (1989) investigated the mixed convection in large baffled rectangular chambers and the characteristic flow structure development for "aided" and "opposed" buoyant forces. Development of the chamber flow structure was found to be predominantly buoyant in nature and sensitive to small variations in the temperature difference between the inlet and wall varying from steady state to asymmetric oscillatory behavior. These investigations, however, have not addressed the effects of mixed convection with internal biological heat sources on the transport phenomenon of heat and mass transfer within these chambers. Information into the diffusion and convection of mass, enthalpy, and momentum within these chambers with the biological heat sources are of interest to better understand their operation and provide a basis for improvement, modification and future development.

A typical chamber that may be used for the purposes described consists of a conical inlet intended to uniformly distribute the atmosphere of interest across the inlet plane. The exhaust consists of a manifold to achieve uniform flow characteristics across the exhaust plane. Inlet and exhaust flow rates are



controlled independently to maintain a slight negative chamber pressure with respect to the ambient pressure (2.5 - 5.1 cm H<sub>2</sub>O). Biological heat sources may consist of a variety of laboratory animal species and are housed in uniformly spaced cage units located directly over the baffles.

This investigation considers a simplified version of the aforementioned chamber. Of interest is the transient behavior and development of the flow structure due to a temperature gradient between the biological heat sources, inlet temperature and wall temperature. Results from a time dependent two-dimensional numerical formulation were compared to experimental results from a scaled-down laboratory experimental model intended to be used as an indicator for use in the analysis of the larger, full-size chamber. The two-dimensional numerical formulation corresponded to the larger, full-size chamber differing from that of the experimental laboratory model in that the depth is 1.0 m compared to 6.67 cm for the model. The vertical end wall temperature,  $T_w$ , was assumed to be constant and equal to 24°C due to the thin wall construction. The inlet temperature was also assumed to be constant across the inlet plane and equal to 27°C.

Biological heat sources were treated as a constant temperature surface at 32°C and of a size and mass that would be appropriate for a 200 gm to 300 gm rat in a confined enclosure (Mauderly, 1986). It was assumed that physiological control of the body temperature is sufficient to maintain a constant body temperature in the low air velocities within the confines of the chamber.

Typical values of Grashof, Rayleigh and Reynolds numbers for this study were  $Gr = 2.02 \times 10^6$ ,  $Ra = 1.42 \times 10^6$  and  $Re = 32$  and  $235$  using the inlet hydraulic diameter,  $D_h$ , as the characteristic length (the two-dimensional formulation assumes chamber depth of one meter while the experimental model has a depth of 6.67 cm thereby resulting in different Reynolds numbers due to the differing hydraulic diameters). The difference in temperature was taken to be the maximum difference between the vertical end wall temperature and the biological heat source temperature,  $\delta T = 8.0^\circ\text{C}$ , with an inlet velocity of  $4.1 \times 10^{-3}$  m/s. With these values for Grashof, Rayleigh and Reynolds numbers, the development of the flow structure is predominately buoyant in nature with the buoyant forces dominating the inertia forces.

### 2.3 Analysis

Two-dimensional numerical solutions of the incompressible time-dependent laminar Navier-Stokes equations were calculated in accordance with the two-dimensional problem shown in Fig. 2.1a. For this investigation, only the dimensional form of the governing equations were solved, thereby circumventing the immediate need for scaling considerations of the non-dimensional parameters as is typically required for buoyant flow conditions (Ostrach and Austin, 1988). The Boussinesq approximation was used in the vertical direction to account for buoyancy effects. Using this approximation the vertical body force becomes:

$$\bar{B}_z = \rho \bar{g} [1 - \beta (T - T_{IN})]$$

where

$$\beta = \frac{1}{T_{IN}}$$

for an ideal gas.

For this investigation, the reference values for all of the gas properties were taken to be those at the inlet plane.

The chamber inlet cone was assumed to provide a uniform velocity distribution across the inlet plane with the exhaust manifold providing a velocity distribution resulting from a constant exhaust pressure across the outlet plane. Viscous dissipation and pressure work were assumed to be negligible due to the low buoyancy-induced velocities. With these assumptions, the two-dimensional governing equations become:

Conservation of mass:

$$\frac{\partial v}{\partial y} + \frac{\partial w}{\partial z} = 0 \quad (2.1)$$

Conservation of momentum:

$$\rho \left( \frac{\partial v}{\partial t} + v \frac{\partial v}{\partial y} + w \frac{\partial v}{\partial z} \right) = - \frac{\partial p^+}{\partial y} + \mu \left( \frac{\partial^2 v}{\partial y^2} + \frac{\partial^2 v}{\partial z^2} \right) \quad (2.2)$$

$$\rho \left( \frac{\partial w}{\partial t} + v \frac{\partial w}{\partial y} + w \frac{\partial w}{\partial z} \right) = - \frac{\partial p^+}{\partial z} + \mu \left( \frac{\partial^2 w}{\partial y^2} + \frac{\partial^2 w}{\partial z^2} \right) + \rho g \beta (T - T_{IN}) \quad (2.3)$$

Conservation of energy:

$$\rho \left( \frac{\partial T}{\partial t} + v \frac{\partial T}{\partial y} + w \frac{\partial T}{\partial z} \right) = \frac{k}{C_p} \left( \frac{\partial^2 T}{\partial y^2} + \frac{\partial^2 T}{\partial z^2} \right) \quad (2.4)$$

The boundary conditions were specified with the assumption that there is a uniform inlet velocity profile and the vertical end wall temperature is constant. Only the magnitude of the inlet velocity is specified. The magnitude of the outlet velocity is such as to satisfy the conservation of mass with a constant reference pressure across the outlet plane.

The outlet boundary condition for temperature was considered to be locally parabolic such that the Peclet number is sufficiently large so as to exhibit local one-way behavior in the axial direction. The baffles were treated as being infinitesimally thick with a no-slip boundary condition. The baffle temperature was specified to be that of the local fluid temperature.

Boundary conditions:

Inlet:  $t \geq 0$ ,  $v = 0$ ,  $w = W_{IN} = 4.1 \times 10^{-3}$  m/s,  $T = T_{IN} = 27^\circ\text{C}$

Vertical end wall:  $t \geq 0$ ,  $v = 0$ ,  $w = 0$ ,  $T = T_w = 24^\circ\text{C}$

Baffle:  $t \geq 0, v = 0, w = 0$

Heat sources:  $t \geq 0, T = 32^\circ\text{C}$

Outlet:  $t \geq 0, v = 0, p^+ = 0$

For this investigation, two restart fields were chosen for the initial conditions of the field dependent variables. The method for obtaining the restart fields are discussed in the following section.

## 2.4 Numerical Scheme

The numerical scheme used is a finite-difference iterative method of solution using a control-volume approach as developed by Spalding et al. (1980). The two-dimensional numerical model was formulated using a fully implicit finite-difference scheme of the time dependent, laminar Navier-Stokes equations. The "SIMPLEST" (Spalding et al., 1980) method of solution for the momentum equations was used with the hybrid differencing formulation. When a cell Peclet number is within the range -2 to 2, a central-difference scheme is used and when the cell Peclet number is outside this range the upwind differencing scheme is used.

The outlet boundary condition for temperature was considered to be locally parabolic such that the Peclet number is sufficiently large so as to exhibit local one-way behavior in the axial direction (Patankar, 1980). This approach to specifying the outlet boundary condition for a dependent variable is generally accepted as the most available approach for internal flow problems in which the fluid leaves the calculation domain and the dependent variable of interest is unknown.

The baffles were treated as being infinitesimally thick with a no-slip boundary condition by setting the cell wall velocity to zero over the region of the baffle location. The baffle temperature was specified to be that of the local fluid temperature. Heat sources were "blocked" by setting the cell velocity components within the heat source region to zero and fixing to a constant temperature.

The solution sequence involved solving for the velocity and temperature fields from an assumed pressure field at a specific time step. The pressure field was then subsequently updated using these velocity and temperature fields in the pressure-correction equation such that the conservation of mass was satisfied. This iterative sweep process was then repeated using a slab-by-slab method at each time step until convergence criteria were satisfied. Convergence characteristics at each time step were maintained by reducing the time step where appropriate. Conditions for convergence to a solution, either at a specific time step or to a steady state solution, was based upon a dependent variable,  $\phi$ , varying less than a predetermined change of the magnitude fraction,  $\epsilon_\phi$ , between successive

sweeps or time steps where:

$$|\phi_s - \phi_{s+1}| / \phi \leq \epsilon_\phi$$

The values of  $\epsilon_\phi$  were varied and it was required that the magnitude of the dependent variable be greater than the roundoff error or truncation error such as would happen when velocities approach zero. Typically,  $\epsilon_\phi$  was less than  $1.0 \times 10^{-3}$  for five successive sweeps. Intermediate results were monitored to insure convergence and numerical stability at a specific time step during the course of the solution. These intermediate results were also used to determine convergence toward either a steady state or a steady periodic solution.

Appropriate grid size and spacing and numerical time step was chosen to give acceptable numerical accuracy while still maintaining reasonable and acceptable computational times. Due to the complexity of the flow structure, the errors as a result of grid size and time step were determined first, by comparing the shape of the flow structure for similarity with a previous solution at a larger time step or grid size. Secondly, random locations throughout the chamber were selected and the average error compared between the similar solutions such that halving the time step resulted in a less than a three percent error in the dependent variable over the time span of interest and decreasing the grid size by ten percent resulted in less than a one percent error in the dependent variable. For this problem, a uniform  $100 \times 100$  grid was chosen to give good coverage with a time step of 0.010 seconds.

Initially the solution was started from a zero velocity and constant temperature field. The time step was gradually reduced once the solution became oscillatory in nature either due to numerical perturbations or naturally occurring oscillations due to the physics of the problem. Two restart fields for velocity, temperature and pressure were then chosen from these solutions and the time dependence behavior observed over a span of forty seconds using the final reduced time step of 0.010 seconds.

With the development of the relatively complex transient flow structure, both decreasing the grid size and time step would reveal both additional wavelengths and frequencies that would otherwise not be observed with a larger grid size and time step. In addition, error propagation in the solution with the progression of time would tend to numerically oscillate the solution with some numerically induced low frequency harmonics. Increasing the grid number and reducing time step is the appropriate response to correcting and revealing these additional wavelengths and harmonics and decreasing time step related propagation errors. Due to the physical size of the problem, however, this would significantly increase the computational time in solving the problem. Realizing these numerical limitations in obtaining solutions to a random and marginally stable problem such as presented here requires such numerical solutions to be used with care.



## 2.5 Experimental Approach

An experimental chamber model was fabricated using 1.91cm thick plexiglas with an interior body dimension of 0.813 m  $\times$  6.67 cm and 0.686 m high, Figs. 2.1b and 2.2. Baffles of 1.5 mm thick plexiglas were inserted across the chamber depth and fixed into the vertical side walls. The vertical end walls were fabricated using a thin aluminum plate combined with a water jacket to maintain a constant wall temperature. A Lauda recycling water bath was used to maintain a constant water temperature in the water jacket ( $\pm 0.2^\circ\text{C}$ ). Heat sources were simulated using flask heating mantles (Glas-col) located symmetrically approximately 1.4 cm above the baffles and maintained at constant temperature ( $\pm 0.5^\circ\text{C}$ ). Inlet and exhaust air was passed through a series of laminated porous stainless steel plates with a nominal pore size of 44 microns to maintain a uniform velocity profile. The inlet volumetric flow rate was adjusted and monitored using a Matheson rotameter and corrected to account for the operational pressure drop. The chamber pressure was maintained to that of ambient by adjusting the exhaust flow rate.

Field temperature measurements were made using iron-constantan exposed junction thermocouples individually calibrated to within  $\pm 0.1^\circ\text{C}$ . Each thermocouple was immersed in a stirred water bath and calibrated using a standard NBS traceable thermometer (Ever Ready Thermometer Co., New York, N.Y.) ( $0.05^\circ\text{C}$ ) over the anticipated range of operation of  $24^\circ\text{C}$  to  $32^\circ\text{C}$ . An insulated

isothermal thermocouple switch to minimize stray emf and thermocouple amplifier were used in conjunction with a digital voltmeter for a sensitivity greater than the required  $\pm 5.1 \mu\text{V}$  for  $\pm 0.1^\circ\text{C}$  measurements. Thermocouple voltages over a range of calibration temperatures were obtained and referenced to an ice point consisting of a large reservoir ice bath with an additional reference thermocouple to verify shifts in the reference ice point temperature. The resulting calibration was used to determine the field temperature during the course of experimentation. Periodically, the standard NBS traceable thermometer was also used to verify field temperatures of the experiment.

Thermocouples were chosen and sized to minimize flow disturbances and maximize response time with a sheath diameter of 0.159 cm and a bead diameter ranging from 0.025 cm to 0.076 cm for a time constant of 1.35 to 1.73 seconds. Assuming a maximum time constant of 1.7 seconds, the frequency response for measuring a .017 Hz (1 cycle/60 s) signal would result in a .985 attenuation with a  $-10^\circ$  phase shift.

Velocity data was obtained using a TSI IFA-100 hot wire anemometer using a platinum film sensor model #1211-10 with a frequency response of 300 kHz. To effectively use the hot wire anemometer, the magnitude of the buoyant-induced velocity, due to the heating of the sensor, in relation to the velocity to be measured was of interest. Uncertainty errors can be determined depending upon the orientation of the fluid velocity to that of the induced buoyant velocity as described by TSI (TSI TB 14). This is evident when the stream velocity is either opposed to or in the same direction and of the same order of magnitude as the

sensor-induced buoyant velocity. During this experiment, the range of stream velocities encompassed the sensor-induced velocity, limiting the use of the hot wire anemometer from quantitatively evaluating the velocity magnitude to evaluating the frequency behavior of the velocity at various chamber locations.

The laboratory experimental chamber was operated in such a manner so as to observe the development of the transient behavior of both temperature and velocity at six chamber locations (Fig. 2.1). Initially the chamber was started from a steady state initial condition without heat sources and with an inlet velocity,  $W_{IN}$ , of  $4.1 \times 10^{-3}$  m/s. The heat sources were gradually brought to 32°C while maintaining the inlet temperature,  $T_{IN}$ , and vertical wall temperature,  $T_w$ , at 27°C and 24°C respectively. Temperature and velocity data were obtained at the six chamber locations until the chamber appeared to maintain a steady periodic state in which the magnitude and oscillatory behavior of velocity and temperature remained constant. It was found that simultaneous measurements of velocity and temperature at the same chamber location induced temperature measurement errors due to the hot wire anemometer probe, therefore, measurement of temperature and velocity were obtained at differing chamber locations. Further temperature sampling artifacts due to the hot wire anemometer probe were verified to be negligible by relocating the hot wire anemometer probe to another chamber location while fixing the thermocouple chamber location.

## 2.6 Results and Discussion

Experimental data from the laboratory model consisted of time-dependent temperature and hot wire anemometry measurements at various chamber locations about the central plane to determine the transient behavior of temperature and velocity. These experimental data were then compared with results obtained from the transient two-dimensional numerical solutions.

Figures 2.3 and 2.4 show typical two-dimensional numerical solutions for velocity and temperature at a time  $t=t_0$  and  $t=t_0+30s$  respectively. Figure 2.5 shows the two-dimensional numerical time-dependent variation of temperature and velocity for six chamber locations,  $[(.50L, .31H), (.50L, .82H), (.70L, .31H), (.70L, .62H), (.90L, .11H), (.90L, .72H)]$ . These numerical solutions were initiated, as discussed in the numerical scheme, from the two arbitrarily chosen initial restart fields spanning a forty second time frame. Shown in Fig. 2.6 are the numerical solution phase-space shapes which are plotted as the rate of change of the dependent variable, velocity and temperature, versus the dependent variable over time. Experimentally obtained temperature and velocity information with increasing heat source temperature at chamber location  $(.70L, .31H)$  are shown in Fig. 2.7 and at the six chamber locations, Fig. 2.8. In these figures, 48 second snapshots were taken at 10 minute intervals for 120 minutes to demonstrate the transient behavior of the chamber as the heat source temperature is increased. These experimental data are also compared to the time-dependent velocity obtained from the numerical results which are also shown in Fig. 2.8.

Development of the flow structure, Figs. 2.3 and 2.4, was found to be time-dependent in nature with the formation of four Bénard cells in the upper portion

of the chamber above the upper baffles and heat sources. Over the course of time, these cells dissipated and reformed resulting in an oscillating core flow between the two upper baffles. A high velocity wall boundary layer flow was maintained on the vertical end wall increasing in thickness as the core flow dissipated. Bénard cells also formed between the upper and lower sets of baffles although the formation of these cells appeared to be influenced by the core flow. There was a reflux of mass between the vertical walls and upper baffles that was also influenced by the oscillating core flow which in turn influenced the formation of the Bénard cells above the upper baffles and heat sources. This behavior resulted in a marginally stable and oscillatory flow structure.

Two-dimensional numerical results showed the temperature and velocity to behave in an oscillatory nature with some incommensurable harmonics at the six chamber locations investigated, Fig. 2.5. The magnitude and frequency of the oscillations were shown to be dependent upon the chamber location and the proximity of that chamber location to a Bénard cell. The greatest oscillatory behavior occurred at the chamber centerline between the upper baffles, with the core flow developing and subsequently dissipating as a result of the Bénard cell formation above the upper baffles and heat sources. Temperature and velocity tended to be inversely proportional as would be expected in flow structures driven by buoyant forces with a fluid Prandtl number approaching one for which the rate that the velocity profile develops is equivalent to the rate that the thermal profile develops, Figs. 2.5a, 2.5b, and 2.5d. However, Figs. 2.5c, 2.5e, and 2.5f

did not show this behavior possibly due to the proximity of the chamber location to the movement of the low velocity core of a Bénard cell.

Phase-space or attractor plots of temperature and velocity, shown in Fig. 2.6, exhibited unique shapes at the six chamber locations resulting from a combination of steady state behavior which is represented by a fixed point in the phase-space, periodic behavior which is represented by a limit cycle in the phase-space and aperiodic behavior which is represented by a torus in the phase-space of temperature and velocity.

The experimental results demonstrated the transition of the flow structure through specific bifurcations, with the heat source temperature being the driving parameter for these transitions to occur. Figure 2.7 illustrates this behavior at chamber location  $(.70L, .31H)$ . With an increasing heat source temperature, the velocity was shown to pass through transitions from steady state, periodic, aperiodic, and finally chaotic or random oscillatory behavior with high frequency incommensurable harmonics. Figure 2.8 compares the experimentally obtained temperature and velocity harmonics at the six chamber locations to the velocity harmonics obtained from the two-dimensional numerical results. The oscillatory behavior of temperature was significantly attenuated due to the frequency response of the thermocouples and therefore difficult to resolve and compare with velocity. However, the velocity behavior demonstrated unique differences in harmonics between the the six chamber locations.

Experimental results showed chamber location  $(.70L, .62H)$ , Fig. 2.8e, to have the greatest variation in velocity while chamber location  $(.50L, .82H)$ , Fig. 2.8d, the least. This is opposite to the numerical results which showed the greatest variation in velocity to be at chamber locations  $(.50L, .31H)$  and  $(.50L, .82H)$  and the least variation in velocity at chamber location  $(.70L, .62H)$ . Experimental results, however, did show that chamber location  $(.50L, .31H)$ , Fig. 2.8a, to have the greatest variation in velocity second to chamber location  $(.70L, .62H)$ , Fig. 2.8e, agreeing with the numerical results as to being one of the two chamber locations with the greatest velocity variation.

The experimental results showed unique transient behavior at each of the six chamber locations. Transition of velocity through a series of bifurcations showed a unique behavior in both amplitude and harmonics up to and including the steady oscillatory behavior. Experimental results also indicated a marginally stable flow structure that appeared to be easily perturbed by heat source temperature. Comparison of the numerically obtained velocity results to the experimentally obtained velocity data show good agreement in harmonic behavior for chamber locations  $(.50L, .31H)$ ,  $(.90L, .11H)$  and  $(.90L, .72H)$  in Figs. 2.5a, 2.5c and 2.5f, respectively. The numerical results appeared to have less high frequency harmonics than the experimental results due in part to possible numerical damping. Comparison of the numerical and experimental results for chamber locations  $(.50L, .82H)$ ,  $(.70L, .31H)$  and  $(.70L, .62H)$  in Figs. 2.5d, 2.5b and 2.5e, respectively, showed poor agreement in the harmonic behavior of velocity.

Verification of the high velocity boundary layer region was performed by traversing the hot wire anemometer probe toward the vertical end wall. The location of this high velocity region was determined when there was an observable increase in the indicated velocity from that of a baseline velocity outside the confines of the high velocity region. Figure 2.9 shows the results of these measurements confirming the presence of a high velocity region between the vertical end wall and  $0.64 \pm 0.16$  to  $1.27 \pm 0.16$  cm with a vertical location of  $0.67H$ .

Efforts to utilize numerical solutions for a time-dependent comparison of experimental results in a random and marginally stable flow structure resulted in the comparison of numerical and experimental techniques that are each limited. The numerical grid size and time step increment appropriate to capture wave lengths and frequency harmonics of the problem limit the numerical solution to a problem such that with continued decreases in grid size and time step increment, additional wavelengths and harmonics would continually be revealed while significantly increasing the computational solution time. Experimental techniques in the measurement of low velocities and small temperature differences resulted in either velocity measurements being affected by velocity sensor-induced velocities and attenuated temperature measurements as a result of the thermocouple frequency response. However, with these limitations the numerical and experimental results obtained demonstrate similar harmonics and qualitative time-dependent behavior of the developing flow structure.

## 2.7 Conclusions



Comparison the experimental results to the two-dimensional numerical solutions revealed the third dimension of the laboratory experimental model to have a significant effect upon the developing flow structure, thus inducing time-dependent behavior differing from that of the two-dimensional numerical solutions. This was exhibited in both the oscillatory behavior at various chamber locations as well as the decreased amplitude in harmonics of all the chamber locations. However, there do appear to be unique harmonics and time-dependent behavior at each of the chamber locations as the flow structure passes through a transition of specific bifurcations.

The observed variations in flow structure from steady state to oscillatory behavior are consistent with laminar buoyant flow bifurcations for which Prandtl number, geometry, and Rayleigh number are the parameters to influence the flow structure at a specific bifurcation (Yang, 1988). Transition from a stable, steady state flow structure to one that is periodic in time, aperiodic, and finally chaotic are examples of specific bifurcations that may be expected with variation in Rayleigh number, Prandtl number, and altered geometry. Such appears to be the case with the development of the flow structure in the chambers investigated here. Variation in Rayleigh number due to the differences between the the internal heat source temperature, inlet temperature and wall temperature in conjunction with either the baffle placement or chamber aspect ratios provided the means for these flow structure transitions to occur. This resulted in the observed differences between the two-dimensional formulation and laboratory experimental model.

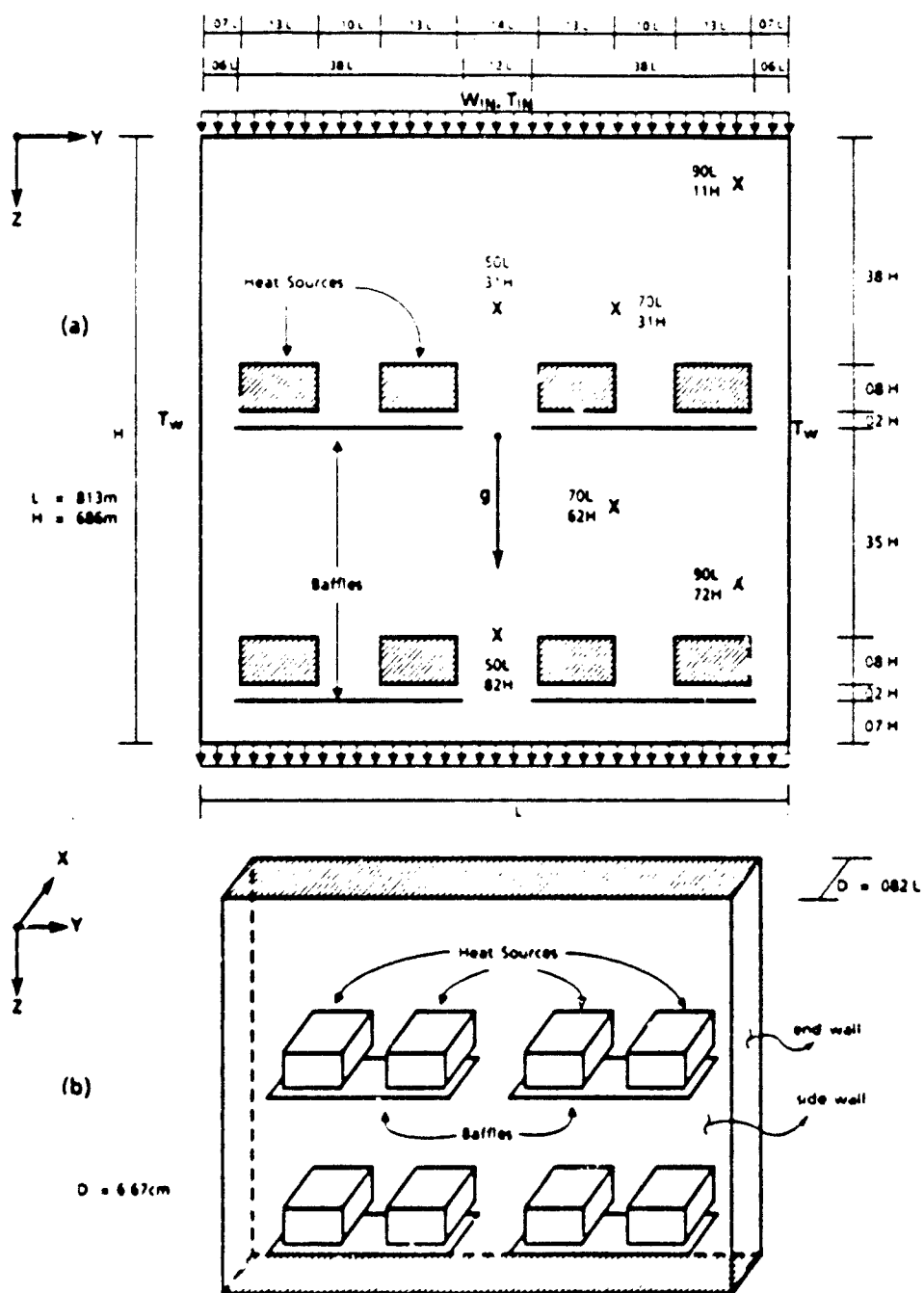


Fig. 2.1 Chamber geometry specifications (a) two-dimensional geometry  
(b) three-dimensional laboratory model geometry

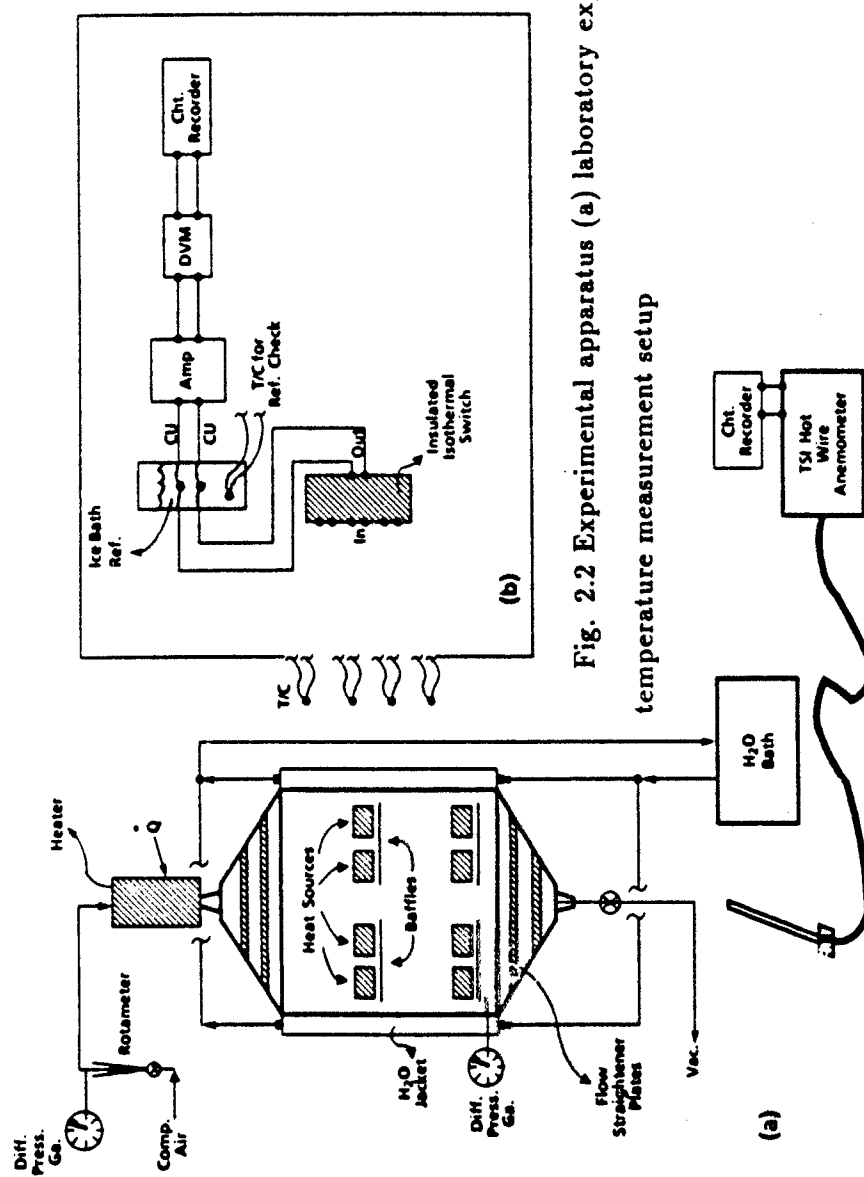


Fig. 2.2 Experimental apparatus (a) laboratory experimental model (b) temperature measurement setup

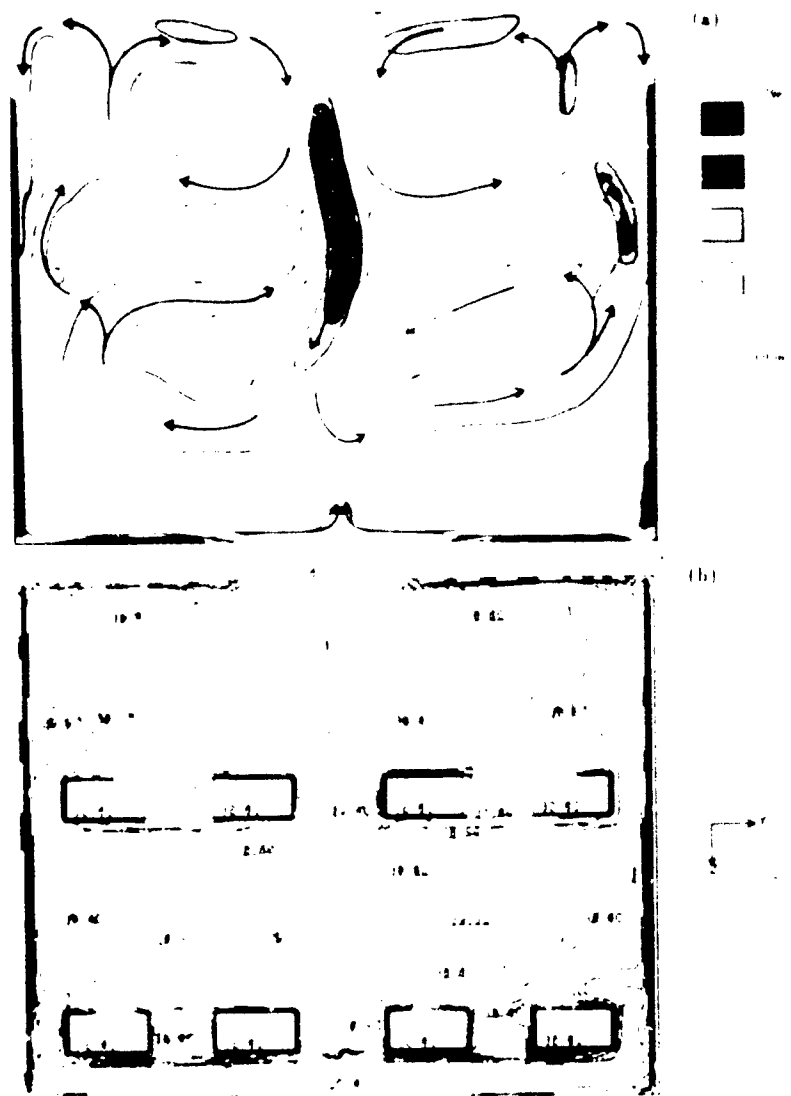


Fig. 2.3 Two-dimensional numerical results at time  $t=t_0$ . (a) chamber velocity direction and magnitude profile (b) temperature contour



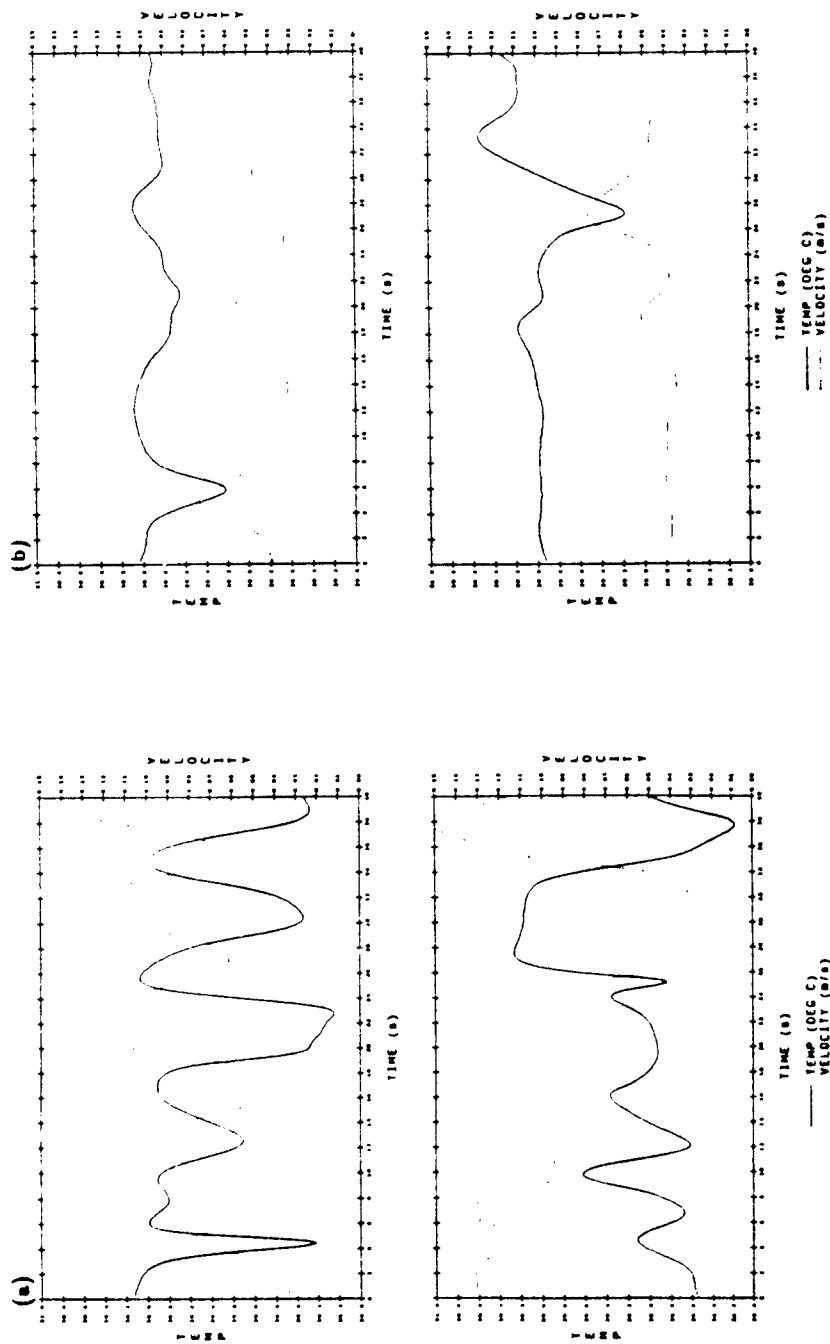


Fig. 2.5 Two-dimensional numerical time-dependent plots of velocity and temperature (a) (.50L, .31H) (b) (.70L, .31H) (c) (.90L, .11H) (d) (.50L, .82H) (e) (.70L, .62H) (f) (.90L, .72H)

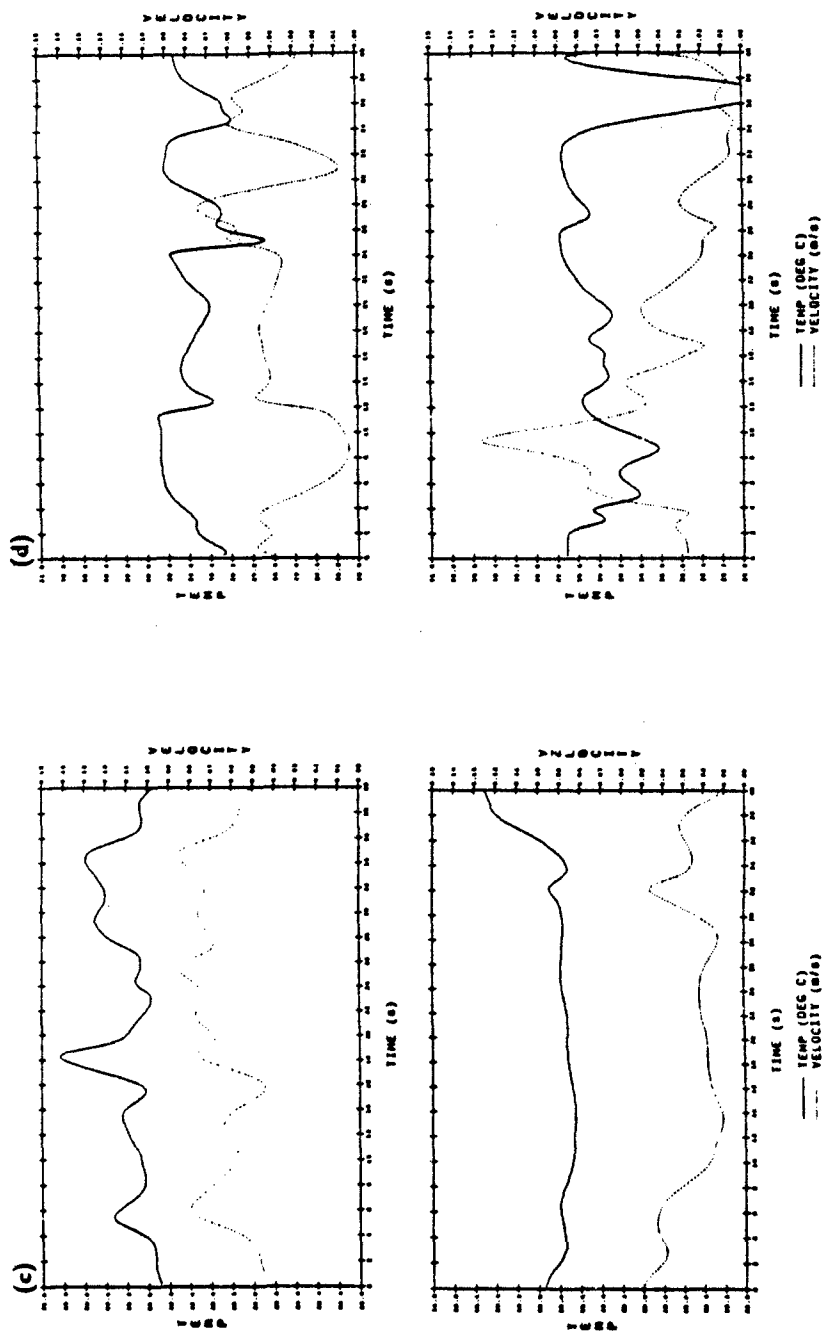


Fig. 2.5 Two-dimensional numerical time-dependent plots of velocity and temperature (a) (.50L, .31H) (b) (.70L, .31H) (c) (.90L, .11H) (d) (.50L, .82H) (e) (.70L, .62H) (f) (.90L, .72H)

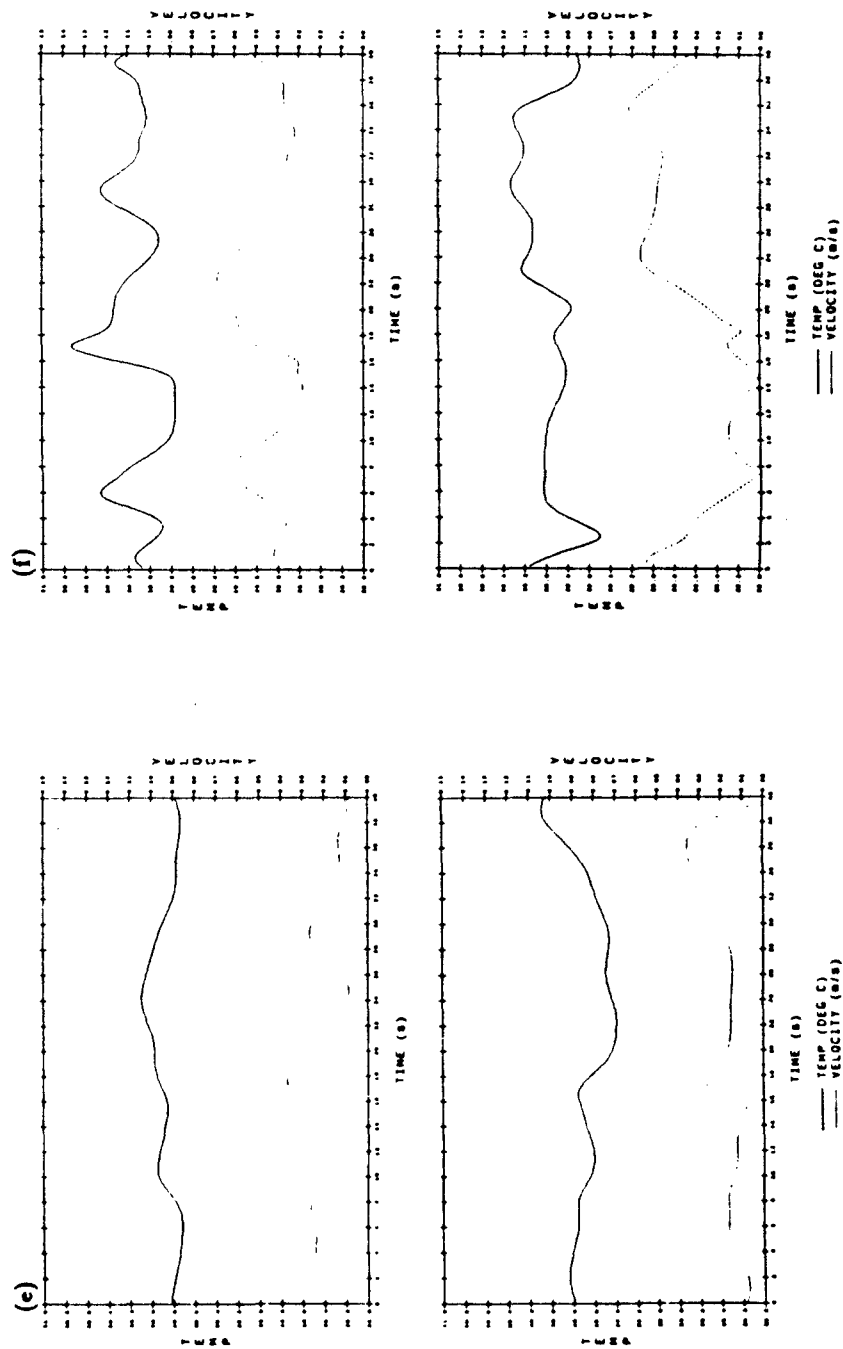


Fig. 2.5 Two-dimensional numerical time-dependent plots of velocity and temperature (a) (.50L, .31H) (b) (.70L, .31H) (c) (.90L, .11H) (d) (.50L, .82H) (e) (.70L, .62H) (f) (.90L, .72H)



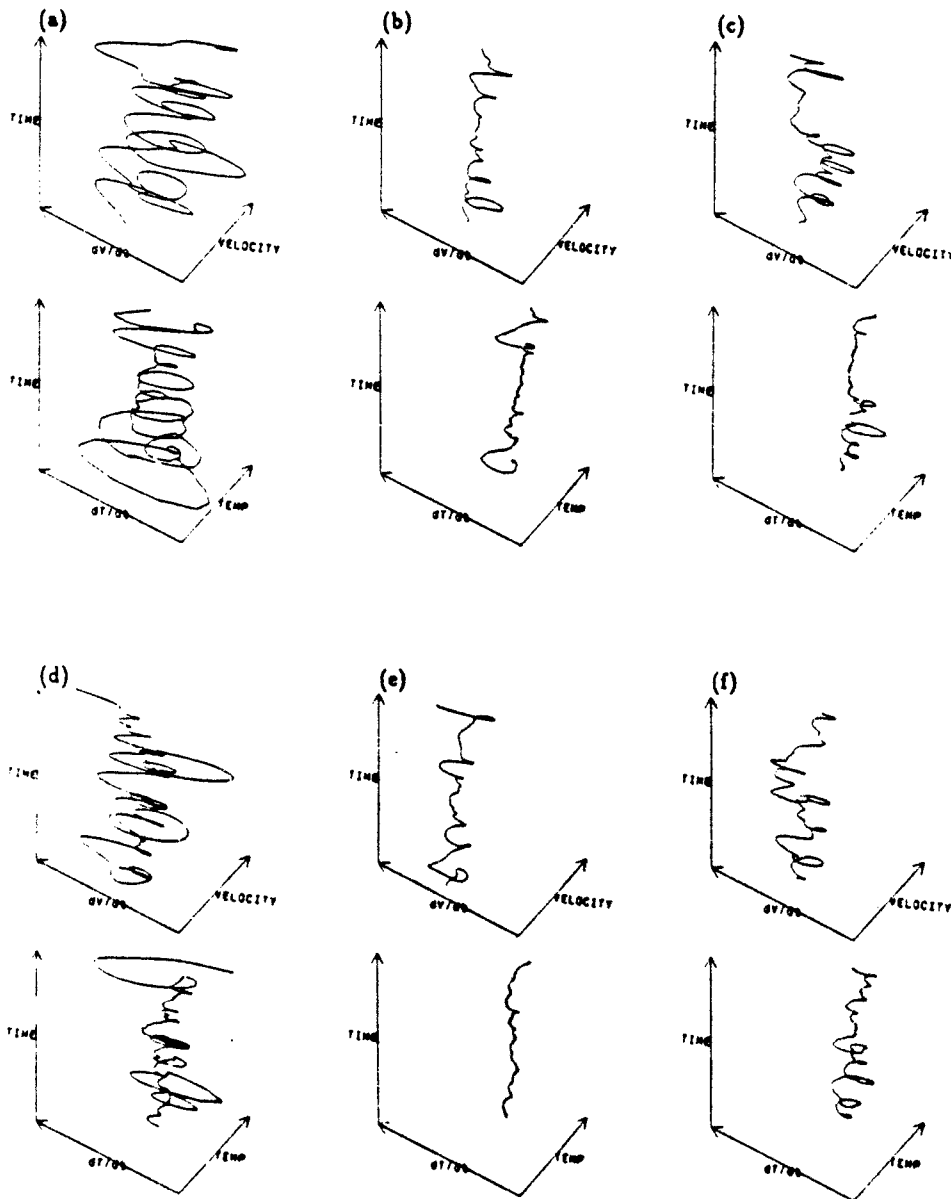


Fig. 2.6 Two-dimensional numerical phase-space plots of velocity and temperature (a) (.50L, .31H) (b) (.70L, .31H) (c) (.90L, .11H) (d) (.50L, .82H) (e) (.70L, .62H) (f) (.90L, .72H)

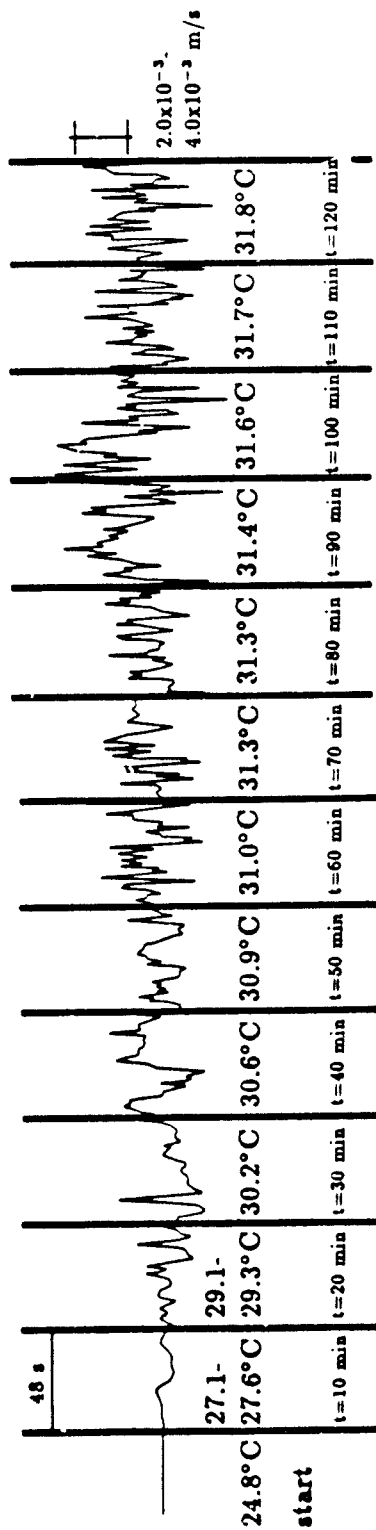


Fig. 2.7 Time-dependent experimental results for velocity at chamber location (.70L, .31H) with increasing heat source temperature

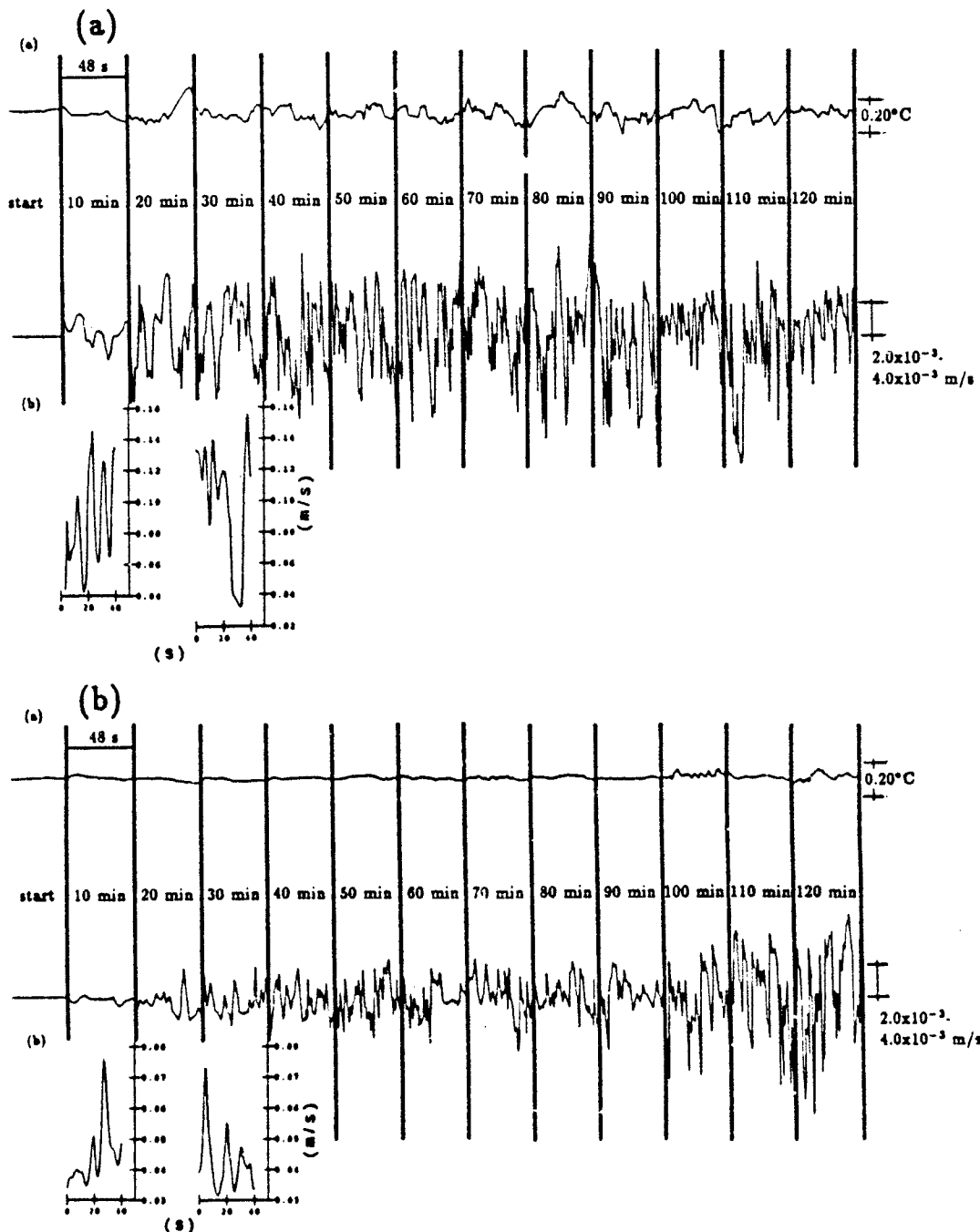


Fig. 2.8 Comparison of the (a) time-dependent experimental results for velocity and temperature (b) time-dependent numerical results for velocity at chamber locations: (a) (.50L, .31H) (b) (.70L, .31H) (c) (.90L, .11H) (d) (.50L, .82H) (e) (.70L, .62H) (f) (.90L, .72H)

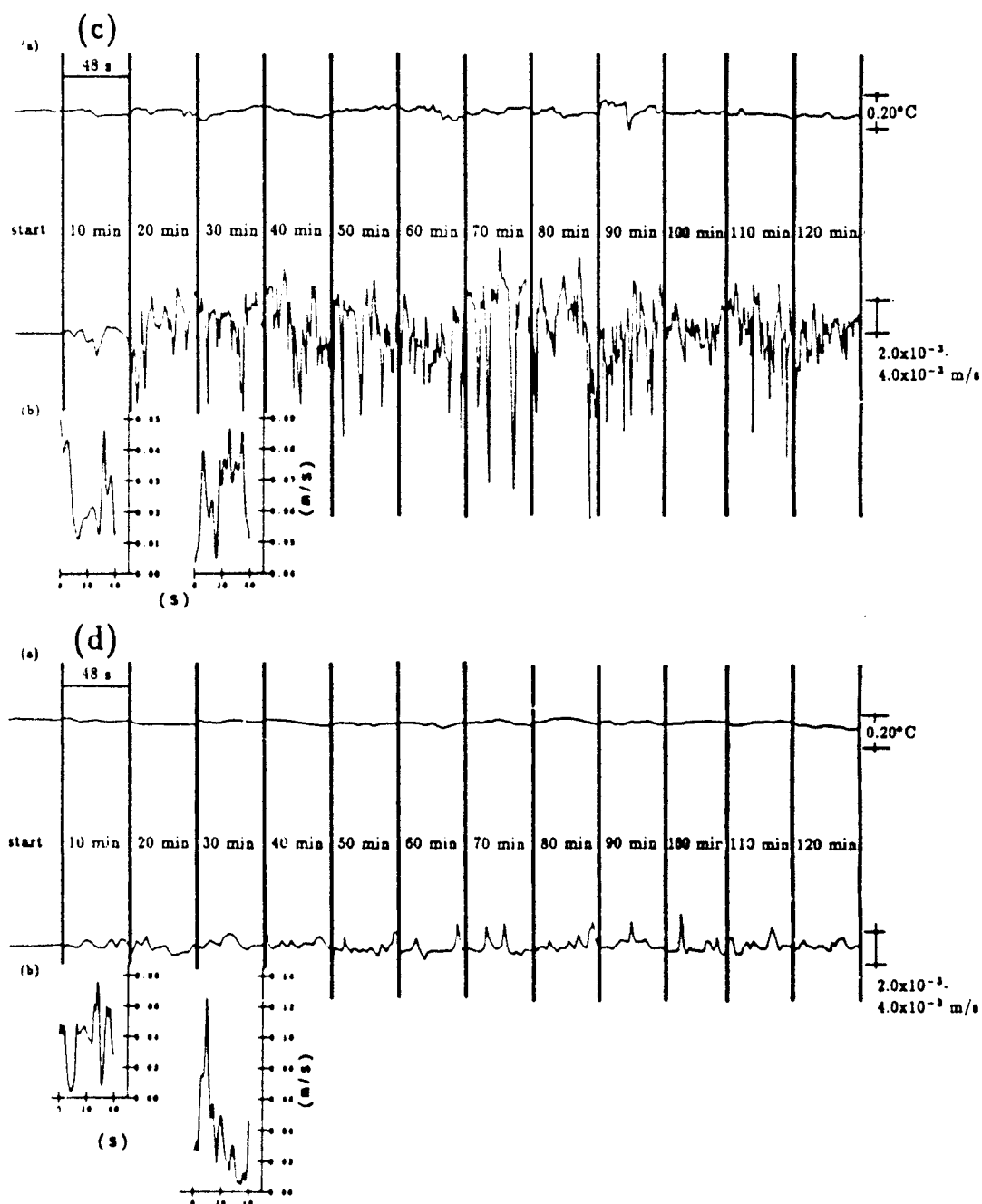


Fig. 2.8 Comparison of the (a) time-dependent experimental results for velocity and temperature (b) time-dependent numerical results for velocity at chamber locations: (a) (.50L, .31H) (b) (.70L, .31H) (c) (.90L, .11H) (d) (.50L, .82H) (e) (.70L, .62H) (f) (.90L, .72H)

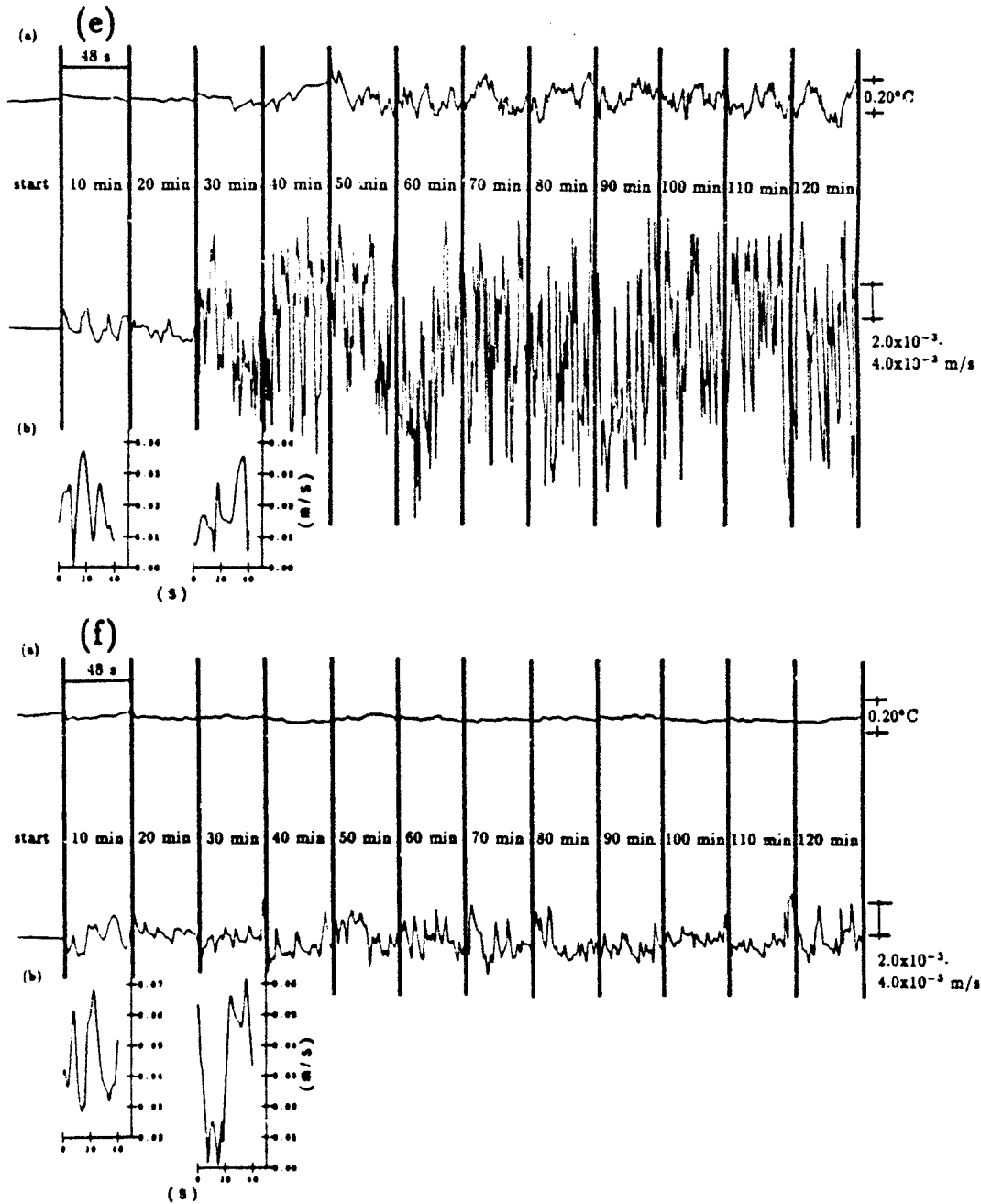


Fig. 2.8 Comparison of the (a) time-dependent experimental results for velocity and temperature (b) time-dependent numerical results for velocity at chamber locations: (a) (.50L, .31H) (b) (.70L, .31H) (c) (.90L, .11H) (d) (.50L, .82H) (e) (.70L, .62H) (f) (.90L, .72H)

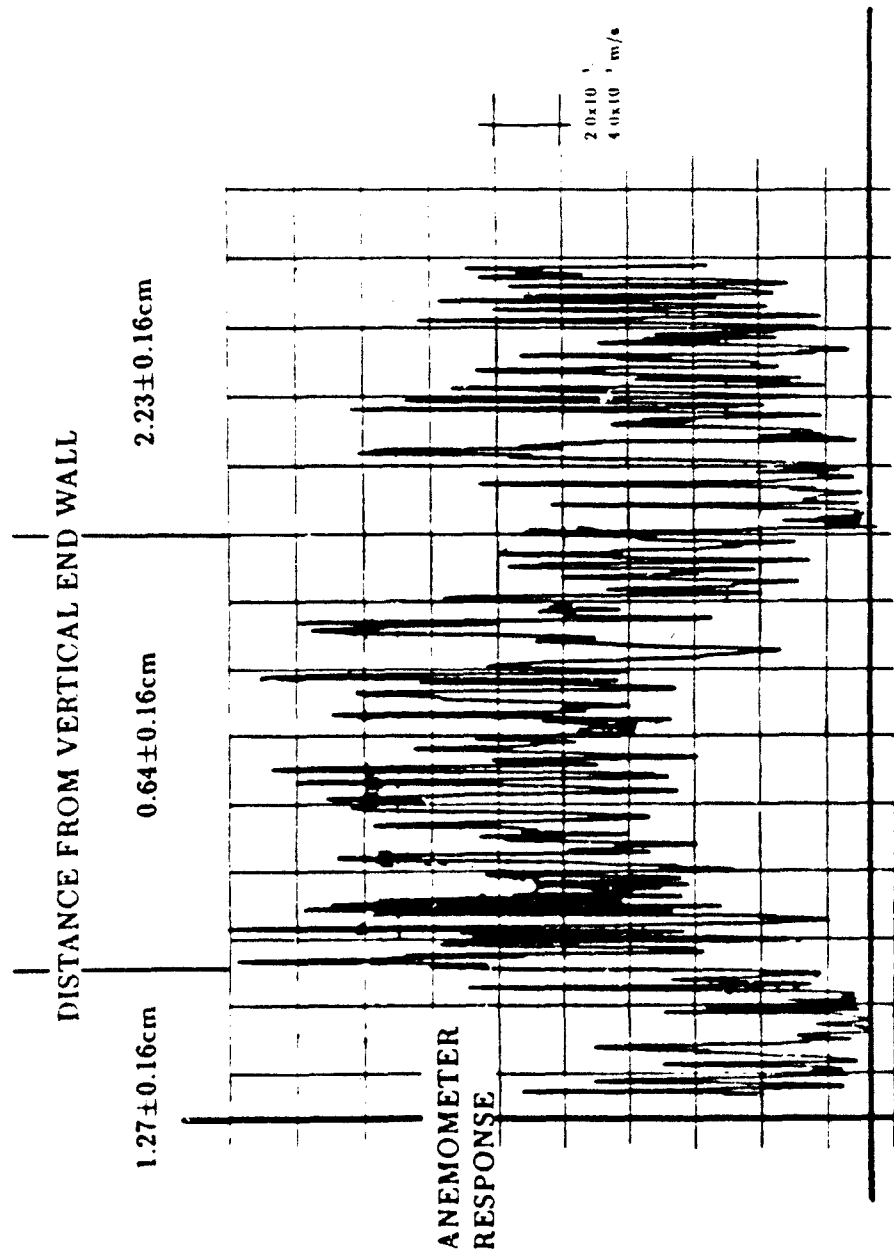


Fig. 2.9 Experimental results for locating the high velocity boundary layer region at  $0.67H$

## Chapter 3

### FLOW VISUALIZATION OF MIXED CONVECTION IN LARGE BAFFLED RECTANGULAR CHAMBERS

#### 3.1 Summary

An investigation to determine the effects of mixed convection on the flow structure of large baffled chambers with and without internal heat sources has been completed. The two-dimensional numerical formulation involved solving the incompressible time-dependent laminar Navier-Stokes equations assuming a Boussinesq fluid with a Prandtl number of 0.7. Flow visualization in the chamber using  $2\mu\text{m}$  Silahydrocarbon aerosol droplets generated from a Collison compressed air nebulizer was used for comparison to the two-dimensional numerical

solutions. Two baffles were placed symmetrically about the vertical axis with and without internal heat sources and asymmetric vertical wall temperatures.

Fluid velocities obtained from flow visualization information using the Silahydrocarbon aerosol droplets with and without internal heat sources in the full-size chamber agreed well with the predicted velocities from the two-dimensional numerical solutions. However, the third dimension did have a significant effect on the development of this flow structure and the effects cannot be discounted as being negligible.

### 3.2 Introduction

Large baffled rectangular chambers with low inlet velocities have traditionally been used to study a variety of chemical atmospheres generated for health effects and biological studies, chemical reaction and chemical species formation studies, and aerosol characterization studies. Generally, they have a cross-sectional diameter greater than .5 meter with an inlet velocity set to maintain 10-15 chamber volume changes per hour. The inlet and exhaust may be mounted vertically or horizontally with an array of internal baffles included for atmosphere dispersion purposes. Additional capabilities include cage units for housing laboratory animals for a variety of biological research applications.



There have been many investigations concerning the Rayleigh-Bénard flow in confined and partially open enclosures with and without baffles or dividers and internal or wall heat sources (Bajorek and Lloyd, 1982; Markatos and Malin, 1982; Powe and Warrington, 1983; Nansteel and Greif, 1981; Sparrow, et al., 1984; Warrington and Powe, 1985; November and Nansteel, 1987; Lee and Goldstein, 1988; Ostrach and Austin, 1988). Such investigations have made use of both experimental and numerical results for information with regard to the temperature profile and flow structure in various closed cavity geometries with differing magnitudes of Grashof, Prandtl, and Rayleigh numbers.

Yang (1988) discusses the buoyant enclosure problem as a dissipative dynamic system whose flow structure development is one of a series of bifurcations brought about by the driving parameters of Rayleigh number, Prandtl number, and enclosure geometry. Development of a flow structure from one that is steady state, periodic in time, aperiodic, and finally chaotic are examples of specific bifurcations that may be expected with variation in Rayleigh number, Prandtl number, and altered geometry. Yang (1988) further discusses the use of an attractor, a concept used in nonlinear dynamics, to describe the temporal asymptotic behavior of a trajectory in the phase space corresponding to a specific bifurcation.

Initial investigations of these chambers incorporated flow visualization techniques using smoke and dyes to optimize the chamber geometry so that well-dispersed atmospheres could be obtained (Carpenter and Beethe, 1981; Moss,

1981). Quantitative approaches to determine the mean residence time of a chamber, the rate of dispersion within a chamber of a tracer gas, and the distribution within a chamber using vapors, droplets, and solid particles have also been done (Hemenway et al., 1982; Beethe et al., 1979; Moss, 1982; Yeh et al., 1986). Most recently, Yerkes et al. (1989) investigated the mixed convection in large baffled rectangular chambers and the characteristic flow structure development for "aided" and "opposed" buoyant forces. Development of the chamber flow structure was found to be predominantly buoyant in nature and sensitive to small variations in the temperature difference between the inlet and wall varying from steady state to asymmetric oscillatory behavior. Continued investigations addressing the effects of mixed convection with internal biological heat sources on the on the transient development of the flow structure were also done by Yerkes et al. (1990). However, the investigations by Yerkes (1990) fail to relate the computational numerical results to the full-size chambers of interest.

A typical chamber used for the purposes described is shown in Fig. 3.1. The chamber consists of a conical inlet intended to uniformly distribute the atmosphere of interest across the inlet plane and an exhaust manifold to achieve uniform flow characteristics across the exhaust plane. Inlet and exhaust flow rates are controlled independently to maintain a slight negative chamber pressure with respect to the ambient pressure (2.5 - 5.1 cm H<sub>2</sub>O). Biological heat sources may consist of a variety of laboratory animal species and are housed in uniformly spaced cage units located directly over the baffles.

The scope of this investigation is shown in Table 3.1 and compares the two-dimensional numerical solutions with a flow visualization technique using Silahydrocarbon aerosol droplets as the visual tracer in the full-size chamber. Of interest is the development of the flow structure with and without internal biological heat sources with asymmetric vertical wall temperatures. The two-dimensional numerical formulation corresponds to a full-size chamber with a depth of one meter. Only the upper baffles and heat sources were considered for this investigation.

Biological heat sources were treated as a constant temperature surface at 32°C and of a size and mass that would be appropriate for a 200 gm to 300 gm rat in a confined enclosure (Mauderly, 1986). It was assumed that physiological control of the body temperature is sufficient to maintain a constant body temperature in the low air velocities within the confines of the chamber.

### 3.3 Analysis

#### Math Formulation

Two-dimensional numerical solutions of the incompressible time-dependent laminar Navier-Stokes equations were calculated in accordance with the two-dimensional problems shown in Fig. 3.2a and 3.2b for cases #1 and #2 respectively. Only the upper baffles with and without heat sources were considered for

numerical formulation. The boundary conditions for temperature on the right and left vertical walls were assumed to be constant and were obtained from the experimental conditions. For this investigation, only the dimensional form of the governing equations were solved, thereby circumventing the immediate need for scaling considerations of the non-dimensional parameters as is typically required for buoyant flow conditions (Ostrach and Austin, 1988). The Boussinesq approximation was used in the vertical direction to account for buoyancy effects. Using this approximation the vertical body force becomes:

$$\vec{B}_z = \rho \vec{g} [1 - \beta (T - T_{IN})]$$

where:

$$\beta = \frac{1}{T_{IN}}$$

for an ideal gas.

For this investigation, the reference values for all of the gas properties were taken to be those at the inlet plane.

The chamber inlet cone was assumed to provide a uniform velocity distribution across the inlet plane with the exhaust manifold providing a velocity distribution resulting from a constant exhaust pressure across the outlet plane. Viscous dissipation and pressure work were assumed to be negligible due to the low buoyancy-induced velocities. With these assumptions, the two-dimensional governing equations become:

Conservation of mass:

$$\frac{\partial v}{\partial y} + \frac{\partial w}{\partial z} = 0 \quad (3.1)$$

Conservation of momentum:

$$\rho \left( \frac{\partial v}{\partial t} + v \frac{\partial v}{\partial y} + w \frac{\partial v}{\partial z} \right) = - \frac{\partial p^+}{\partial y} + \mu \left( \frac{\partial^2 v}{\partial y^2} + \frac{\partial^2 v}{\partial z^2} \right) \quad (3.2)$$

$$\begin{aligned} \rho \left( \frac{\partial w}{\partial t} + v \frac{\partial w}{\partial y} + w \frac{\partial w}{\partial z} \right) = & - \frac{\partial p^+}{\partial z} + \mu \left( \frac{\partial^2 w}{\partial y^2} + \frac{\partial^2 w}{\partial z^2} \right) \\ & + \rho g \beta (T - T_{IN}) \end{aligned} \quad (3.3)$$

Conservation of energy:

$$\rho \left( \frac{\partial T}{\partial t} + v \frac{\partial T}{\partial y} + w \frac{\partial T}{\partial z} \right) = \frac{k}{C_p} \left( \frac{\partial^2 T}{\partial y^2} + \frac{\partial^2 T}{\partial z^2} \right) \quad (3.4)$$

The boundary conditions were specified with the assumption that there is a uniform inlet velocity profile and the vertical end wall temperature is constant. Only the magnitude of the inlet velocity is specified. The magnitude of the outlet velocity is such as to satisfy the conservation of mass with a constant reference pressure across the outlet plane.

The outlet boundary condition for temperature was considered to be locally parabolic such that the Peclet number is sufficiently large so as to exhibit local one-way behavior in the axial direction. The baffles were treated as being

infinitesimally thick with a no-slip boundary condition. The baffle temperature was specified to be that of the local fluid temperature.

Boundary conditions:

Inlet:  $v = 0$ ,  $w = W_{IN}$ ,  $T = T_{IN}$

Right wall:  $v = 0$ ,  $w = 0$ ,  $T = T_{rwall}$

Left wall:  $v = 0$ ,  $w = 0$ ,  $T = T_{lwall}$

Baffle:  $v = 0$ ,  $w = 0$

Heat sources:  $v = 0$ ,  $w = 0$ ,  $T = 32^{\circ}\text{C}$

Outlet:  $v = 0$ ,  $p^+ = 0$

## Aerosol Science

For effective use of flow visualization using Silahydrocarbon aerosol droplets one must consider some basic aerosol science to determine terminal settling velocities and the effects of thermophoresis induced velocities for the droplets generated, (Hinds, 1982). Droplet behavior in the flow field will not necessarily give correct information as to the magnitude of the fluid velocity due to the external forces acting on the aerosol droplets resulting in droplet motion deviating from

that of the fluid flow field. Figure 3.3 shows the free body diagram of a droplet that is suspended in the flow stream. The vertical forces consist of the droplet weight, buoyant force, and drag force in which:

$$\sum F = 0 = -mg + [\text{buoyant force}] + [\text{drag force}] \quad (3.5)$$

where

$$m = \rho_d V_d$$

$$[\text{buoyant force}] = \rho_f V_d g$$

$$[\text{drag force}] = 3\pi\mu V d$$

The drag force assumes Stokes law where the drag coefficient,  $C_D = 24/\text{Re}$ . However, Stokes law assumes that the relative velocity of the fluid at the surface of the droplet is zero. For droplets less than  $1\mu\text{m}$  in diameter, the drag force will also include a slip correction factor,  $C_c$ , (Cunningham slip correction factor) accounting for the "slip" of a droplet as the diameter approaches the mean free path of the fluid molecules. Now, the drag force becomes:

$$[\text{drag force}] = \frac{3\pi\mu V d}{C_c}$$

where

$$C_c = 1 + \frac{2.52\lambda}{d} \quad (3.6)$$

for droplet diameters down to  $0.1\mu\text{m}$ .

The velocity magnitude of the fluid to maintain the droplet in a stationary position may now be calculated. This velocity is the terminal settling velocity of a spherical droplet of a given density and diameter where:

$$V = \frac{1}{18} \frac{d^2 g C_c}{\mu} (\rho_d - \rho_f) \quad (3.7)$$

Thermophoresis induced velocity must also be considered. This is the velocity induced by forces resulting in the difference in molecular bombardment on opposite sides of the droplet due to a temperature gradient in the flow field. The magnitude of thermophoretic velocity depends on gas and droplet properties and on the temperature gradient. This velocity may be approximated by the following relation where the droplet diameter is greater than the mean free path ( $d > \lambda$ ):

$$\bar{V}_{th} = \frac{-3\mu C_c H \nabla T}{2\rho_f T_d} \quad (3.8)$$

where

$$H \simeq \left( \frac{1}{1 + 6\lambda/d} \right) \left( \frac{k_f/k_d + 4.4\lambda/d}{1 + 2k_f/k_d + 8.8\lambda/d} \right) \quad (3.9)$$

Motion of the aerosol droplets may now be used and compared to the fluid motion. For instance, if a droplet has no vertical motion, the fluid velocity must be that of the terminal droplet velocity and conversely, if a droplet is settling at



the terminal velocity there is no vertical fluid velocity. Also, in regions of high temperature gradients such as at the vertical wall, the lateral velocity component of the droplet toward the wall will be in part due to the thermophoretic induced velocity and in part due to droplet diffusion.

### 3.4 Numerical Scheme

The numerical scheme used is a finite-difference iterative method of solution using a control-volume approach as developed by Spalding et al. (1980). A two-dimensional numerical model was formulated using the fully implicit finite-difference scheme of the time dependent, laminar Navier-Stokes equations. The "SIMPLEST" (Spalding et al., 1980) method of solution for the momentum equations was used with the hybrid differencing formulation. When a cell Peclet number is within the range -2 to 2, a central-difference scheme is used and when the cell Peclet number is outside this range the upwind differencing scheme is used.

The outlet boundary condition for temperature was considered to be locally parabolic such that the Peclet number is sufficiently large so as to exhibit local one-way behavior in the axial direction (Patankar, 1980). This approach to specifying the outlet boundary condition for a dependent variable is generally accepted as the most available approach for internal flow problems in which

the fluid leaves the calculation domain and the dependent variable of interest is unknown.

The baffles were treated as being infinitesimally thick with a no-slip boundary condition by setting the cell wall velocity to zero over the region of the baffle location. The baffle temperature was specified to be that of the local fluid temperature. Heat sources were "blocked" by setting the cell velocity components within the heat source region to zero and fixing to a constant temperature.

The solution sequence involved solving for the velocity and temperature fields from an assumed pressure field at a specific time step. The pressure field was then subsequently updated using these velocity and temperature fields in the pressure-correction equation such that the conservation of mass was satisfied. This iterative sweep process was then repeated using a slab-by-slab method at each time step until convergence criteria were satisfied. Convergence characteristics at each time step were maintained by reducing the time step where appropriate with the minimum computational time required to reach a steady state solution being at least three characteristic times,  $H/W_{IN}$ , or approximately ten minutes. In addition, conditions for convergence to a solution, either at a specific time step or to a steady state solution, was based upon a dependent variable,  $\phi$ , varying less than a predetermined change of the magnitude fraction,  $\epsilon_\phi$ , between successive sweeps or time steps where:

$$|\phi_s - \phi_{s+1}| / \phi \leq \epsilon_\phi$$

The values of  $\epsilon_\phi$  were varied and it was required that the magnitude of the dependent variable be greater than the roundoff error or truncation error such as would happen when velocities approach zero. Typically, for a steady state solution,  $\epsilon_\phi$  ranged from  $1.0 \times 10^{-3}$  to  $1.0 \times 10^{-2}$  over a time span of 25 seconds, while over five successive sweeps  $\epsilon_\phi$  was less than  $1.0 \times 10^{-3}$ . Intermediate results were monitored to insure convergence and numerical stability at a specific time step during the course of the solution. These intermediate results were also used to determine convergence toward either a steady state or a steady periodic solution.

Appropriate grid size and spacing were chosen to give acceptable numerical accuracy while still maintaining reasonable and acceptable computational times. Due to the complexity of the flow structure, the errors as a result of grid size were determined first, by comparing the shape of the flow structure for similarity with a previous solution at a larger grid size. Secondly, random locations throughout the chamber were selected and the average error compared between the similar solutions such that decreasing the grid size by ten percent resulted in less than a one percent error in the dependent variable. For this problem, a uniform  $100 \times 100$  grid was chosen to give good coverage.

### 3.5 Experimental Approach

Figure 3.1 shows the full-size whole-body inhalation exposure chamber as is used in the toxicity testing of various chemical compounds. The rectangular chamber body measures  $0.813\text{ m} \times 0.813\text{ m} \times 0.686\text{ m}$  and is constructed of stainless steel with the front and sides fabricated of glass for observation during chamber operation. The inlet consists of a annulus and conical section for the purpose of obtaining a uniform velocity distribution across the inlet plane. The exhaust consists of a radial spider also for the purpose of obtaining uniform exhaust characteristics across the exhaust plane.

Figure 3.4 shows the schematic of the aerosol generation apparatus that was used to generate a Silahydrocarbon aerosol droplet for the purposes of visualizing the chamber flow structure. The generation apparatus consisted of a six-hole Collison (BGI, Inc. Waltham, MA.) compressed air nebulizer operated at 20 psi to produce a mass median droplet diameter of  $2.0\mu\text{m}$  with a geometric standard deviation of 2.0. The droplet density was assumed to be that of the bulk fluid density of Silahydrocarbon,  $\rho_d = .8145\text{ gm/cc}$ , resulting in a terminal droplet velocity of  $9.85 \times 10^{-3}\text{ cm/s}$ . The thermophoretic velocity for a  $1.0\mu\text{m}$  droplet is on the order of  $1.0 \times 10^{-4}\text{ cm/s}$  for a one degree temperature per centimeter gradient.

Chamber inlet and wall temperatures were obtained using iron-constantan surface mounted thermocouples placed along the centerline of the vertical end walls at  $.15H$  and  $.70H$ . These thermocouples were calibrated to within  $\pm 0.1^\circ\text{C}$  using a constant temperature stirred water bath and an NBS traceable thermometer  $\pm 0.05^\circ\text{C}$ . The vertical wall temperatures were averaged to give the temperature boundary condition that was subsequently used in the two-dimensional numerical formulation.

Flow visualization was obtained using an 8 mm video camera (Sony CCD-V9) with lighting provided by insulated florescent lamps placed at the top and base of the right vertical end wall. The fluid velocity in the plane of the camera was calculated by observation of the aerosol path with known distance references in the chamber. Effects of the lamps were determined prior to the experimental procedure by visual observation using low level lighting and found to be negligible. The experimental procedure consisted of introducing a 30 second bolus of Silahydrocarbon droplet aerosol while maintaining the volumetric flow rate through the chamber to produce an inlet velocity of  $0.71 \times 10^{-3} \text{ m/s}$ .

### 3.6 Results and Discussion

Experimental flow visualization information was obtained for cases #1 and #2 with the right and left vertical end wall temperatures incorporated as boundary conditions for the subsequent corresponding numerical formulations and so-

lutions for the cases investigated, Table 3.1. Figures 3.5 and 3.6 show the two-dimensional numerical results for the velocity direction and magnitude profiles for cases #1 and #2 respectively.

Also shown in Figs. 3.5 and 3.6 are the chamber locations for which the velocity obtained from the visualization experiments are compared to the numerical results. The chamber locations for the velocity comparison in case #1 were taken at the lower vertical surface at the left wall, A, the right lower horizontal plane just above the exhaust manifold, B, and the lower vertical surface at the right wall, C. The chamber location for the velocity comparison in case #2 were taken at the location between the two baffles and heat sources along the chamber centerline, A, and the right lower horizontal plane just above the exhaust manifold, B. Case #2 also showed a separation point located at the lower right vertical wall, C. The vertical location of this separation point is compared for both the numerical results and measurements made from the flow visualization information.

A summary of the two-dimensional numerical results compared with the experimental flow visualization are shown in Table 3.2. The numerical solutions showed steady state behavior for the two cases studied. There was good agreement between the numerical and experimental results for the chamber locations investigated. In general, even though the full-size chamber geometry differs from that of the numerical formulation, the visual observations indicated numerous similarities in the development of the flow structure.

Case #1 experimental observations showed a rotational mass flux about the perimeter of the chamber as did the numerical solution. There was little vertical motion in the central lower region beneath the baffles. Comparison of the numerically obtained vertical velocities in this lower region indicated the velocity magnitude to be approximately that of the droplet settling velocity. The vertical velocity gradually increased in magnitude as the right vertical end wall was approached.

Bénard cells were observed for case #2 above the upper baffles and heat sources while the lower region below the baffles showed stagnate layers of aerosol droplets. Numerically obtained vertical velocities in this lower region also showed the velocity to be on the order of the droplet settling velocity. Separation of the flow from the lower right vertical end wall was due to a mass flowing down the right vertical end wall intersecting with mass flowing across the exhaust plane and up the same vertical end wall. The intersection location resulted in the observed separation of the mass from the vertical wall. The bulk of the aerosol mass remained in the upper region showing a significant increase in residence time directly influenced by the heat sources. An apparent distinguishing feature of this case is the lack of flow between the baffles along the chamber centerline. The absence of any vertical mass transport in this region was confirmed by both numerical and the experimental visualization information.

The flow structure for case #1 appeared to be sensitive to external temperature influences as was indicated when a heat gun was used to heat the third

dimension front vertical surface. The flow structure for case #2 did not appear to be as sensitive to similar external temperature influences.

### 3.7 Conclusion

The two-dimensional numerical solutions agreed well with the visual studies that were conducted for the cases with and without internal heat sources and asymmetric vertical end wall temperatures. There were significant third dimensional effects that need to be considered for future studies, however, the two-dimensional solutions gave accurate information with regard to the general form of the flow structure. Characteristic elements of the flow structures for both cases were shown to be present in the numerical solutions as well as the experimental observations for the chamber locations investigated. Differences in the chamber geometry and the numerical formulation for the most part did not appear to greatly effect the results except for the inlet cone region where the flow was shown to follow the inlet cone surface. The effects of internal heat sources were consistent and showed a significant deviation in the flow structure from one without the internal heat sources. This deviation in the flow structure appeared to result not only in the development of Bénard cells but also resulting in the noticeable increase in mass residence time in the upper region above the baffles and heat sources. For both cases mass was transported along the chamber walls verifying the existence of a high velocity boundary layer.



Table 3.1  
EXPERIMENTAL CONDITIONS FOR  
2-D NUMERICAL COMPARISON

| case #           | Temperature specification        |
|------------------|----------------------------------|
| 1                | $T_{IN}=21.5^{\circ}\text{C}$    |
| W/O HEAT SOURCES | $T_{rwall}=22.4^{\circ}\text{C}$ |
|                  | $T_{lwall}=21.2^{\circ}\text{C}$ |
| 2                | $T_{IN}=24.0^{\circ}\text{C}$    |
| W HEAT SOURCES   | $T_{rwall}=23.0^{\circ}\text{C}$ |
|                  | $T_{lwall}=22.0^{\circ}\text{C}$ |

(upper baffles and heat sources)

$$W_{IN} = 0.71 \times 10^{-3} \text{m/s}$$

Table 3.2  
EXPERIMENTAL FLOW VISUALIZATION  
AND 2-D NUMERICAL COMPARISON

| case #                | Location | Numerical  | Experimental  |
|-----------------------|----------|--|---------------|
| 1<br>W/O HEAT SOURCES | A        | 2-5 cm/s↓  | 2-3 cm/s↓     |
|                       | B        | 1-3 cm/s⇒<br>$4.5 \times 10^{-3} - 2.0 \times 10^{-1}$ cm/s↑     | 4-5 cm/s⇒     |
|                       | C        | 1-3 cm/s↑  | 1.0-1.5 cm/s↑ |
| 2<br>W HEAT SOURCES   | A        | 9.2 cm/s⇒ (max)  | 10-12 cm/s⇒   |
|                       | B        | 1.5-3.0 cm/s⇒<br>$5.0 \times 10^{-3} - 2.5 \times 10^{-2}$ cm/s↑ | 1-2 cm/s⇒     |
|                       | C        | 8.2-9.6 cm‡  | 5-10 cm‡      |

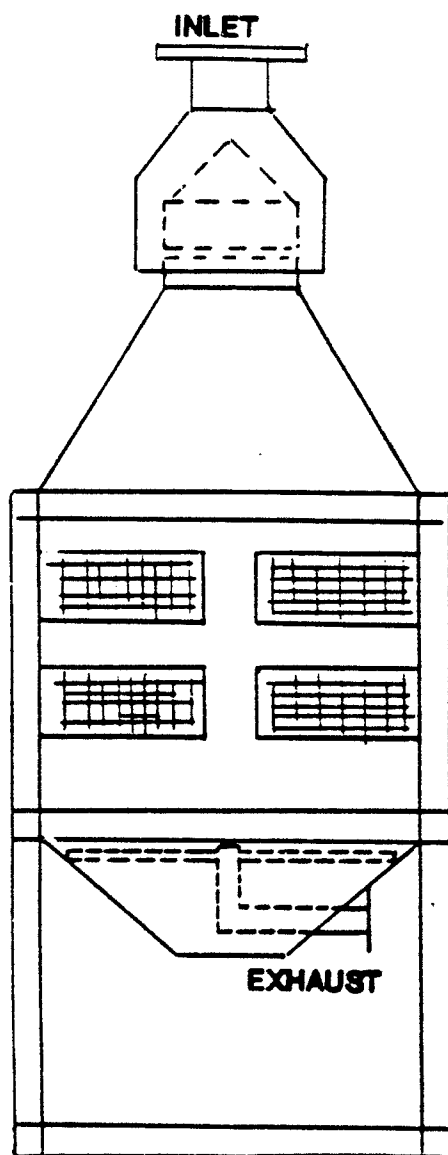


Fig. 3.1 Whole-body inhalation exposure chamber

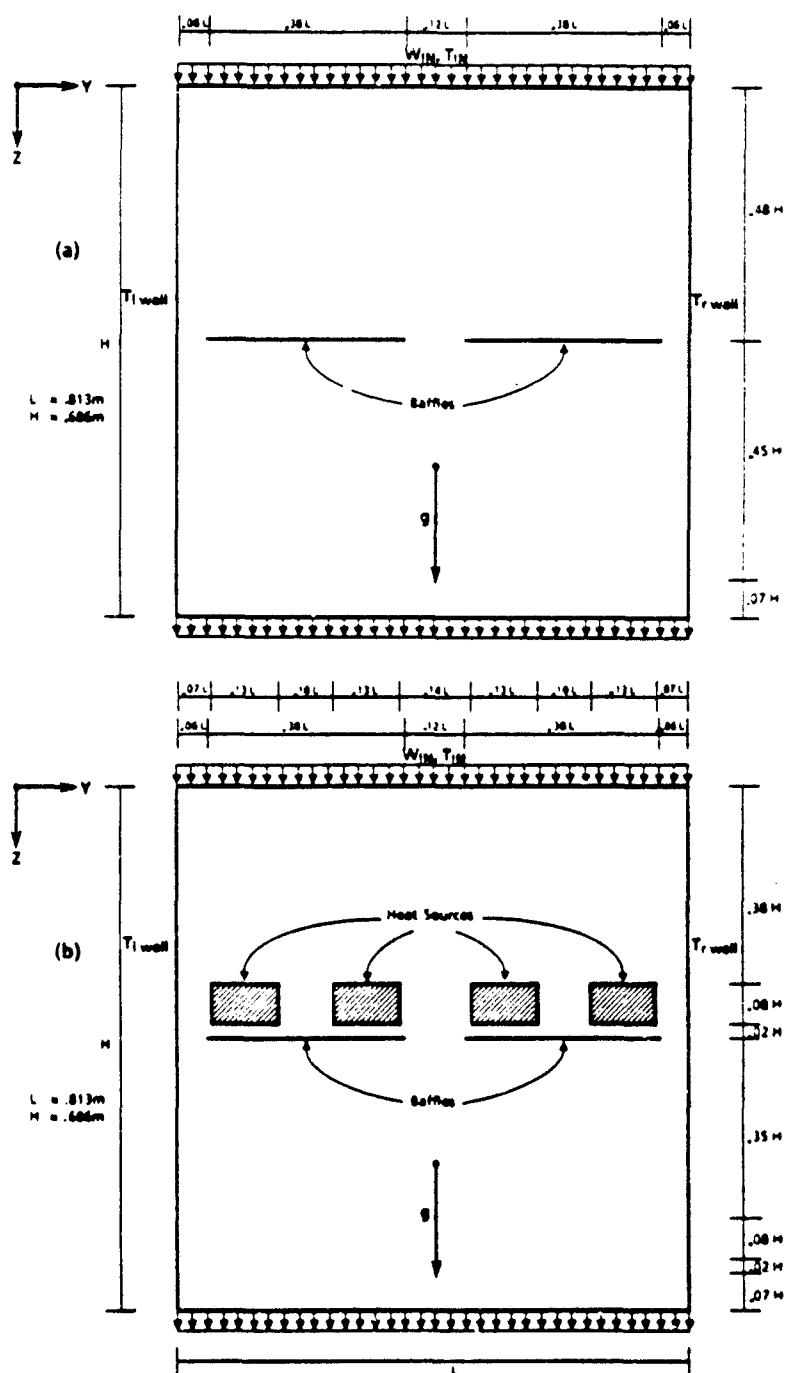


Fig. 3.2 Chamber geometry specification for two-dimensional numerical formulation (a) case #1 (b) case #2

**[DRAG + BUOYANCY]**



**[WEIGHT]**

Fig. 3.3 Forces on aerosol droplet

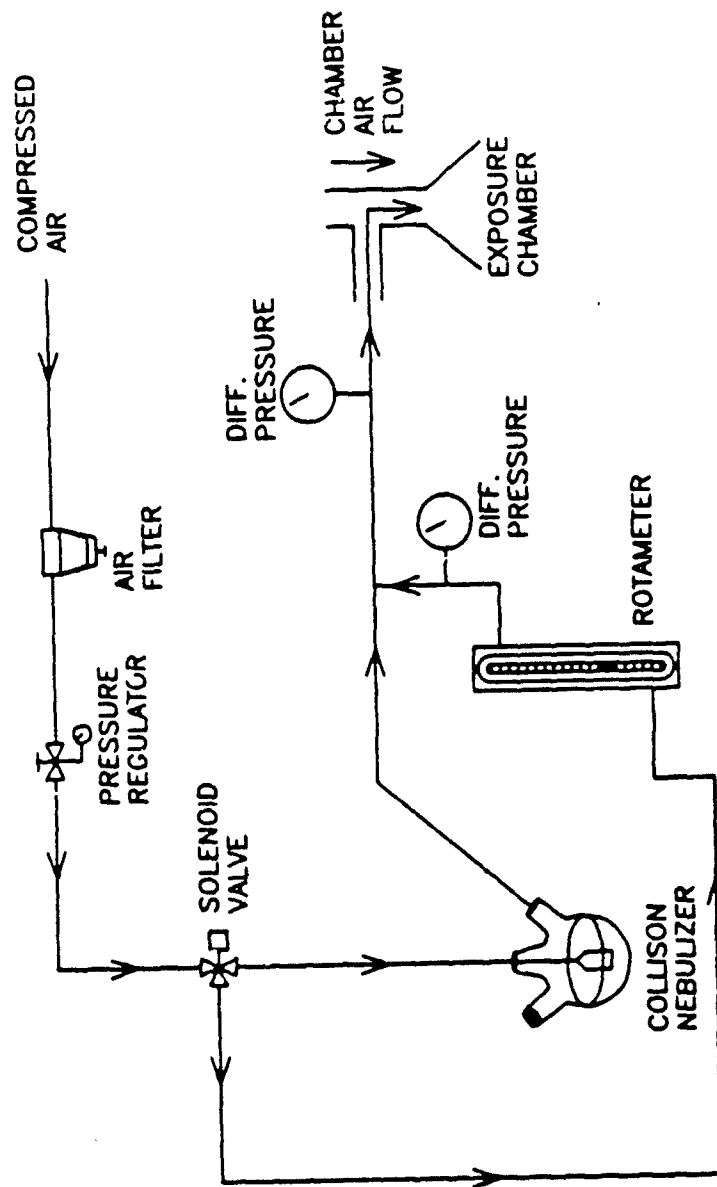


Fig. 3.4 Silahydrocarbon droplet aerosol generation system

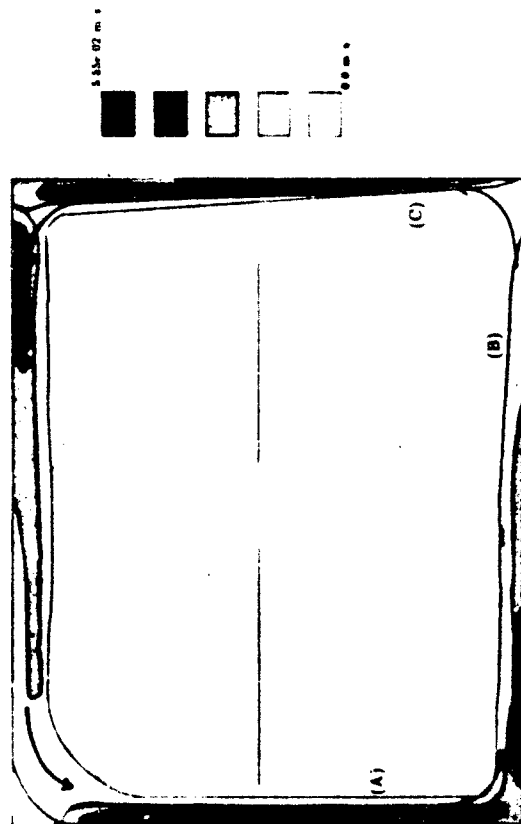


Fig. 3.5 Case #1 two-dimensional numerical results showing velocity direction and magnitude and chamber locations for comparison of flow visualization experimental results

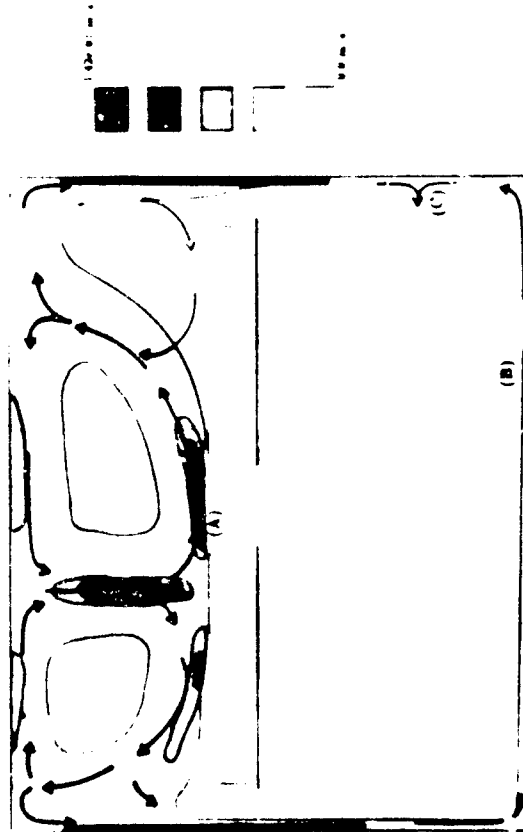


Fig. 3.6 Case #2 two-dimensional numerical results showing velocity direction and magnitude and chamber locations for comparison of flow visualization experimental results



## OVERALL SUMMARY

### *Conclusions*

Development of the chamber flow structure with and without internal heat sources was shown to be predominately buoyant in nature with the velocity profile developing primarily due to temperature differences within the confines of the chamber. The chamber flow structure without internal heat sources was found to be sensitive to small variations in the temperature difference between the inlet and vertical wall with an increase in the mass flux to the vertical wall for inlet temperatures greater than the vertical wall temperatures. As the inlet to vertical wall temperatures increased, there was shown to be an increasing low velocity region depicted by the stratified temperature gradient for which mass and energy is transported by diffusion as opposed to convection. When inlet temperatures became less than the vertical wall temperature and without internal heat sources, the flow structure became oscillatory in nature primarily due to the placement of the lower baffles. This oscillatory flow structure consisted of a central core of cooler fluid falling and subsequently rising along the warmer vertical walls. With the addition of internal heat sources, the flow structure developed multiple Bénard cells typically common to buoyant flow structures. Development of the flow structure was shown to be marginally stable with self-sustained oscillatory

behavior as the Bénard cells formed and subsequently collapsed. The flow structure developed through a series of bifurcations from steady-state to periodic, aperiodic, and chaotic with increasing temperature differences between the heat sources, inlet, and vertical walls.

Experimental efforts using both the experimental laboratory model and the larger, full-size chamber provided useful information in comparing the experimental results to the numerical solutions. Use of the laboratory experimental model to depict the larger, full-size chamber showed significant three-dimensional effects influencing the development of the flow structure within the model. However, even with these differences, formulation of a three-dimensional numerical approach successfully addressed these inconsistencies. Flow visualization in the larger, full-size chamber agreed well with the two-dimensional numerical formulation. The fluid velocity as determined at the selected chamber locations agreed well with the numerical results as did the location of the separation point when the internal heat sources were considered. There still appeared to be significant third-dimensional effects in the full-size chamber.

The two-dimensional formulation for either the laboratory model or larger, full-size chamber appeared to be limited due to the neglecting of the third-dimension. However, the two dimensional results did predict the general chamber behavior as shown by the visualization experiments in the full-size chamber. The assumption of constant and uniform wall temperatures, heat source temperatures, and inlet velocity appeared to be appropriate for these initial investigations as was also indicated by the visualization experiment.

### *Recommendations*

With these initial studies concluded, it is appropriate to back track and initiate detailed parametric studies to determine the effects of temperature, baffle placement or altered geometry, and heat source placement. Coinciding with these parametric studies, evaluation of the multiple length scales for future investigations would be helpful in addressing the order of magnitude effects of various non-dimensional terms at various chamber locations in addition to deriving the non-dimensional and normalized sets of governing equations.

These chambers are normally operated with multiple chemical species, multiple phase atmospheres with and without condensation, chemical reactions, etc. Therefore additional efforts in investigating the transport characteristics of a variety of airborne compounds is of interest in further developing and describing the physics of chamber performance under specific applications.

Although the computational time for the solution of these problems has been extensive, an expanded formulation to one that incorporates the effects of three-dimensions is desirable. These formulations would more accurately depict chamber behavior defining criteria such as inlet and exhaust configurations for future chamber design and modification.

## Appendix A: BUOYANT FLOW AND EXPOSURE CHAMBER OVERVIEW

### A) BUOYANT FLOW OVERVIEW

These investigations involve the development of a velocity field within a fluid primarily due to changes in the fluid density as a result of temperature gradients. It is appropriate to discuss some basic theory behind the development of this type of fluid motion to further supplement the investigations presented herein.

It may be recalled that mass and energy is transported either by convection (velocity) or diffusion (random molecular motion). Convection transport can be induced by either external means such as fluid machinery or natural means such as gravitational, centrifugal, or coriolis forces. Motion is induced when the lighter less dense fluid rises and the heavier greater density fluid falls.

There have been numerous investigations into the development of Rayleigh-Bénard flow within confined enclosures. However there is little information concerning the addition of low velocity fluid flow into these same enclosures. Figure A.1 shows the scope of previous investigations for free, forced, and mixed convection regimes for flow in vertical tubes, (Aung, 1987). There has been very little work with low Reynolds number and high Rayleigh number flows in cavities whose diameter to height ratio approach one. For the investigations conducted herein, inlet Reynolds numbers range from 32 to 235 with Rayleigh numbers on the order of  $10^7$ . Although the chamber of interest is of a rectangular cross-section rather than a circular cross-section, the hydraulic diameter to chamber

height ranged from 0.18 to 1.31 for the experimental laboratory model and full-size chamber respectively. The scope of this investigation therefore encompasses the free convection, laminar flow regime for which there has been very little investigative research efforts.

The general form of the time-dependent differential governing equations for a compressible variable property fluid are as follows:

Conservation of mass:

$$\frac{\partial \rho}{\partial t} + \nabla \cdot (\rho \vec{V}) = 0 \quad (A.1)$$

Conservation of momentum:

$$\rho \frac{D\vec{V}}{Dt} = \nabla \cdot \tau - \nabla p + \rho \vec{B} \quad (A.2)$$

Conservation of energy:

$$\rho C_p \frac{DT}{Dt} = \nabla \cdot \vec{q}_e + S \quad (A.3)$$

where  $D/Dt$  is the substantial derivative  $(\partial/\partial t + \vec{V} \cdot \nabla)$ . The energy equation (A.3) does not contain the viscous dissipation and pressure work terms, since both are small due to the low velocities encountered in natural convection phenomena (Gebhart, 1971).

For these investigations, the fluid property variation was accounted for by assuming the fluid to be a Boussinesq fluid. This approximation relates the fluid density in the body force term to a reference fluid density by way of the fluid expansion coefficient,  $\beta$ , and difference between the fluid temperature and a reference fluid temperature (Yang, 1987; Gebhart, 1971). By Bernoulli's equation, the local depression of pressure in the flow region at any given vertical distance,  $z$ , is not greater than  $\rho w^2/2$  or

$$p_o - p \leq O[gz(\rho_o - \rho)]$$

Using this relation and since  $\rho = \rho(p, t)$ , the differences in density at a given  $z$  may be written as a double expansion in terms of the temperature difference and pressure difference where:

$$\rho_o - \rho = \left( \frac{\partial \rho}{\partial T} \right)_p (T_o - T) + \dots + \left( \frac{\partial \rho}{\partial p} \right)_T (p_o - p) + \dots + \frac{\partial^2 \rho}{\partial T \partial p} (T_o - T)(p_o - p) + \dots$$

Using the estimate for  $p_o - p$ , the density difference for an ideal gas ( $p = \rho RT$ ), in terms of  $(T - T_o)$  becomes

$$\rho_o - \rho = \frac{\rho \beta (T - T_o)}{1 + \beta (T - T_o)} + \frac{g \beta z}{R} (\rho_o - \rho) + \frac{g \beta z}{R} \beta (T - T_o) (\rho_o - \rho)$$

+additional cross terms

where

$$\beta = -\frac{1}{\rho} \left( \frac{\partial \rho}{\partial T} \right)$$

for an ideal gas

$$\beta = \frac{1}{T_0}$$

The quantity  $g\beta z/R$  is very small for gases at the terrestrial intensity of gravity and  $(T - T_0)/T$  is generally assumed to be small. Now, the following approximation for density becomes

$$\rho = \rho_0[1 - \beta(T - T_0)] \quad (A.4)$$

Using this approximation for the variation of density in the body force term of the momentum equations, the formulation becomes one in terms of the difference between the fluid temperature and a reference fluid temperature. Allowing all the remaining density terms in the governing equations to be the constant reference fluid density,  $\rho = \rho_0$ , the governing equations can now be formulated in the incompressible form. As with any approximation, there are limits for which a Boussinesq fluid may be assumed as discussed by Zhong (1985). This approximation is generally valid for  $\theta_0 \leq 0.1$  with an overprediction of the vertical velocity as much as 20 percent as  $\theta_0$  approaches 0.2. For this investigation, the maximum value of  $\theta_0$  is .027 which is well within the limits of acceptable use for assuming a Boussinesq fluid.

Using this approximation in the vertical direction to account for buoyancy effects, the vertical body force becomes:

$$\vec{B}_z = \rho \vec{g} = \rho_0 \vec{g}[1 - \beta(T - T_0)] \quad (A.5)$$

The  $\rho_0 g$  term in the Boussinesq approximation, equation (A.2), may now be transformed into a hydrostatic pressure term and be combined with the existing static pressure term in the momentum equation while noting the gravitational direction to maintain the correct sign in the body force term. For these investigations, the reference values for all of the gas properties were taken to be those at the inlet plane. Viscous dissipation and pressure work were assumed to be negligible due to the low buoyancy-induced velocities. With these assumptions, the time-dependent incompressible governing equations become:

Conservation of mass:

$$\nabla \cdot (\vec{V}) = 0 \quad (A.6)$$

Conservation of momentum:

$x$ -direction:

$$\rho \left( \frac{\partial u}{\partial t} + \nabla \cdot (\vec{V}u) \right) = -\frac{\partial p^+}{\partial x} + \nabla \cdot (\mu \nabla u) \quad (A.7)$$

$y$ -direction:

$$\rho \left( \frac{\partial v}{\partial t} + \nabla \cdot (\vec{V}v) \right) = -\frac{\partial p^+}{\partial y} + \nabla \cdot (\mu \nabla v) \quad (A.8)$$

$z$ -direction:

$$\rho \left( \frac{\partial w}{\partial t} + \nabla \cdot (\vec{V}w) \right) = -\frac{\partial p^+}{\partial z} + \nabla \cdot (\mu \nabla w) + \rho g \beta (T - T_0) \quad (A.9)$$



Conservation of energy:

$$\rho \left( \frac{\partial T}{\partial t} + \nabla \cdot (\vec{V}T) \right) = \nabla \cdot \left( \frac{k}{C_p} \nabla T \right) \quad (A.10)$$

Additional difficulties arise that are specific to buoyant flow problems in confined enclosures dealing with the multiple length and velocity scales (Ostrach and Austin, 1988). Non-dimensionalizing and normalizing the dimensional form of the governing equations require physically correct reference lengths and characteristic velocities to accurately solve the problem while still maintaining the physics of the problem. With this specific problem, as with other buoyant flow problems, there are multiple scale lengths and characteristic velocities depending upon the chamber location. The physics defining the fluid mechanics differ due to the prevailing dominate forces at various chamber locations. These dominate forces may vary from that of buoyancy forces, viscous forces, and diffusion forces. To accurately solve and reflect the physics of the entire problem, the different reference length scales and characteristic velocities in each of these regions must be correctly identified and be reflected in the non-dimensional and normalized sets of governing equations. Since these first sets of investigations were for the purpose of identifying the physics of the problem, only the dimensional sets of governing equations were solved numerically. With these initial and further parametric studies, the appropriate development of the problem in a non-dimensional normalized form may be addressed while still accurately addressing the physics of the problem.

This difficulty can best be illustrated by considering the possible multiple characteristic velocities in terms of the characteristic length scale depending upon the dominate forces governing the physics of the problem, (Ostrach, 1982):

$$V_c = \nu/L_c = (\text{viscous vs. inertia})$$

$$V_c = \alpha/L_c \text{ (convection vs. conduction)}$$

$$V_c = (\alpha\nu)^{.5}/L_c \text{ (combination)}$$

$$V_c = g\beta\Delta T_c L_c^2/\nu \text{ (buoyancy vs. viscous)}$$

$$V_c = (g\beta\Delta T_c L_c)^{.5} \text{ (buoyancy vs. inertia)}$$

## B) EXPOSURE CHAMBER OVERVIEW

Research efforts to determine the inhalation toxicity of a variety of airborne compounds utilize either whole-body or nose-only exposure methods. As a result, airborne compounds or toxicants that may consist of vapour, droplets, solid particulates, or a combination of the three have to be transported with maximum efficiency through a variety of flow elements so as to be inhaled by experimental animals. Transport tubes, mixers, and exposure chambers, for example, have inherent losses associated with their operation during the course of an experiment. This study addresses the whole-body exposure chamber and uses computational methods in conjunction with experimental data to develop a better understanding of physics of chamber operation for improvement, modification, and future development. Transport phenomenon such as diffusion and the convection of mass, enthalpy, and momentum play an important role on the efficiency of chamber operation. With the addition of heat generation from animal species within the chamber, these transport phenomenon are further complicated with the introduction of the free convection of heat, possibly altering flow patterns within the chamber.

There have been several exposure chamber configurations developed for inhalation toxicology studies. Figure A.2 shows four examples of the variety of possible chamber configurations which have been or are being used for inhalation research. Figure A.2a shows a horizontal flow chamber developed by Hemenway (1982) for which the toxicant is dispersed horizontally. Figure A.2b shows the multi-tiered chamber developed by Moss (1981) while Fig. A.2c and A.2d show a conventional pyramidal end cone "Hinnert-type" (Carpenter and Beethe, 1981)

and cylindrical chamber (Riley, 1986) type configurations. These chambers are generally fabricated of stainless steel and glass in order to minimize toxicant atmospheres reacting with the chamber. The primary purpose of these chambers has been to deliver well dispersed toxicants at low velocities to determine the toxic effects of various compounds.

Evaluation of these chambers have been performed by numerous investigators addressing spatial and temporal toxicant distributions within the chambers of interest for specific applications (Beethe et al., 1979; Yeh et al., 1986). The approach to addressing these spatial and temporal variations has been to sample at predetermined chamber locations by extracting a volume of air and toxicant over a given period of time and subsequently comparing the variation of the toxicant distribution within the chamber.

Additional evaluations of these chambers using flow visualization and quantitative models addressing the mean residence time of the chamber and the rate of dispersion of a toxicant within the chamber have also been performed (Carpenter and Beethe, 1981; Moss, 1981; Hemenway et al., 1986). Flow visualization techniques by Moss (1981) utilized a hydraulic water model with the injection of a tracer dye as the visual reference in determining the flow structure within the chamber while Carpenter (1981) injected  $\text{TiO}_2$ -HCL smoke into the chamber to ascertain the chamber flow structure. Quantitative information for the chamber as a whole was developed by Hemenway, et al. (1986) by addressing the chamber response to an injection of a toxicant or test material by comparing the inlet and exhaust profiles over time. This gave information as to the degree of chamber mixing, dead volume size, and shunting of the test material to the exhaust.

The effects of internal heat sources or animal species have been addressed by Bernstein and Drew (1981) and Yeh et al. (1988). Bernstein and Drew (1981) discussed animal loading and the effectiveness of eliminating or dissipating the heat load from the chamber. The effects of the heat sources on the chamber as a whole is discussed by Yeh (1988) showing the effects of spatial and temporal variation with and without animals.

Although these investigations have provided useful insight and information as to the overall performance, to date, there has been little use made of computational fluid dynamics for the evaluation and design of these chambers, nor have consideration as to what role the buoyancy forces play and what, if any are the possible effects due to sampling in determining spatial and temporal distributions.



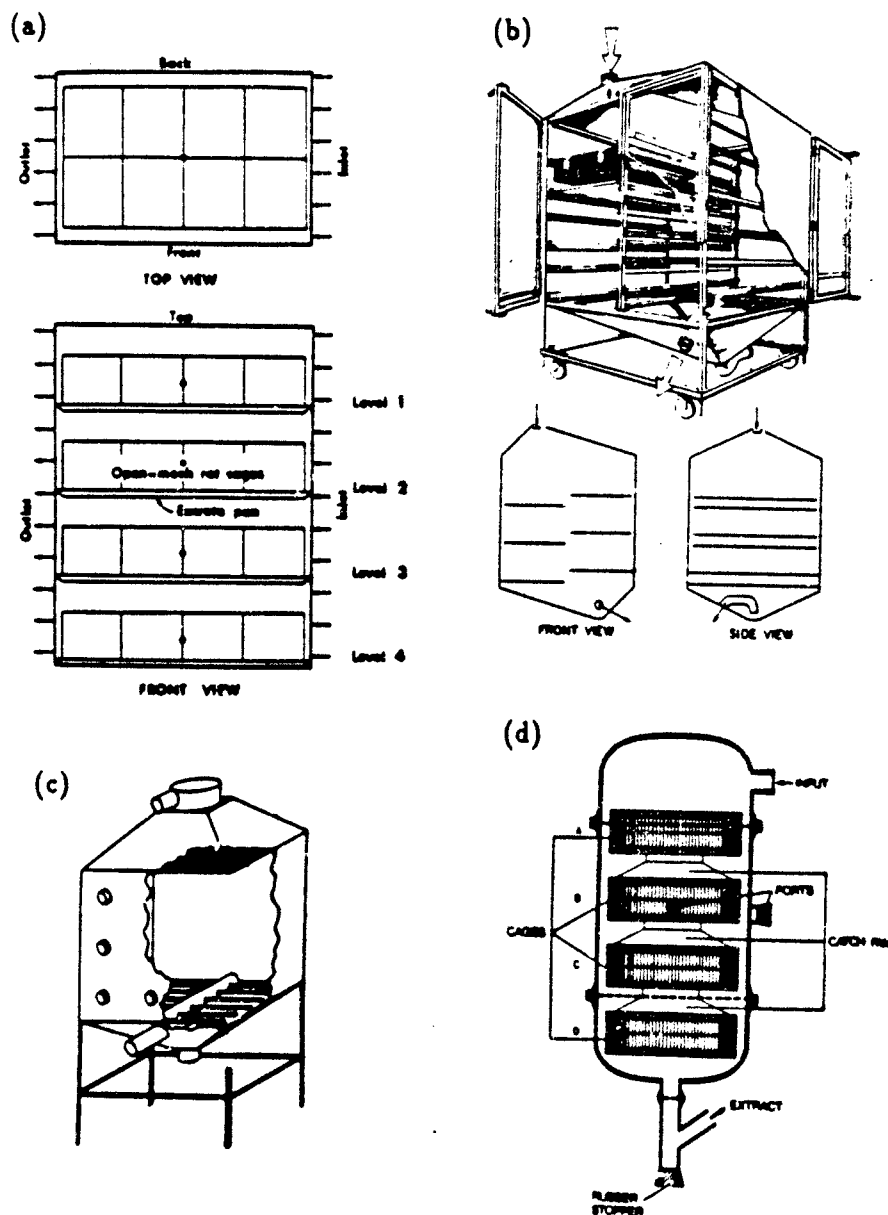


Fig. A.2 Possible chamber configurations in use for inhalation research  
 (a) horizontal flow chamber (b) multi-tiered chamber (c) pyramidal end cone  
 "Hinners-type" chamber (d) cylindrical chamber

## Appendix B: EXPERIMENTAL INSTRUMENTATION

### A) Rotameter pressure correction, calibration and use

#### i) Theory and use

The volumetric air flow rate through the experimental chamber was monitored and controlled using a Matheson "tube cube" rotameter. It is appropriate to review the theory of operation for these devices in addition to a method for pressure correction to determine the actual volumetric flow rate during operation.

A rotameter consists of a tapered tube in which some sort of a "float" assumes a vertical position corresponding to a given flow rate through the tube. The tapered tube diameter varies continuously with vertical displacement and serves three purposes:

- 1) Balance of the float is self maintaining.
- 2) Provides a constant pressure drop ( $\delta P$ ) for different flow rates. [Since  $\delta P = \delta P(Q^2)$ , for a fixed area, the tapered tube provides a variable area such that the  $\delta P$  is constant.]
- 3) If the taper varies linearly with height, the float position will vary linearly with flow rate.



Figure B.1 shows the free body diagram of a ball float that is suspended in the flow stream. The vertical forces consist of the ball weight, buoyant force, and drag force in which:

$$\sum F = 0 = -mg + [\text{buoyant force}] + [\text{drag force}] \quad (B.1)$$

where:

$$m = \rho_b V_b$$

$$[\text{buoyant force}] = \rho_f V_b g$$

$$[\text{drag force}] = \left( \frac{C_D \rho_f |V| A_b}{2} \right) V$$

Solving equation (B.1) for velocity and substituting into the conservation of mass where:

$$\begin{aligned} \frac{dm}{dt} &= \rho_f A V \\ \frac{dm}{dt} &= \rho_f A \left( \frac{2V_b g (\rho_b - \rho_f)}{(\rho_f A_b C_D)} \right)^{.5} \end{aligned} \quad (B.2)$$

The cross-sectional area,  $A$ , can further be defined in terms of tube taper and vertical position,  $y$  (note:  $D_o = d$ ):

$$A = \frac{\pi}{4} [(D_o + ay)^2 - d^2] \approx \frac{\pi}{2} D_o ay = \frac{\pi}{2} day \quad (B.3)$$

Substituting equation (B.3) into (B.2) and letting

$$K = \frac{\pi}{2} da \left( \frac{2V_b g}{(A_b C_D)} \right)^{.5}$$

we get:

$$\frac{dm}{dt} = Ky[(\rho_b - \rho_f) \rho_f]^{.5} \quad (B.4)$$

Now we have a relationship between the mass flow rate and the vertical displacement of the ball. For viscous fluids, the drag coefficient can be made nearly independent of viscosity by using sharp edge floats. For an ideal gas, in which a change in density will occur at differing pressures by way of the ideal gas law, there must be a pressure correction made to maintain an accurate measurement of the volumetric flow rate while the rotameter is in use.

## ii) Rotameter pressure correction

Consider two application in which the first is the rotameter operating at some reference pressure and temperature without an external operational pressure drop as shown in Fig. B.2a. The second application is one in which the rotameter is operated at some displaced pressure and temperature with an external operating pressure drop as shown in Fig. B.2b. For convenience, the first application will be considered to be the conditions for calibration of the rotameter. For both applications, the ball position is assumed to be fixed, therefore  $K$  may be assumed to be constant if the drag coefficient is constant. If for both applications the fluid type remains constant and the pressure and temperature range is small,

changes in drag coefficient may be assumed to be small. For each condition, equation (B.4) can be used in which the product  $Ky$  is constant resulting in the following two equations:

$$Ky = \frac{(dm/dt)_2}{[(\rho_b - \rho_2) \rho_2]^{.5}}$$

$$Ky = \frac{(dm/dt)_o}{[(\rho_b - \rho_o) \rho_o]^{.5}}$$

Equating these two equations gives the following:

$$\frac{(dm/dt)_2}{(dm/dt)_o} = \left( \frac{(\rho_b - \rho_2) \rho_2}{(\rho_b - \rho_o) \rho_o} \right)^{.5} \quad (B.5)$$

If the float is chosen such that the ball density is much greater than the fluid density and using  $dm/dt = \rho AV = \rho Q = \text{constant}$ , equation (B.5) is further reduced to :

$$\frac{\rho_1 Q_1}{\rho_o Q_o} = \left( \frac{\rho_2}{\rho_o} \right)^{.5} \quad (B.6)$$

where

$$\left( \frac{dm}{dt} \right)_2 = \rho_2 Q_2 = \rho_1 Q_1$$

Now, including the ideal gas law where  $\rho = P/(RT)$ , equation (B.6) can be put in terms of pressure and temperature. Since the drag coefficient was assumed to be constant due to a constant fluid type, the gas constant is also assumed to be constant. Making these substitutions and solving for  $Q_1$ , equation (B.6) becomes:

$$Q_1 = Q_o \left( \frac{T_1 P_o}{T_o P_1} \right) \left( \frac{P_2 T_o}{P_o T_2} \right)^{.5} \quad (B.7)$$

If the temperature,  $T_1 = T_2$  for adiabatic conditions, the final correction equation becomes, for adiabatic and frictionless flow:

$$Q_1 = Q_o \left( \frac{P_o}{P_1} \right) \left( \frac{P_2 T_1}{P_c T_o} \right)^{.5}$$

or in terms of  $\delta P$ :

$$Q_1 = Q_o \left( \frac{(1 + \delta P/P_1) P_o T_1}{P_1 T_o} \right)^{.5} \quad (B.8)$$

Generally, the calibration conditions are approximate to the operational conditions. If this is so, the final equation will further reduce to:

$$Q_1 = Q_o \left( 1 + \frac{\delta P}{P_{atm}} \right)^{.5} \quad (B.9)$$

The final equations (B.8) and (B.9) can now be used as a means of pressure correction the flow through a rotameter either form a calibration curve or when a calibration curve is determined for which there will usually be a pressure drop associated with the calibration device. In all instances, the calibration curve must be determined and corrected for a pressure drop equal to zero. It must be noted that there is a limitation on this form the correction equation. The flow from the rotameter to point in which the volumetric flow rate must be determined was assumed to be adiabatic and frictionless. For cases in which the gas flow coming out of the rotameter becomes critical or has heat added, there may be significant error to be considered.

### iii) Rotameter calibration and error analysis

Calibration of rotameters is performed using a calibrated standard as a reference. An NBS traceable calibration device is used such as a bubble flow meter, a dry or wet test meter, laminar flow element, etc. In addition to the calibrated flow measuring reference, a pressure reference to determine the calibration setup pressure drop and additional calibration instrumentation such as a barometer, and thermometer for determining the ambient air pressure and temperature are required.

Each of the above mentioned instrumentation devices have some error associated with their used. This error must be considered during the calibration procedure to determine the overall calibration error due to the instrumentation. Instrument precision, accuracy, and resolution must all be considered when evaluating instrument error. An additional error due to the ability of the calibrator or operator to set the rotameter float at any given setting consistently must also be considered. This repeatability error must be added to the instrument error in order to determine the overall rotameter calibration error.

If a function,  $\Phi$ , is considered in which  $\Phi = \Phi(\alpha, \beta, \gamma)$ , the total error for  $\Phi$  can be determined by the following relation, (Doebelin, 1983):

$$E_{\Phi} = \left| \left( \frac{\partial \Phi}{\partial \alpha} \right) \Delta \alpha \right| + \left| \left( \frac{\partial \Phi}{\partial \beta} \right) \Delta \beta \right| + \left| \left( \frac{\partial \Phi}{\partial \gamma} \right) \Delta \gamma \right| \quad (B.10)$$

where  $\Delta ( )$  is the error associated with the measurement of the appropriate independent variable.

For the calibration of a rotameter, equation (B.9) can be used with the appropriate assumptions. Using equation (B.10), the error in the calibrated flow rate can be calculated if the instrument error in the independent variables is known. Thus the corrected calibration flow rate,  $Q_o$ , for a rotameter can be found by the following relation derived from equation (B.9):

$$Q_o = \frac{Q_1}{(1 + \delta P/P_{atm})^{.5}}$$

where:

$$Q_1 = \frac{V_g}{t}$$

and:

$Q_1 \equiv$  indicated calibrated volumetric flow rate at an operational  $\delta P$

$Q_o \equiv$  corrected calibrated volumetric flow rate at  $\delta P = 0$

the instrument error now becomes:

$$E_{Q_o} = \frac{Q_o}{2} \left( \frac{2\Delta Q_1}{Q_1} + \frac{\Delta P_{atm} \delta P}{(1 + \delta P/P_{atm}) P_{atm}^2} + \frac{\Delta P(\delta P)}{(1 + \delta P/P_{atm}) P_{atm}} \right) \quad (B.11)$$

$$E_{Q_1} = \Delta Q_1 = \frac{\Delta V_g}{t} + \frac{V_g \Delta t}{t^2} \quad (B.12)$$

Now the calibrated volumetric flow rate can be determined with the appropriate instrument error where we have  $Q_o \pm EQ_o$ .

When the rotameter is in use, and with the appropriate assumptions, equation (B.9) can again be used to determine the unknown  $Q_1$  from the operational pressure drop,  $\delta P$ , and calibration volumetric flow rate,  $Q_o$ . Now, the corrected volumetric flow rate at an operational  $\delta P$  can be calculated. The method as described above can be used to determine the operational instrument error of the rotameter.

Repeatability error can be determined simply as the maximum deviation in volumetric flow rate when multiple repeated float settings are made. This error along with the maximum deviation due to the instrumentation error can be added to determine the maximum calibration error over the range calibrated. This total error can be stated in terms of percent of the range calibrated or in volumetric flow rate units only.

Actual use of the calibrated data usually involves fitting and algebraic function to this data. In this form, calibration information can easily be interpolated between the actual calibration points. However, there is also some error associated with the algebraic function when compared to the actual calibration data. Goodness of fit tests and or control charts with the appropriate confidence intervals are then required to determine the extent to which the information being obtained from the calibrated curve function is correct or if the calibration of a specific instrument is remaining valid. Generally, for a rotameter, a piecewise linear fit is sufficiently accurate (assuming there are enough calibration points)

and within the total rotameter error such that the error due to the curve fit can be neglected.

The calibration curve for the rotameter utilized in the experimental apparatus is shown in Fig. B.3. A dry test meter was used as the reference calibration standard with a full scale error of  $\pm 0.1$  lt/min over the calibrated range of 3.0 lt/min to 19.0 lt/min.

## B) Thermocouple calibration and use

### i) Theory and use

Thermocouples are a first order response temperature measurement device for which dissimilar metals generate a voltage (Seebeck voltage) which is almost linear for small changes in temperature. To measure temperature accurately, a reference junction must be used in conjunction with the thermocouple. This reference junction generally consists of an additional thermocouple maintained at a constant temperature, usually that of the melting point of ice commonly referred to as an ice point reference.

Thermocouples generally have an error of  $\pm 1.0^{\circ}\text{C}$  to  $\pm 2.0^{\circ}\text{C}$  depending upon the specific type of thermocouple used. If a thermocouple is individually calibrated this error may be reduced to  $\pm 0.1^{\circ}\text{C}$  providing the voltage measurement sensitivity can be obtained. Exposed junction iron-constantan type thermocouples were used for these investigations requiring that the voltage measure-



ment sensitivity be  $5.1 \mu\text{v}$  for a  $\pm 0.1^\circ\text{C}$  resolution in temperature measurement. Switching between thermocouples was performed using an isothermal thermocouple switch which was insulated to minimize stray emf. The thermocouple output was amplified with a gain of 100 and the resulting voltage monitored using a digital voltmeter. The ice point reference utilized either an ice bath or electronic ice point for which error induced due to ambient temperature variation was negligible. The temperature measurement setup was subsequently maintained and calibrated as a whole to minimize the additive errors for each of the components such as wires, amplifier, ice point reference, etc. An additional reference temperature to zero the amplifier was taken at the ice point reference. This temperature was periodically monitored to verify the existence of electronic drift and reset the amplifier zero prior to taking temperature measurements.

## ii) Thermocouple calibration

Thermocouple calibrations were performed using an ERTCO PG-108 (Ever Ready Thermometer Co., New York, N.Y.) NBS traceable (NBS Identification No. 311474) mercury thermometer with a resolution of  $\pm 0.05^\circ\text{C}$ . Both the thermocouple and the calibration reference were mounted together and placed in a Lauda circulating water bath and the temperature varied over the range of anticipated temperature measurement ( $24.0^\circ\text{C} - 32.0^\circ\text{C}$ ). This procedure was repeated and subsequently checked periodically to verify calibration over the course of the experiment.

Thermocouple output voltage was found to be linear over the range of temperatures calibrated with a static sensitivity,  $K^*$ , of approximately  $5.1 \mu\text{v}/0.1^\circ\text{C}$ .

A typical calibration curve is shown in Fig. B.4 with a 99% confidence band for the linear fit of the calibration data.

### iii) Thermocouple frequency response

Exposed junction thermocouples with a junction bead diameter ranging from 0.025 cm to 0.076 cm for a time constant of 1.35 to 1.73 seconds respectively were used for these investigations. Measurement of the transient temperature fields required that information with regard to the frequency response of the thermocouples be determined to evaluate the attenuation and phase shift of the measured transient temperature variation. The following relation for a first order instrument response shows the amplitude ratio,  $AR$ , of the input and output signal or fraction of attenuation and the phase angle for a given instrument time constant,  $\tau$ , and frequency,  $\omega$ , of the signal to be measured, (Doebelin, 1983):

$$AR = \frac{q_o}{q_i} = \frac{K^*}{(\omega^2 \tau^2 + 1)^{.5}} \angle \tan^{-1}(-\omega \tau) \quad (B.13)$$

where:

$$AR_{db} = 20 \log AR$$

Figure B.5 shows a Bode plot of a first order instrument while Table B.1 shows the amplitude ratio and phase shift for a time constant,  $\tau=1.7s$ .

## C) Hot wire/hot film anemometer calibration and use

### i) Theory and use

Hot wire/hot film anemometers consist of heating a wire or film sensor by passing a current through a wire or film, (Doebelin, 1983). As a fluid passes across the wire or film, the amount of heat convected and the resulting drop in sensor temperature for a constant current or change in the current required to maintain a constant sensor temperature is a direct measure of fluid velocity. Typical hot wire sensors are constructed of materials which are certified to maintain consistent properties, the most commonly used wire being a platinum coated tungsten wire with a high coefficient of resistance ( $\approx 0.004$  ohms/ $^{\circ}\text{C}$ ). Typical hot film sensors consist of a fused quartz substrate with a high purity platinum film bonded to the surface. Platinum provides the most stable, anticorrosive film material available with the proper resistance characteristics for thermal anemometry. Film sensors are also coated with either alumina for gas flows or quartz for liquids.

For equilibrium conditions, the following relation relating the current through the sensor,  $I$ , sensor temperature,  $T_{\text{wire}}$ , and sensor resistance,  $R_{\text{wire}}$  to fluid velocity,  $V$  where:

$$I^2 R_{\text{wire}} = hA (T_{\text{wire}} - T_f) \quad (B.14)$$

where the film coefficient has the general form (*King's law*):

$$h = C_0 + C_1 \sqrt{V}$$

For these investigations, velocity data was obtained using a TSI IFA-100 hot wire anemometer using a platinum film sensor model #1211-10 with a manufacturer rated typical upper frequency response in air at 100 m/s is 300 kHz. For this anemometer, the sensor current is constant while changes in the sensor temperature are measured by changes in the wire resistance. A bridge circuit is used

to indicate a change in sensor resistance by means of a change in bridge voltage which is directly related to the fluid velocity. The platinum film sensor that was used resolves the velocity in two dimensions in a cross flow configuration. Velocity components parallel to the sensor were not resolved.

## ii) Hot wire anemometer calibration

To effectively use the hot wire anemometer, the magnitude of the buoyant-induced velocity, due to the heating of the sensor, in relation to the velocity to be measured was of interest. Uncertainty errors can be determined depending upon the orientation of the fluid velocity to that of the induced buoyant velocity as described by TSI (TSI TB 14). This is evident when the stream velocity is opposed to the sensor-induced buoyant velocity and of the same order of magnitude.

Calibration of the hot wire anemometer was conducted using a laminar calibration cell fabricated to provide a uniform velocity profile as shown in Fig. B.6. Volumetric flow rate was controlled and monitored using a calibrated rotameter as previously discussed. Two sets of calibration runs are shown (I and II) in Fig. B.7 with the calibration velocity or flow either being opposed (flow down) or aligned (flow up) with the sensor-induced buoyant velocity. This resulted in a pronounced decrease in the output voltage for the calibration velocity being opposed to the sensor-induced velocity when compared to a calibration velocity being aligned with the sensor-induced velocity. For the specific sensor that was calibrated here, the buoyant induced velocity ranged from 0.010 m/s to 0.020 m/s with a sensor sensitivity ranging from  $0.50 \times 10^3 - 1.0 \times 10^3$  mV/(m/s) for velocities from 0.020 m/s to 0.030 m/s.

Discrepancies between runs I and II appear to be related to changes in the fluid temperature altering the sensor output as would be related to equation (B.14). With a change in fluid temperature, the sensor resistance or temperature is shifted at equilibrium resulting in a shift in the sensor output for the same velocity.

Table B.1  
THERMOCOUPLE FREQUENCY RESPONSE  
AMPLITUDE RATIO AND PHASE SHIFT ( $\tau=1.7s$ )

| $\omega$ (rad/sec) | $AR$  | phase angle (deg) |
|--------------------|-------|-------------------|
| 0.10               | 0.986 | -9.65             |
| 0.20               | 0.947 | -18.8             |
| 0.30               | 0.891 | -27.0             |
| 0.40               | 0.827 | -34.2             |
| 0.50               | 0.762 | -40.4             |
| 0.60               | 0.700 | -45.6             |
| 0.70               | 0.643 | -50.0             |
| 0.80               | 0.592 | -53.7             |
| 0.90               | 0.547 | -56.8             |
| 1.00               | 0.507 | -59.5             |

[DRAG + BUOYANCY]



[WEIGHT]

Fig. B.1 Free body diagram of rotameter float

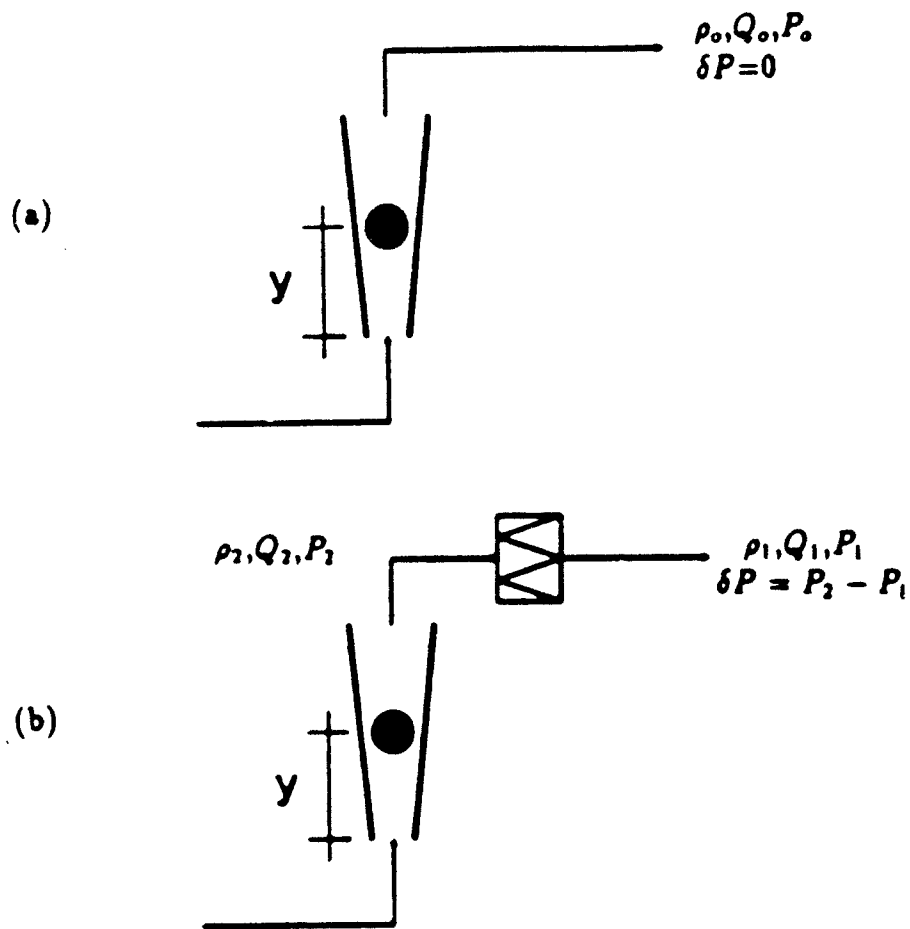


Fig. B.2 Rotameter application schematic (a) operational pressure drop,  $\delta P = 0$  (b) operational pressure drop,  $\delta P \neq 0$



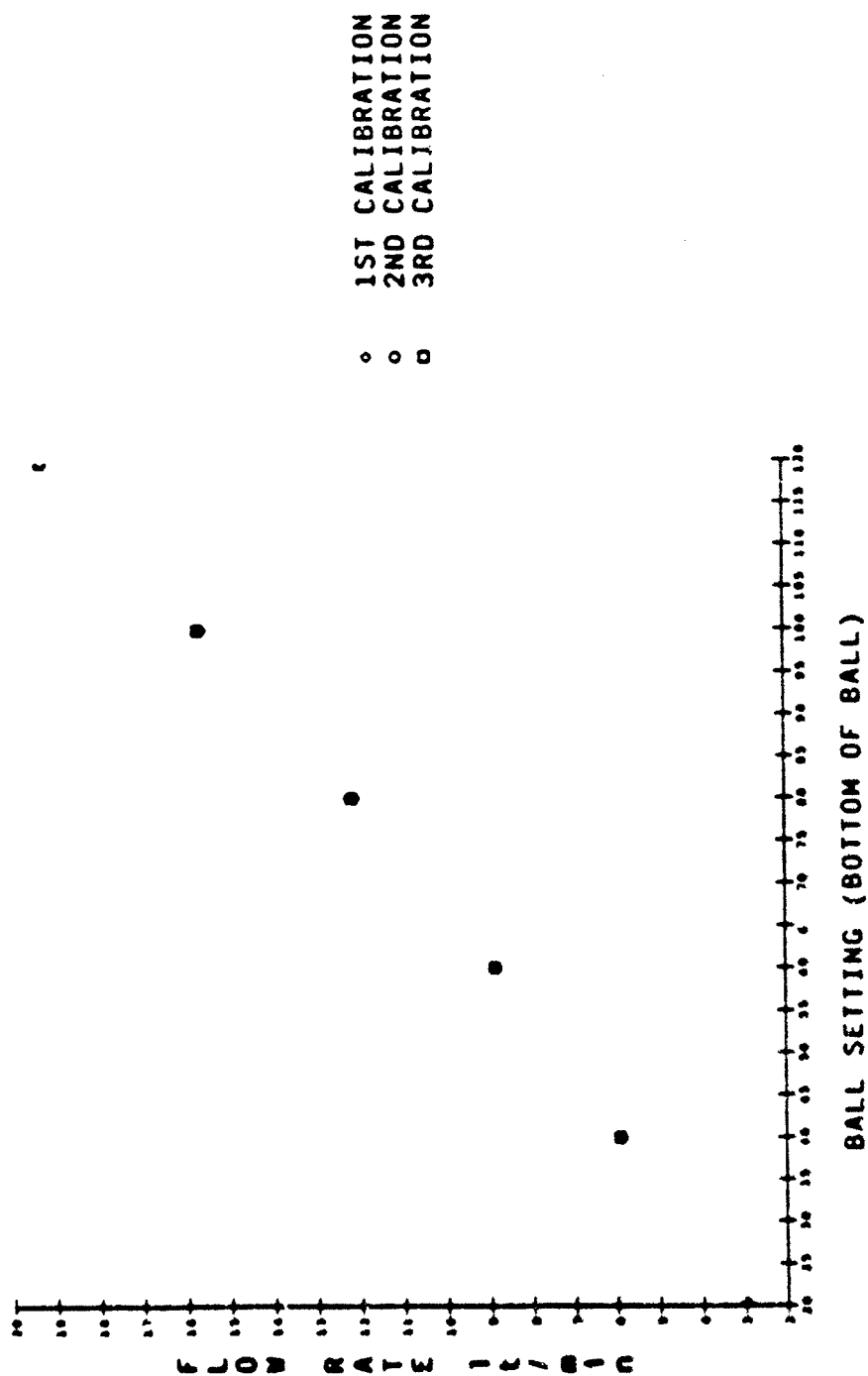


Fig. B.3 rotameter inlet air calibration curve corrected for  $\delta P = 0$

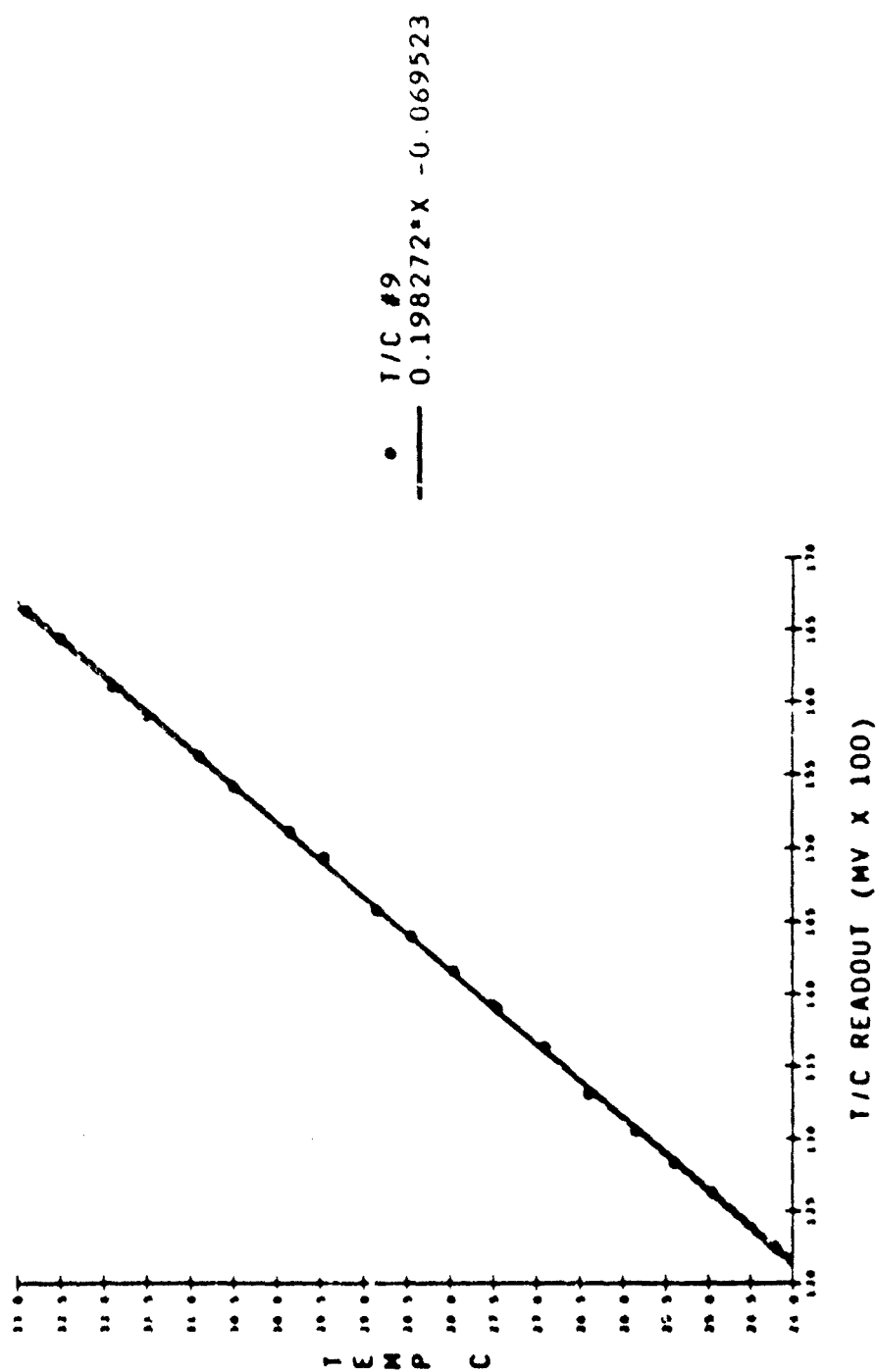


Fig. B.4 Thermocouple calibration curve over the anticipated range of operation with a 99 percent confidence band for the linear fit

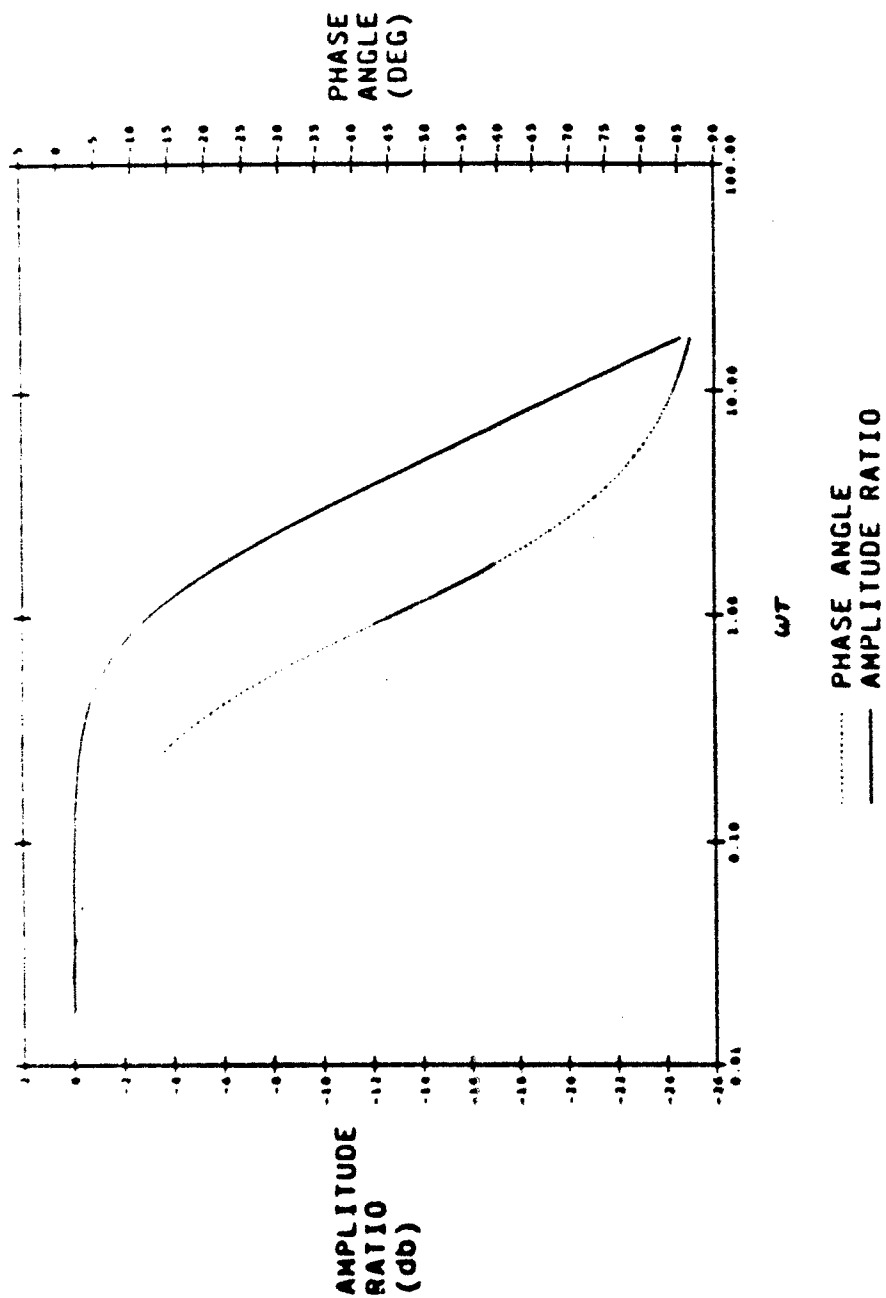


Fig. B.5 Thermocouple first order instrument Bode plot

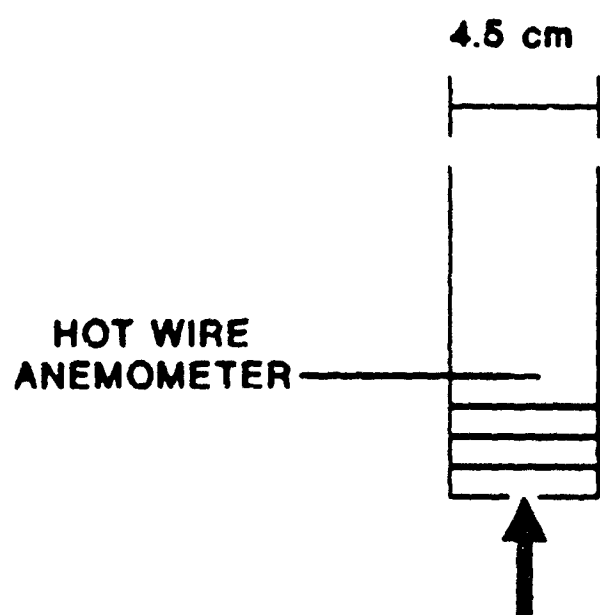


Fig. B.6 Hot wire anemometer calibration cell

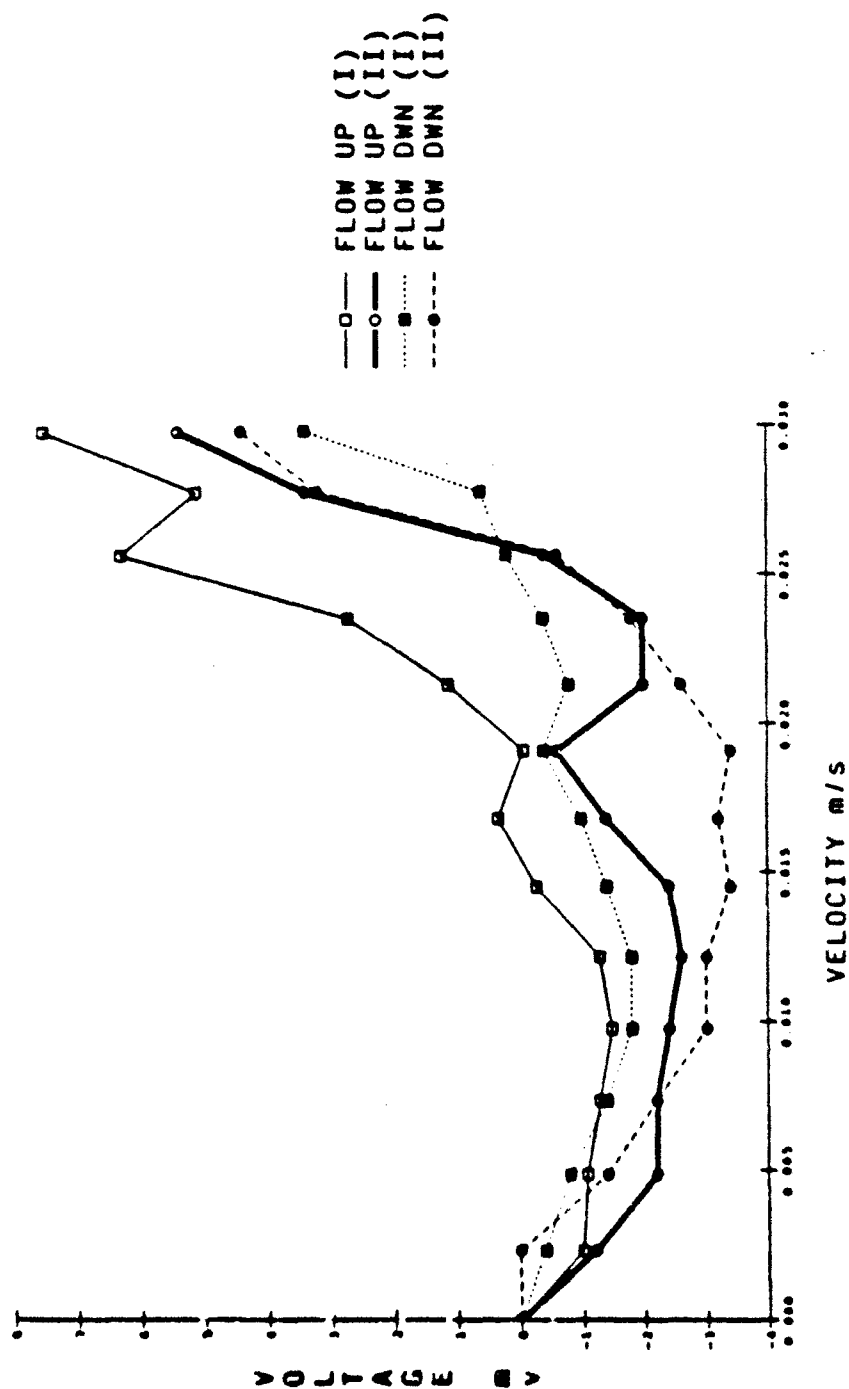


Fig. B.7 Hot wire anemometer calibration curves for aligned (flow up) and opposed (flow down) calibration velocities

## Appendix C: NUMERICAL FORMULATION (PHOENICS)

### i) Q1-File (two-dimensional formulation)

This is a description of the Phoenix Q1 input file. Each group is explained as appropriate to convey the problem approach specific to the Phoenix software package utilized for the two-dimensional investigations.

#### Group 1: Run title and preliminaries

- Problem title and description with variable assignment.

#### Group 2: Time dependence and related parameters

- Set problem to transient.
- Use method of pairs for time step specification.

#### Group 3: X-direction grid specification

- Set rectangular coordinate system.
- Default to a one meter deep chamber.

Group 4: Y-direction grid specification

- Use method of pairs for y-direction grid layout.

Group 5: Z-direction grid specification

- Use method of pairs for z-direction grid layout.

Group 7: Variables solved, stored and named

- Single phase fluid specified.
- Solve for and store dependent variables  $P1$ ,  $V1$ ,  $W1$ ,  $H1$ .
- Use implicit slab-by-slab method of solution for velocity and enthalpy.
- Use implicit whole-field method of solution for pressure.
- Use harmonic averaging of the exchange coefficient.

Group 8: Terms in the differential equations

- Built in source terms active for velocity components (pressure term included in momentum equations).

- Built in source terms inactive for enthalpy (viscous dissipation and pressure work terms not included in formulation).
- Convection, diffusion, and transient terms active for dependent variables.
- Dependent variables belong to first phase in a single phase formulation.

#### Group 9: Fluid properties

- Kinematic viscosity, density, Prandtl number specified for fluid.

#### Group 11: Variable initialization

- Choice of restarting [RESTRT(ALL)] from a previous solution or starting from an initial field specified using the FIINIT() command.

#### Group 13: Boundary conditions and special sources

- Chamber inlet boundary

Specifies a uniform velocity and temperature on the upper most cell surface across the width and depth of the chamber



-Chamber outlet boundary

Specifies a reference pressure of zero across the outlet lower most cell surface. This resembles the conditions similar to a porous boundary outlet in which the exhaust side is at a uniform and constant pressure. Specifies an outlet enthalpy to be the same as that of the upstream neighbor cells exhibiting a local parabolic behavior at the outlet boundary.

-Chamber vertical end wall boundary

Specifies a constant temperature wall with no-slip condition for velocity.

-Chamber pan boundary

Specifies an infinitesimally thick pan represented by setting the velocity components to zero along the lower cell walls.

-Chamber heat source boundary

Heat sources are represented by specifying a zero velocity at the cell location within the heat source area and setting the temperature in the blocked region to be constant.

-Buoyancy boundary using the Boussinesq approximation

The Boussinesq approximation using a ground subroutine is used to include the buoyancy source term in the vertical direction. Note coordinate reversal to

be consistent with the inlet and outlet as specified in Phoenix.

Group 15: Termination of sweeps

-Sweep number and residual limits are specified

Group 17: Under-relaxation

-Under-relaxation is specified using FALSDT equal to 1.0. The time step was used to control the amount of relaxation required for specific solutions.

```

TALK=T:RUN( 1, 1);VDU=TTY
GROUP 1. Run identifier and other preliminaries
TEXT(2-D CHAMBER FLOW MODEL W/ HEAT SOURCES)
  This is a two-dimensional model representing a large rectangular
  chambers with baffles and constant temperature heat sources.
  The dimensions are .686m vertical and .813m horizontal.
  This is the symmetric transient model.
  .... VOLUMETRIC FLOW (CFM) -----QIN
  .... INLET VELOCITY (M/SEC) -----WIN
  .... INLET TEMPERATURE (DEG C) -----TIN
  .... WALL TEMPERATURE (DEG C) -----TWALL
  .... INLET PRESSURE (PSIA) -----PIN
  .... INLET DENSITY (KG/CU M) -----DENSIN
  .... INLET VISCOSITY (N SEC/SQ M) -----VISCIN
  .... INLET KINEMATIC VISCOSITY (SQ M/SEC) -----ENULIN
  .... COEFFICIENT OF EXPANSION (1/DEG K) -----BETA
  .... CHAMBER WIDTH (METER) -----L
  .... CHAMBER HEIGHT (METER) -----H
  .... NUMBER OF TIME STEPS -----NT
  .... TIME STEP (SEC) -----DT
  .... START TIME (SEC) -----TSTRT
  .... STOP TIME (SEC) -----TSTOP
REAL(QIN,WIN,TIN,TWALL,PIN,DENSIN,VISCIN,ENULIN,BETA)
REAL(TSTRT,TSTOP,DT,L,H)
INTEGER(NT,DY1,DY2,DY3,DY4,DY5,DY6,DY7,DY8,DY9,DY10,DY11,DY12,DY13)
INTEGER(DZ1,DZ2,DZ3,DZ4,DZ5,DZ6,DZ7,A,B,C,D)
  **for time step ((TSTOP-TSTRT)=DT*NT)**
DT=.05
NT=400
TSTAT=0.0
TSTOP=20.0
PIN=14.4
QIN=5.8
TIN=27.3
  TIN=25.0
  TIN=21.0
  TIN=23.0
  TIN=24.0
TWALL=24.0
WIN=QIN/1.4114E3
BETA=1.0/(273.2+TIN)
DENSIN=PIN*43.24/(492+1.8*TIN)
VISCIN=1.458E-6*(273.2+TIN)**1.5/(383.6+TIN)
ENULIN=VISCIN/DENSIN
L=.813
DY1=6;DY2=1;DY3=13;DY4=10;DY5=13;DY6=1;DY7=12
DY8=1;DY9=13;DY10=10;DY11=13;DY12=1;DY13=6
NY=DY1+DY2+DY3+DY4+DY5+DY6+DY7+DY8+DY9+DY10+DY11+DY12+DY13
A=DY1+DY2+DY3+DY4+DY5+DY6
B=NY-DY13-DY12-DY11-DY10-DY9-DY8+1
C=NY-DY13-DY12-DY11+1
H=.686
DZ1=38;DZ2=8;DZ3=2;DZ4=35;DZ5=8;DZ6=2;DZ7=7
NZ=DZ1+DZ2+DZ3+DZ4+DZ5+DZ6+DZ7
D=NZ-DZ7-DZ6-DZ5+1

```

```

      GROUP 2. Time dependence and related parameters
STEADY=F
TFIRST=TSTART
TLAST=TSTOP
LSTEP=NT
TFRAC(1)=-NT
TFRAC(2)=DT/(TSTOP-TSTART)
      GROUP 3. X-direction grid
CARTES=T
      GROUP 4. Y-direction grid
YVLAST=L
YFRAC(1)=-DY1;YFRAC(2)=6.0E-2/DY1
YFRAC(3)=DY2;YFRAC(4)=1.0E-2/DY2
YFRAC(5)=DY3;YFRAC(6)=.13/DY3
YFRAC(7)=DY4;YFRAC(8)=.10/DY4
YFRAC(9)=DY5;YFRAC(10)=.13/DY5
YFRAC(11)=DY6;YFRAC(12)=1.0E-2/DY6
YFRAC(13)=DY7;YFRAC(14)=.12/DY7
YFRAC(15)=DY8;YFRAC(16)=1.0E-2/DY8
YFRAC(17)=DY9;YFRAC(18)=.13/DY9
YFRAC(19)=DY10;YFRAC(20)=.10/DY10
YFRAC(21)=DY11;YFRAC(22)=.13/DY11
YFRAC(23)=DY12;YFRAC(24)=1.0E-2/DY12
YFRAC(25)=DY13;YFRAC(26)=6.0E-2/DY13
      GROUP 5. Z-direction grid
ZWLAST=M
ZFRAC(1)=-DZ1;ZFRAC(2)=.38/DZ1
ZFRAC(3)=DZ2;ZFRAC(4)=8.0E-2/DZ2
ZFRAC(5)=DZ3;ZFRAC(6)=2.0E-2/DZ3
ZFRAC(7)=DZ4;ZFRAC(8)=.35/DZ4
ZFRAC(9)=DZ5;ZFRAC(10)=8.0E-2/DZ5
ZFRAC(11)=DZ6;ZFRAC(12)=2.0E-2/DZ6
ZFRAC(13)=DZ7;ZFRAC(14)=7.0E-2/DZ7
      GROUP 6. Body-fitted coordinates or grid distortion
      GROUP 7. Variables solved, stored and named
ONEPHS=T
SOLUTN(P1,Y,Y,Y,N,N,Y)
SOLUTN(W1,Y,Y,N,N,N,Y)
SOLUTN(V1,Y,Y,N,N,N,Y)
SOLUTN(H1,Y,Y,N,N,N,Y)
      GROUP 8. Terms (in differential equations and devices)
TERMS(V1,Y,Y,Y,Y,Y,N)
TERMS(W1,Y,Y,Y,Y,Y,N)
TERMS(H1,N,Y,Y,Y,Y,N)
      GROUP 9. Properties of the medium
ENUL=ENULIN
RHO1=DENSIN
PRNDTL(H1)=.7
      GROUP 10. Inter-phase-transfer processes and properties
      GROUP 11. Initialization of variables
FIINIT(H1)=(TIN+TWALL)/2
FIINIT(W1)=0.0
FIINIT(V1)=0.0
FIINIT(P1)=0.0
RESTART(ALL)

```

GROUP 12. Convection and diffusion adjustments

GROUP 13. Boundary conditions and special sources

\*\*inlet boundary conditions\*\*

PATCH(INLET,LOW,1,1,1,NY,1,1,1,NT)

COVAL(INLET,P1,FIXFLU,RHO1\*WIN)

COVAL(INLET,W1,ONLYMS,WIN)

COVAL(INLET,H1,ONLYMS,TIN)

\*\*outlet boundary conditions\*\*

PATCH(OUTLET,HIGH,1,1,1,NY,NZ,NZ,1,NT)

COVAL(OUTLET,P1,FIXP,0.0)

COVAL(OUTLET,H1,ONLYMS,SAME)

\*\*wall boundary conditions\*\*

PATCH(WALL1,SWALL,1,1,1,1,1,NZ,1,NT)

COVAL(WALL1,H1,1.0/PRNDTL(H1),TWALL)

COVAL(WALL1,W1,1.0,0.0)

COVAL(WALL1,V1,1.0,0.0)

PATCH(WALL2,NWALL,1,1,1,NY,NY,1,NZ,1,NT)

COVAL(WALL2,H1,1.0/PRNDTL(H1),TWALL)

COVAL(WALL2,W1,1.0,0.0)

COVAL(WALL2,V1,1.0,0.0)

\*\*span restriction represented by setting velocity=0\*\*

PATCH(PAN1,HIGH,1,1,DY1+1,A,DZ1+DZ2+DZ3,DZ1+DZ2+DZ3,1,NT)

COVAL(PAN1,W1,FIXVAL,0.0)

COVAL(PAN1,V1,FIXVAL,0.0)

PATCH(PAN2,HIGH,1,1,B,NY-DY13,DZ1+DZ2+DZ3,DZ1+DZ2+DZ3,1,NT)

COVAL(PAN2,W1,FIXVAL,0.0)

COVAL(PAN2,V1,FIXVAL,0.0)

PATCH(PAN3,HIGH,1,1,DY1+1,A,NZ-DZ7,NZ-DZ7,1,NT)

COVAL(PAN3,W1,FIXVAL,0.0)

COVAL(PAN3,V1,FIXVAL,0.0)

PATCH(PAN4,HIGH,1,1,B,NY-DY13,NZ-DZ7,NZ-DZ7,1,NT)

COVAL(PAN4,W1,FIXVAL,0.0)

COVAL(PAN4,V1,FIXVAL,0.0)

\*\*heat source representation\*\*

\*\*heater 1\*\*

PATCH(HTA1,CELL,1,1,DY1+DY2+1,DY1+DY2+DY3,DZ1+1,DZ1+DZ2,1,NT)

COVAL(HTA1,W1,FIXVAL,0.0)

COVAL(HTA1,V1,FIXVAL,0.0)

COVAL(HTA1,H1,FIXVAL,32.0)

\*\*heater 2\*\*

PATCH(HTA2,CELL,1,1,DY1+DY2+DY3+DY4+1,A-DY6,DZ1+1,DZ1+DZ2,1,NT)

COVAL(HTA2,W1,FIXVAL,0.0)

COVAL(HTA2,V1,FIXVAL,0.0)

COVAL(HTA2,H1,FIXVAL,32.0)

\*\*heater 3\*\*

PATCH(HTA3,CELL,1,1,B+DY8,NY-DY13-DY12-DY11-DY10,DZ1+1,DZ1+DZ2,1,NT)

COVAL(HTA3,W1,FIXVAL,0.0)

COVAL(HTA3,V1,FIXVAL,0.0)

COVAL(HTA3,H1,FIXVAL,32.0)

\*\*heater 4\*\*

PATCH(HTA4,CELL,1,1,C,NY-DY13-DY12,DZ1+1,DZ1+DZ2,1,NT)

COVAL(HTA4,W1,FIXVAL,0.0)

COVAL(HTA4,V1,FIXVAL,0.0)

COVAL(HTA4,H1,FIXVAL,32.0)

\*\*heater 5\*\*

```

PATCH(HTRS,CELL,1,1,DY1+DY2+1,DY1+DY2+DY3,D,NZ-DZ7-DZ6,1,NT)
COVAL(HTRS,W1,FIXVAL,0.0)
COVAL(HTRS,V1,FIXVAL,0.0)
COVAL(HTRS,H1,FIXVAL,32.0)
**heater 6**
PATCH(HTR6,CELL,1,1,DY1+DY2+DY3+DY4+1,A-DY6,D,NZ-DZ7-DZ6,1,NT)
COVAL(HTR6,W1,FIXVAL,0.0)
COVAL(HTR6,V1,FIXVAL,0.0)
COVAL(HTR6,H1,FIXVAL,32.0)
**heater 7**
PATCH(HTR7,CELL,1,1,B+DY8,NY-DY13-DY12-DY11-DY10,D,NZ-DZ7-DZ6,1,NT)
COVAL(HTR7,W1,FIXVAL,0.0)
COVAL(HTR7,V1,FIXVAL,0.0)
COVAL(HTR7,H1,FIXVAL,32.0)
**heater 8**
PATCH(HTR8,CELL,1,1,C,NY-DY13-DY12,D,NZ-DZ7-DZ6,1,NT)
COVAL(HTR8,W1,FIXVAL,0.0)
COVAL(HTR8,V1,FIXVAL,0.0)
COVAL(HTR8,H1,FIXVAL,32.0)
**buoyancy boundary--Boussinesq approximation**
**source term = RSG10*(RSG1+RSG2*H1) or g*beta*(Tin-T)**
** (note coordinate reversal)**
RSG10=9.81
PATCH(BUOY,PHASEM,1,1,1,NY,1,NZ,1,NT)
COVAL(BUOY,W1,FIXFLU,GRND3)
RSG2=-BETA
RSG1=BETA * TIN
GROUP 14. Downstream pressure for PARAB=TRUE.
GROUP 15. Termination of sweeps
LSWEEP=10
RESREF(P1)=1.E-6
RESREF(W1)=1.E-6
RESREF(V1)=1.E-6
RESREF(H1)=1.E-6
GROUP 16. Termination of iterations
GROUP 17. Under-relaxation
RELAX(W1,FALS DT,1.0)
RELAX(V1,FALS DT,1.0)
RELAX(H1,FALS DT,1.0)
RELAX(P1,FALS DT,1.0)
GROUP 18. Limits on variables or increments to them
GROUP 19. Data communicated by satellite to GROUND
GROUP 20. Preliminary print-out
PCMS=F
GROUP 21. Field and monitor control
OUTPUT(P1,Y,N,N,N,Y,Y)
OUTPUT(W1,Y,N,N,N,Y,Y)
OUTPUT(V1,Y,N,N,N,Y,Y)
OUTPUT(H1,Y,N,N,N,Y,Y)
GROUP 22. Spot value print-out
NORMON=1
IYMON=N1/2
IZMON=N2/4
IDPL=LSWEEP
GROUP 23. Field print-out and plot control

```

NPLT=1  
ORSIZ=.4  
NYPRIN=NY/20  
NZPRIN=NZ/10  
NTPRIN=NT/5  
ITABL=3  
STOP

ii) Q1-File (three-dimensional formulation)

This is a description of the Phoenix Q1 input file. Each group is explained as appropriate to convey the problem approach specific to the Phoenix software package utilized for the three-dimensional investigations.

Group 1: Run title and preliminaries

-Problem title and description with variable assignment.

Group 2: Time dependence and related parameters

-Set problem to transient.

-Use method of pairs for time step specification.

Group 3: X-direction grid specification

-Set rectangular coordinate system.

-Uniform grid spacing in the x-direction with five cells for a chamber depth of 6.668 cm.

Group 4: Y-direction grid specification



- Use method of pairs for y-direction grid layout.

#### Group 5: Z-direction grid specification

- Use method of pairs for z-direction grid layout.

#### Group 7: Variables solved, stored and named

- Single phase fluid specified.
- Solve for and store dependent variables  $P1$ ,  $V1$ ,  $W1$ ,  $H1$ .
- Use implicit slab-by-slab method of solution for velocity and enthalpy.
- Use implicit whole-field method of solution for pressure.
- Use harmonic averaging of the exchange coefficient.

#### Group 8: Terms in the differential equations

- Built in source terms active for velocity components (pressure term included in momentum equations).
- Built in source terms inactive for enthalpy (viscous dissipation and pressure work terms not included in formulation).

- Convection, diffusion, and transient terms active for dependent variables.
- Dependent variables belong to first phase in a single phase formulation.

#### Group 9: Fluid properties

- Kinematic viscosity, density, Prandtl number specified for fluid.

#### Group 11: Variable initialization

- Choice of restarting [RESTRT(ALL)] from a previous solution or starting from an initial field specified using the FIINIT() command.

#### Group 13: Boundary conditions and special sources

- Chamber inlet boundary

Specifies a uniform velocity and temperature on the upper most cell surface across the width and depth of the chamber

- Chamber outlet boundary

Specifies a reference pressure of zero across the outlet lower most cell surface. This resembles the conditions similar to a porous boundary outlet in which the exhaust side is at a uniform and constant pressure. Specifies an outlet enthalpy

to be the same as that of the upstream neighbor cells exhibiting a local parabolic behavior at the outlet boundary.

-Chamber vertical end wall boundary

Specifies a constant temperature wall with no-slip condition for velocity.

-Chamber vertical side wall boundary

Specifies either a constant temperature wall or defaults to an adiabatic wall with no-slip condition for velocity.

-Chamber pan boundary

Specifies an infinitesimally thick pan represented by setting the velocity components to zero along the lower cell walls. Pans span the depth of the chamber.

-Buoyancy boundary using the Boussinesq approximation

The Boussinesq approximation using a ground subroutine is used to include the buoyancy source term in the vertical direction. Note coordinate reversal to be consistent with the inlet and outlet as specified in Phoenix.

Group 15: Termination of sweeps

-Sweep number and residual limits are specified

Group 17: Under-relaxation

-Under-relaxation is specified using FALSDT equal to 1.0. The time step was used to control the amount of relaxation required for specific solutions.

```
TALK=T;RUN( 1, 1);VDU=TTY
GROUP 1. run identifier and other preliminaries
TEXT(3-D CHAMBER FLOW MODEL W/O HEAT SOURCES)
```

This is a three-dimensional model representing the laboratory experimental model with baffles.

The dimensions are .686m vertical and .813m horizontal and 6.67cm deep.

This is the symmetric transient model.

```
..... VOLUMETRIC FLOW (CFM) -----QIN
..... INLET VELOCITY (M/SEC) -----WIN
..... INLET TEMPERATURE (DEG C) -----TIN
..... WALL TEMPERATURE (DEG C) -----TWALL
..... INLET PRESSURE (PSIA) -----PIN
..... INLET DENSITY (KG/CU M) -----DENSIN
..... INLET VISCOSITY (IN SEC/SQ M) -----VISCIN
..... INLET KINEMATIC VISCOSITY (SQ M/SEC) -----ENULIN
..... COEFFICIENT OF EXPANSION (1/DEG K) -----BETA
..... SPECIFIC HEAT PHASE 1 (AIR) (J/KG DEG K) --CP1
..... WALL THERMAL CONDUCTIVITY (W/M DEG C) -----KCONW
..... WALL THICKNESS (M) -----WALTH
..... NUMBER OF TIME STEPS -----NT
..... TIME STEP (SEC) -----DT
..... START TIME (SEC) -----TSTART
..... STOP TIME (SEC) -----TSTOP
REAL(QIN,WIN,TIN,TWALL,TROOM,KCONW,PIN,DENSIN,VISCIN,ENULIN,BETA)
```

```
REAL(TSTART,TSTOP,DT,CP1,WALTH)
```

```
INTEGER(NT)
```

```
  **for time step [(TSTOP-TSTART)=DT*NT]**
```

```
DT=.5
```

```
NT=100
```

```
TSTART=0.0
```

```
TSTOP=50.0
```

```
CP1=1004.0
```

```
PIN=14.4
```

```
QIN=5.8
```

```
TIN=27.3
```

```
  TIN=25.0
```

```
  TIN=21.0
```

```
  TIN=23.0
```

```
  TIN=24.0
```

```
TWALL=24.0
```

```
TROOM=26.75
```

```
WIN=QIN/1.4114E3
```

```
BETA=1.0/(273.2+TIN)
```

```
DENSIN=PIN*43.24/(492+1.8*TIN)
```

```
VISCIN=1.458E-6*(273.2+TIN)**1.5/(383.6+TIN)
```

```
ENULIN=VISCIN/DENSIN
```

```
L=.813
```

```
DY1=6;DY2=1;DY3=13;DY4=10;DY5=13;DY6=1;DY7=12
```

```
DY8=1;DY9=13;DY10=10;DY11=13;DY12=1;DY13=6
```

```
NY=DY1+DY2+DY3+DY4+DY5+DY6+DY7+DY8+DY9+DY10+DY11+DY12+DY13
```

```
A=DY1+DY2+DY3+DY4+DY5+DY6
```

```
B=NY-DY13-DY12-DY11-DY10-DY9-DY8+1
```

```

C=NY-DY13-DY12-DY11+1
H=.686
DZ1=38;DZ2=8;DZ3=2;DZ4=35;DZ5=8;DZ6=2;DZ7=7
NZ=DZ1+DZ2+DZ3+DZ4+DZ5+DZ6+DZ7
D=NZ-DZ7-DZ6-DZ5+1
      GROUP 2. time dependence and related parameters
STEADY=F
T1=1ST=TSTART
T2=2ST=1STOP
LSTEP=NT
TFRAC(1)=-NT
TFRAC(2)=DT/(1STOP-TSTART)

      GROUP 3. x-direction grid
CARTES=T
GRDPWR(X,5,6,686E-2,1,0)
      GROUP 4. y-direction grid
YVLAST=L
YFRAC(1)=-DY1;YFRAC(2)=6.0E-2/DY1
YFRAC(3)=DY2;YFRAC(4)=1.0E-2/DY2
YFRAC(5)=DY3;YFRAC(6)=.13/DY3
YFRAC(7)=DY4;YFRAC(8)=.10/DY4
YFRAC(9)=DY5;YFRAC(10)=.13/DY5
YFRAC(11)=DY6;YFRAC(12)=1.0E-2/DY6
YFRAC(13)=DY7;YFRAC(14)=.12/DY7
YFRAC(15)=DY8;YFRAC(16)=1.0E-2/DY8
YFRAC(17)=DY9;YFRAC(18)=.13/DY9
YFRAC(19)=DY10;YFRAC(20)=.10/DY10
YFRAC(21)=DY11;YFRAC(22)=.13/DY11
YFRAC(23)=DY12;YFRAC(24)=1.0E-2/DY12
YFRAC(25)=DY13;YFRAC(26)=6.0E-2/DY13
      GROUP 5. z-direction grid
ZVLAST=M
ZFRAC(1)=-DZ1;ZFRAC(2)=.38/DZ1
ZFRAC(3)=DZ2;ZFRAC(4)=8.0E-2/DZ2
ZFRAC(5)=DZ3;ZFRAC(6)=2.0E-2/DZ3
ZFRAC(7)=DZ4;ZFRAC(8)=.35/DZ4
ZFRAC(9)=DZ5;ZFRAC(10)=8.0E-2/DZ5
ZFRAC(11)=DZ6;ZFRAC(12)=2.0E-2/DZ6
ZFRAC(13)=DZ7;ZFRAC(14)=7.0E-2/DZ7
      GROUP 6. Body-fitted coordinates on grid distortion
      GROUP 7. variables solved, stored and named
ONEPHS=T
SOLUTN(P1,Y,Y,Y,N,N,Y)
SOLUTN(W1,Y,Y,N,N,N,Y)
SOLUTN(V1,Y,Y,N,N,N,Y)
SOLUTN(U1,Y,Y,N,N,N,Y)
SOLUTN(M1,Y,Y,N,N,N,Y)
      GROUP 8. terms (in differential equations and devices)
TERMS(V1,Y,Y,Y,Y,Y,N)
TERMS(U1,Y,Y,Y,Y,Y,N)
TERMS(W1,Y,Y,Y,Y,Y,N)
TERMS(M1,N,Y,Y,Y,Y,N)
      GROUP 9. properties of the medium
ENUL=ENULIN

```

```

RHO1=DENSIN
PRNDTL(H1)=.7
  GROUP 10. Inter-phase-transfer processes and properties
  GROUP 11. initialization of variables
    FIINIT(H1)=TROOM
    FIINIT(W1)=0.0
    FIINIT(P1)=0.0
  RESTART(ALL)
  GROUP 12. Convection and diffusion adjustments
  GROUP 13. boundary conditions and special sources
    **inlet boundary conditions**
    PATCH(INLET,LOW,1,NX,1,NY,1,1,1,NT)
    COVAL(INLET,P1,FIXFLU,RHO1*WIN)
    COVAL(INLET,W1,ONLYMS,WIN)
    COVAL(INLET,H1,ONLYMS,TIN)
    **outlet boundary conditions**
    PATCH(OUTLET,HIGH,1,NX,1,NY,NZ,NZ,1,NT)
    COVAL(OUTLET,P1,FIXP,0.0)
    COVAL(OUTLET,H1,ONLYMS,SAME)
    **wall boundary conditions**
    PATCH(WALL1,SWALL,1,NX,1,1,1,NZ,1,NT)
    COVAL(WALL1,H1,1.0/PRNDTL(H1),TWALL)
    COVAL(WALL1,W1,1.0,0.0)
    COVAL(WALL1,U1,1.0,0.0)
    COVAL(WALL1,V1,1.0,0.0)
    PATCH(WALL2,NWALL,1,NX,NY,NY,1,NZ,1,NT)
    COVAL(WALL2,H1,1.0/PRNDTL(H1),TWALL)
    COVAL(WALL2,W1,1.0,0.0)
    COVAL(WALL2,U1,1.0,0.0)
    COVAL(WALL2,V1,1.0,0.0)
    PATCH(WALL3,WALL,1,1,1,NY,1,NZ,1,NT)
    COVAL(WALL3,H1,1.0/PRNDTL(H1),TROOM)
    COVAL(WALL3,W1,1.0,0.0)
    COVAL(WALL3,U1,1.0,0.0)
    COVAL(WALL3,V1,1.0,0.0)
    PATCH(WALL4,EWALL,NX,NX,1,NY,1,NZ,1,NT)
    COVAL(WALL4,H1,1.0/PRNDTL(H1),TROOM)
    COVAL(WALL4,W1,1.0,0.0)
    COVAL(WALL4,U1,1.0,0.0)
    COVAL(WALL4,V1,1.0,0.0)
    **open restriction represented by setting velocity=0**
    PATCH(PAN1,HIGH,1,NX,DY1+1,A,DZ1+DZ2+DZ3,DZ1+DZ2+DZ3,1,NT)
    COVAL(PAN1,W1,FIXVAL,0.0)
    COVAL(PAN1,U1,FIXVAL,0.0)
    COVAL(PAN1,V1,FIXVAL,0.0)
    PATCH(PAN2,HIGH,1,NX,9,NY-DY13,DZ1+DZ2+DZ3,DZ1+DZ2+DZ3,1,NT)
    COVAL(PAN2,W1,FIXVAL,0.0)
    COVAL(PAN2,U1,FIXVAL,0.0)
    COVAL(PAN2,V1,FIXVAL,0.0)
    PATCH(PAN3,HIGH,1,NX,DY1+1,A,NZ-DZ7,NZ-DZ7,1,NT)
    COVAL(PAN3,W1,FIXVAL,0.0)
    COVAL(PAN3,U1,FIXVAL,0.0)
    COVAL(PAN3,V1,FIXVAL,0.0)
    PATCH(PAN4,HIGH,1,NX,9,NY-DY13,NZ-DZ7,NZ-DZ7,1,NT)
    COVAL(PAN4,W1,FIXVAL,0.0)

```

```

COVAL(PAN4,U1,FIXVAL,0.0)
COVAL(PAN4,V1,FIXVAL,0.0)
**buoyancy boundary--Boussinesq approximation **
**source term = RSG10*(RSG1+RSG2*H1) or g*beta(Tin-T) **
**(note coordinate reversal) **
RSG10=9.81
PATCH(BUOY,PHASEM,1,NX,1,NY,1,NZ,1,NT)
COVAL(BUOY,W1,FIXFLU,GRND3)
RSG2=-BETA
RSG1=BETA * TIN
GROUP 14. Downstream pressure for PARAB=.TRUE.
GROUP 15. termination of sweeps
LSWEEP=10
RESREF(P1)=1.E-6
RESREF(W1)=1.E-6
RESREF(U1)=1.E-6
RESREF(V1)=1.E-6
RESREF(H1)=1.E-6
GROUP 16. Termination of iterations
GROUP 17. under-relaxation
RELAX(W1,FALSDT,1.0)
RELAX(U1,FALSDT,1.0)
RELAX(V1,FALSDT,1.0)
RELAX(H1,FALSDT,1.0)
RELAX(P1,FALSDT,1.0)
GROUP 18. Limits on variables or increments to them
GROUP 19. Data communicated by satellite to GROUND
GROUP 20. preliminary print-out
ECHO=F
GROUP 21. field and monitor control
OUTPUT(P1,Y,N,N,N,Y,Y)
OUTPUT(W1,Y,N,N,N,Y,Y)
OUTPUT(U1,Y,N,N,N,Y,Y)
OUTPUT(V1,Y,N,N,N,Y,Y)
OUTPUT(H1,Y,N,N,N,Y,Y)
GROUP 22. spot value print-out
NPRMON=20
IYMON=50
IZMON=25
IXMON=3
IPLTL=LSWEEP
GROUP 23. field print-out and plot control
NPLT=1
CRSIZ=.4
NYPRIN=5
NZPRIN=NZ/10
NXPRIN=3
NTPRIN=NT/2
ITABL=3
STOP

```



## Appendix D: DISCUSSIONS ON THE USE OF PHOENICS

Using "PHOENICS" for this investigation involved extensive computational time due to the physical size of the problem. A  $100 \times 100$  grid was used in the solution of a problem with the momentum and energy equations being coupled through the buoyancy body force term. In addition, the time-dependent formulation was chosen to address time-dependent behavior adding to the computational time. The computational time was, however, reduced by increasing the F array and NFDIM in the ground from a default of 50000 to 300000. Increasing these dimensions effectively decreased the I/O to the disk and increased amount of operation within the core memory. No additional modifications to the ground subroutine made for this investigation.

The buoyancy body force was incorporated using a ground subroutine which utilizes the Boussinesq approximation. The only difficulty in the specification of this ground subroutine was the direction of the body force term. With "PHOENICS", the inlet along the z-axis is taken to be the "low" with the outlet being the "high". A coordinate reversal was required to maintain consistency with the direction of the body force term and the direction of flow in the z-direction specific to "PHOENICS".

## REFERENCES

- Aung, W. "Mixed Convection in Internal Flow." In *Handbook of Single-Phase Convective Heat Transfer*, pp. 15.1-15.51. Kakac, S., Shah, R.K., and Aung, W. New York: John Wiley and Sons, 1987.
- Bajorek, S.M., and Lloyd, J.R. "Experimental Investigation of Natural Convection in Partitioned Enclosures." *ASME Journal of Heat Transfer* 104 (1982): 527-532.
- Beethe, R.L., Wolff, R.K., Griffis, L.C., Hobbs, C.H., McClellan, R.O. (1979) Evaluation of a Recently Designed Multi-Tiered Exposure Chamber. Technical Report EY-76-C-04-11013, Department of Energy Contract.
- Bernstein, D.M., and Drew, R.T. (1981) The Major Parameters Affecting Temperature Inside Inhalation Chambers. Technical Report BNL 51318 UC-48, Brookhaven National Laboratory.

Carpenter, R.L., and Beethe, R.L. (1981) Cones, Cone Angles, Plenums, and Manifolds. Technical Report BNL 51318 UC-48, Brookhaven National Laboratory.

Chiu, K., and Rosenberger, F. "Mixed Convection Between Horizontal Plates-I. Entrance Effects." *Int. J. Heat Mass Transfer* 30 (1987): 1645-1654.

Chiu, K., Ouazzani, J., and Rosenberger, F. "Mixed Convection Between Horizontal Plates-II. Fully Developed Flow." *Int. J. Heat Mass Transfer* 30 (1987): 1655-1662.

Choudhury, D., and Patankar, S.V. "Combined Forced and Free Laminar Convection in the Entrance Region of an Inclined Isothermal Tube." *ASME Journal of Heat Transfer* 110 (1988): 901-909.

Doebelin, E.O. 1983. *Measurement Systems Application and Design*. New York: McGraw-Hill.

Gebhart, B. 1971. *Heat Transfer*. New York: McGraw-Hill Book Company.

Hemenway, D.R., Carpenter, R.L. and Moss, O.R. "Inhalation Toxicology Chamber Performance: A Quantitative Model." *Am. Ind. Hyg. Assoc. J.* 43 (1982): 120-127.

Hemenway, D.R. and MacAskill, S. "Design, Development and Test Results of a Horizontal Flow Inhalation Toxicology Facility." *Am. Ind. Hyg. Assoc. J.* 43 (1982): 874-879.

Hinds, W.C. 1982. *Aerosol Technology, Properties, Behavior, and Measurement of Airborne Particles*. New York: John Wiley and Sons.

Lee, Jae-Heon, and Goldstein, R.J. "An Experimental Study on Natural Convection Heat Transfer in an Inclined Square Enclosure Containing Internal Energy Sources." *ASME Journal of Heat Transfer* 110 (1988): 345-349.

Markatos, N.C., and Malin, M.R. "Mathematical Modelling of Buoyancy-Induced Smoke Flow in Enclosures." *Int. J. Heat Mass Transfer* 25 (1982): 63-75.

Mauderly, J.L. "Respiration of F344 Rats in Nose-only Inhalation Exposure Tubes." *Journal of Applied Toxicology* 6 (1986): 25-30.

Moss, R.O. (1981) A Chamber Producing Uniform Concentrations of Particulates for Exposure of Animals on Tiers Separated By Catch Pans. Technical Report BNL 51318 UC-48, Brookhaven National Laboratory.

Moss, O.R., Decker, J.R., and Cannon, W.C. "Aerosol Mixing in an Animal Exposure Chamber Having Three Levels of Caging With Excreta Pans." *Am. Ind. Hyg. Assoc. J.* 43 (1982): 244-249.

Nansteel, M.W., and Greif, R. "Natural Convection in Undivided and Partially Divided Rectangular Enclosures." *ASME Journal of Heat Transfer* 103 (1981): 623-629.

November, M., and Nansteel, M.W. "Natural Convection in Rectangular Enclosures Heated From Below and Cooled Along One Side." *Int. J. Heat Mass Transfer* 30 (1987): 2433-2440.

Osborne, D.G., and Incropera, F.P. "Experimental Study of Mixed Convection Heat Transfer for Transitional and Turbulent Flow Between Horizontal, Parallel Plates." *Int. J. Heat Mass Transfer* 28 (1985): 1337-1344.

Ostrach, S. "Natural Convection Heat Transfer in Cavities and Cells." *Heat Transfer* 1 (1982): 365-379.

Ostrach, S., and Austin, W.J. "Natural Convection in Enclosures." *ASME Journal of Heat Transfer* 110 (1988): 1175-1190.

Patankar, S.V. 1980. *Numerical Heat Transfer and Fluid Flow*. New York: Hemisphere Publishing Corp.

Powe, R.E., and Warrington, Jr., R.O. "Natural Convection Heat Transfer Between Bodies and Their Spherical Enclosures." *ASME Journal of Heat Transfer* 105 (1983): 440-446.

Ramachandran, N., Chen, T.S., and Armaly, B.F. "Mixed Convection in Stagnation Flows Adjacent to Vertical Surfaces." *ASME Journal of Heat Transfer* 110 (1988): 373-377.

Ramadhani, S., Zenouzi, M., and Astill, K.N. "Combined Natural and Forced Convective Heat Transfer in Spherical Annuli." *ASME Journal of Heat Transfer* 106 (1984): 811-816.

Riley, A. "A New Approach to the Construction of Small Animal Inhalation Chambers: Design and Evaluation." *Am. Ind. Hyg. Assoc. J.* 47 (1986): 147-151.

Spalding, D.B. (1980) *Mathematical Modeling of Fluid-Mechanics, Heat Transfer and Chemical Reaction Processes*. Technical Report HTS/80/1, Imperial College, London.

Sparrow, E.M., Stryker, P.C., and Ansari, M.A. "Natural Convection in Enclosures With Off-Center Innerbodies." *Int. J. Heat Mass Transfer* 27 (1984): 49-56.

Tanaka, H., Maruyama, S., and Hatano, S. "Combined Forced and Natural Convection Heat Transfer for Upward Flow in a Uniformly Heated, Vertical Pipe." *Int. J. Heat Mass Transfer* 30 (1987): 165-174.

unknown author. (unknown date) *Measurements in Low Velocity Gases*. Technical Report TB 14, TSI.



Warrington, Jr, R.O., and Powe, R.E. "The Transfer of Heat by Natural Convection Between Bodies and Their Enclosures." *Int. J. Heat Mass Transfer* 28 (1985): 319-330.

Yang, K.T. "Natural Convection in Enclosures." In *Handbook of Single-Phase Convective Heat Transfer*, pp. 13.1-13.51. Kakac, S., Shah, R.K., and Aung, W. New York: John Wiley and Sons, 1987.

Yang, K.T. "Transitions and Bifurcations in Laminar Buoyant Flows in Confined Enclosures." *ASME Journal of Heat Transfer* 110 (1988): 1191-1204.

Yao, L.S. "Free and Forced Convection in the Entry Region of a Heated Vertical Channel." *Int. J. Heat Mass Transfer* 26 (1983): 65-72.

Yeh, H.C., Newton, G.J., Barr, E.B., Carpenter, R.L., and Hobbs, C.H.

"Studies of the Temporal and Spatial Distribution of Aerosols in Multi-Tiered Inhalation Exposure Chambers." *Am. Ind. Hyg. Assoc. J.* 47 (1986): 540-545.

Yeh, H.C., Snipes, M.B., Eidson, A.F., Hobbs, C.H.. (1988) Comparative Evaluation of Nose-only vs. Whole-body Inhalation Exposures for Rats. Technical Report annual report LMF-121, Lovelace Inhalation Toxicology Research Institute.

Yerkes, K.L., Faghri, A. "An Experimental and Numerical Simulation of Mixed Convection in Large Baffled Rectangular Chambers." to appear in *Proc. ASME Winter Annual Meeting* (1989): .

Yerkes, K.L., Faghri, A. "Mixed Convection Analysis in Large Baffled Rectangular Chambers." to be presented at *ASME Summer Annual Meeting* (1990): .

Zhong, Z.Y., Yang, K.T., and Lloyd, J.R. "Variable Property Effects in Laminar Natural Convection in a Square Enclosure." *ASME Journal of Heat Transfer* 107 (1985): 133-138.